Topographic Reconstructions of the Trans-Gondwanan Mountain Belt

Thesis submitted in accordance with the requirements of the University of Adelaide for an Honours Degree in Geology/Geophysics

Flynn Cameron

November 2021

THE UNIVERSITY of ADELAIDE

ABSTRACT

Reconstructing the evolution of the shape of Earth's surface in deep time has not been previously attempted. How topography changes through time is essential in understanding the controls on ancient Earth systems (e.g. climate, biology and atmosphere/hydrosphere chemistry). The Neoproterozoic to Cambrian East African Orogen amalgamated through an important time for Earth's climate. Here, I attempt the first reconstruction of the changing topography of the trans-Gondwanan mountain belt, as a first step in revealing the significance of the mountain belt on climate throughout this period. The topographic reconstruction was attempted by incorporating inverted metamorphic pressure–time (P–t) data into a compositional isostatic equilibrium equation. This was done to determine an approximate elevation of the mountain belt relative to the modern-day elevation. By georeferencing the P–t data to current geological provinces, and incorporating them into a full plate model, a paleo-geographic topographic reconstruction was developed through the final amalgamation sequence of Central Gondwana. Across the orogen there is a variability in the depths that the rocks were buried and ultimately the elevations the mountain belts reached above sea level. The Arabian Nubian Shield (accretionary orogenesis from ~750–600 Ma) produced elevations of up to ~3 km peak elevation, similar to average heights of the current day European Alps. In the Mozambique and India/Madagascar belts much higher elevations of up to ~8 km, are predicted from ~650 –530 Ma., elevations similar to the current day Himalayas.

In addition to developing a methodology to apply topography in deep time, a proof-of-concept study was undertaken to efficiently obtain relevant pressure-time data for future campaign-style topography reconstruction studies. This was done using garnets from a well characterised transect across Southern India, which dated using the novel laser Lu–Hf inductively coupled plasma reaction cell mass spectrometry (LA-ICP-MS/MS) technique. Quartz inclusions within these were then analysed using RAMAN spectroscopy to determine their trapping pressures. These produced results of up to ~12–15 kbar at ages ~600 to 540 Ma (peak conditions) which agree with conventional pressure-time studies and demonstrate the potential of this workflow.

KEYWORDS

Topography, Reconstruction, Isostasy, Gondwana, Climate, East African Orogen, Garnet, Neoproterozoic.

TABLE OF CONTENTS

LIST OF FIGURES AND TABLES

INTRODUCTION

Topography, the features of Earth's surface, are controlled by the movement of tectonic plates, which is linked to Earth's climate. The elevation and global location of mountains has a major control on the intensity of erosion, feeding into the carbon cycle. Therefore, an understanding of the evolution of topography, is critical when attempting to model the Earth system in deep time (Chamberlin 1899; Raymo, Ruddiman, and Froelich 1988; Hilton and West 2020). The process of silicate weathering within mountains draws down CO_2 from the atmosphere, which is a long term control on climate (Hilton and West 2020; Mills, Donnadieu, and Goddéris 2021). These processes are also a factor in the amount of nutrients supplied to the ocean, which controls biological activity and photosynthetic oxygen production (Goddéris et al. 2017).

The Neoproterozoic was a tumultuous time in Earth's history, with breakup and formation of supercontinents, extreme climatic variation and the proliferation of life (Halverson et al. 2009; Lenton et al. 2014; Hoffman et al. 2017). The oceanic Sr^{87}/Sr^{86} isotope record also displays a strong increase over the mid/late Neoproterozoic, which is used as a proxy for the weathering of old rocks and thus erosion rates of mountain belts (Shields 2007; Halverson et al. 2009).

The late Neoproterozoic – early Cambrian East African Orogen (EAO) is considered the largest orogen of the last billion years prior to the Cenozoic, which formed during the final amalgamation of Gondwana (Collins and Pisarevsky 2005; Fritz et al. 2013). The EAO is over 7000 km in strike length and is thought to be analogous to the Himalayas (Fritz et al. 2013).

Merdith et al. (2021), attempted the first full plate tectonic reconstruction for the last billion years, providing indicative locations of tectonic plates through time. However, to develop a climate model for the Neoproterozoic, the other variable that must be considered is topography (Mills et al. 2019; Mills, Donnadieu, and Goddéris 2021). Moreover, it is not straightforward to reconstruct the topography of half a billion years ago, so the EAO is used as a case study to test the feasibility of estimating topography in deep time. The EAO preserves rocks at the surface that experienced a wide range of pressures and temperatures in the Neoproterozoic, which reflect varying degrees of orogenic burial at different times during the amalgamation of Gondwana (Fritz et al. 2013).

This study investigates inversions of pressure-time metamorphic data from past studies across the EAO, and paleo-georeferences them in tectonic reconstructions of the orogen (Merdith et al. 2021). Applying crustal parameters for ancient and modern crusts (taken from various data sources; *see Table 5*) allows for the determination of a series of paleo-crustal sections, to balance against their associated modern crustal sections. This enables definition of the ancient overburden enforced upon the ancient crustal columns and allows the correction for isostasy (Airy 1855; Pratt and Stokes 1859; Pratt and Challis 1855). This facilitates the development of a compositional (and in-future thermal) isostatic inversion for both crustal columns, which predict elevation-time points across the EAO (Hasterok and Chapman 2007). These are limited in space-time based on their locale and the limited abundance of preserved rock. In order to counter these complications, a reconnaissance, proof-of-concept study, was undertaken trialling a workflow obtaining campaign-style P–t estimates for the orogen. This was collected from the age of garnets and pressures derived from trapped quartz inclusions.

GEOLOGICAL SETTING/BACKGROUND

Topographic Reconstructions and Isostatic Equilibrium

Topographic reconstructions in deep time have rarely been attempted due to the uncertainty of inverting data to past elevations. Here, I attempt to reconstruct a crustal column using published pressure-time data and rock compositions to input into an isostatic equilibrium equation to find corresponding elevation in deep time.

Using the reconstructed density of the crustal columns from a place at a known time and balancing the input parameters to the crustal column developed for the modern crust, it is possible to develop a gradient in height for the mountains through time. This is called the compositional isostasy. This process is based off the initial concepts proposed by Airy(1855) & Pratt(1855; 1859) and are prepared using pressure and density estimates. Defining this gives a basic uncorrected elevation relative to the elevation of the crust above sea level today. In future studies, this height can be further modified to correct for the thermal isostatic elevation variations that are based on temperature at depth, thermal conductivity, heat production and heat flow input parameters (Hasterok and Chapman, 2007).

East African Orogen

The East African Orogen (EAO) was a dynamic belt that formed via a series of tectonic collisional events involved in the amalgamation of Gondwana from ~850–530 Ma, after the break-up of the supercontinent Rodinia (Fritz et al. 2013; Collins and Pisarevsky 2005; Stern 1994). Each of these events was significant in the building of a large mountain belt stretching across the Gondwanan supercontinent (Jacobs, Bauer, and Fanning 2003; Squire et al. 2006). Today these events are preserved in remnants of the old mountains in metasedimentary and meta-igneous rocks stretching from northern Egypt on the Sinai Peninsula to Mozambique in the south and Southern India/Sri Lanka to the east (Johnson et al. 2011b; Fritz et al. 2013; Collins et al. 2021). The EAO consists of two distinct areas. To the north the Arabian Nubian Shield (ANS), which consists of a pre-amalgamated series of Neoproterozoic arc accretions from ~850–700 Ma, these make up modern Egypt, Sudan, Eritrea, Ethiopia and some parts of Saudi Arabia (Johnson et al. 2011a; Fritz et al. 2013). The ANS stretches eastward to the Afif and Azania microcontinent terranes that geographically make up modern Saudi Arabia, Yemen and Somalia (Johnson et al. 2011a). Four distinct accretion events are recorded in the ANS, highlighted by (Fritz et al. 2013; Robinson et al. 2014), these range from ~850–600 Ma. This study, however, is focussed on the latter events in the amalgamation from ca. 680–600 Ma. To the south, the lower grade metamorphic ANS pinches out, moving into the Mozambique Belt (MB), which preserves much higher grades (Fritz et al. 2013). Published geochronology from these areas show protolith ages only closely predating the metamorphism (Johnson et al. 2011b; Tenczer et al. 2013). These correspond to the arc amalgamation ages before becoming overprinted by the Afif-Abas collision event in the latter ANS formation (Johnson et al. 2011a). To the south of this, the Mozambique Belt consists of various reworked pre-Neoproterozoic crustal fragments involved in events ranging from ~650–530 Ma, the MB stretches from Kenya to Tanzania in a series of granulite facies metamorphosed terranes including Mozambique and Madagascar (Fritz et al. 2013). Remnants of the MB are associated with the Southern Granulite Terrain (SGT) of southern India and the granulite metamorphic terrains across Madagascar (Plavsa et al. 2015). Ages corresponding to these events throughout these regions are recorded in information from granulites, however some past geochronology reveals protolith ages to be variable from Archean to Mesoproterozoic in age (Collins, Clark, and Plavsa 2014; Plavsa et al. 2015; Clark et al. 2020).

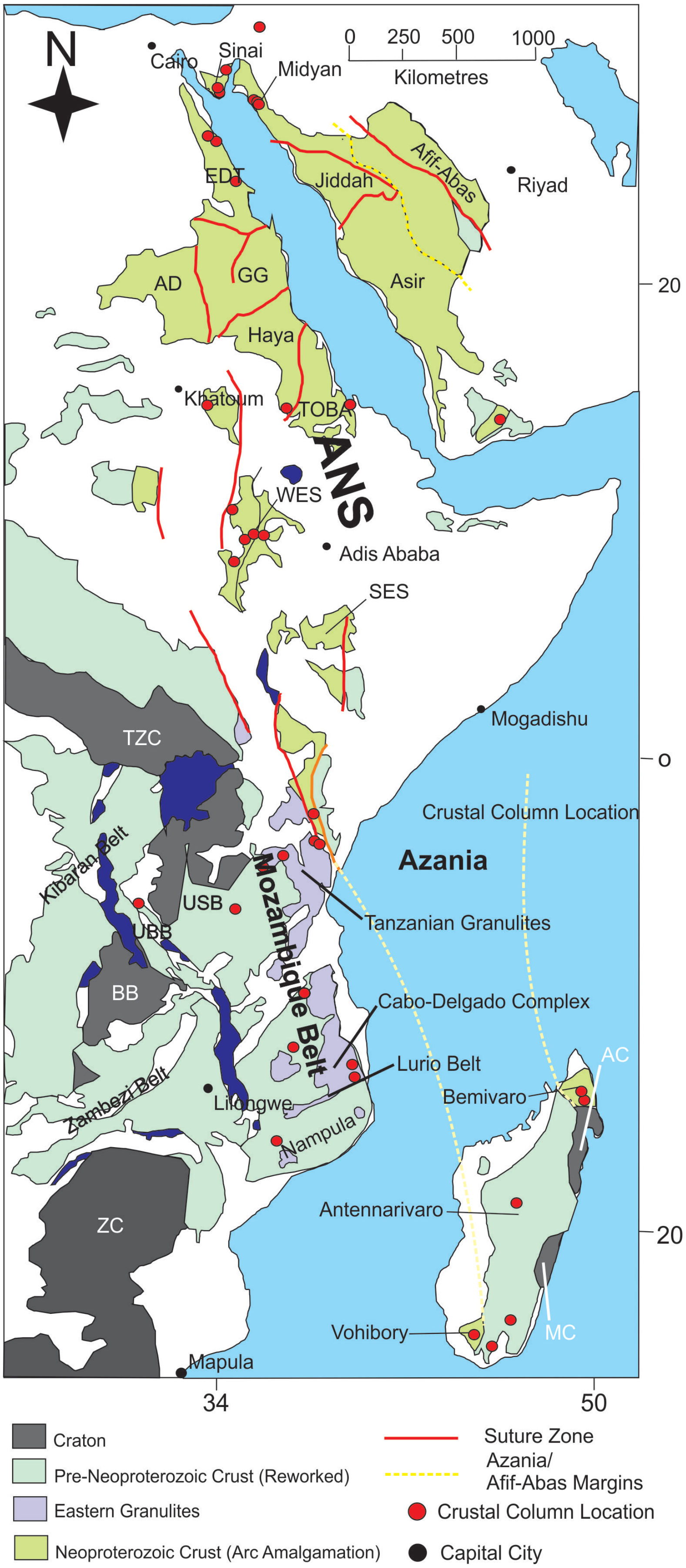

Figure 1: Crustal Provinces involved in the East African Orogen modified from (Fritz et al. 2013). Detailing the sample locations collected from literature to be used to define the crustal provinces, the individual provinces involved across the ANS/MB/Madagascar.(*see Table 5; Appendix C*)

Arabian Nubian Shield

In the Arabian Nubian Shield the oldest continental amalgamation event is associated with the final amalgamation between the Afif Abas microcontinent and the previously accreted ANS volcanic arc (Johnson et al. 2011a). Evidence of this accretion system was recorded in the Baladiyah metamorphic complex of eastern Saudi Arabia. This complex preserved mid-amphibolite facies metamorphism at approx. 750 Ma. This was not a widely observed metamorphic event in the ANS (Abu-Alam et al. 2014). A continental collisional event from ~680–650 Ma produced an extensive regional greenschist/amphibolite facies metamorphism event. With evidence from the Sinai peninsula of Egypt in the Feiran-Solaf Metamorphic complex (Abu El-Enen and Whitehouse 2013) and the Baladiyah metamorphic complex recording a second metamorphic event. These initial events preserved relatively low temperature and low pressure conditions (Abu-Alam et al. 2014). The collision of the amalgamated arc-microcontinent-proto-ANS with the North African Plate, is a latter event recorded in the ANS. This is associated with ages from ~650–610 Ma, evidenced in: the Sinai Peninsula and Eastern Desert metamorphic terranes of Egypt; the Wadi Abu Barqa and associated metamorphic complexes of Jordan; the Elat metamorphic complexes of Southern Israel; and the Baladiyah complex of eastern Saudi Arabia (STERN and MANTON 1987; Eliwa et al. 2008; Jarrar et al. 2013; Abu-Alam et al. 2014; Elisha, Katzir, and Kylander-Clark 2017; Abu Sharib et al. 2018). All these complexes recorded metamorphism from greenschist to mid-amphibolite facies. However, in the southern ANS, the Kenyan metamorphic complexes recorded events of the same ages to upper-amphibolite facies with a relatively large increase in pressure in comparison to the events of the northern ANS (Hauzenberger, Robl, and StÜWe 2005; Hauzenberger et al. 2007b). A final event in the ANS was recorded from ~620–600 Ma, this is associated with the fully amalgamated ANS collision with the Afif, Sahara Metacraton and Congo Plates. This event was preserved in the metamorphic complexes of Eritrea, the Southern and Western Ethiopian shields, the Eastern Desert Terrain and Sinai peninsula of Egypt and the western boundary of the Sahara Metacraton in Northern Sudan (Johnson et al. 2004; Andersson, Ghebreab, and Teklay 2006; Abu El-Enen and Whitehouse 2013; Karmakar and Schenk 2015). These recorded regionally variable P–T information to higher conditions relative to the previous event, preserving mid-amphibolite to upper-amphibolite facies metamorphism.

Mozambique Belt, Madagascar and India

The Mozambique belt is a continuation from the southern ANS and mostly consists of Archean and Paleoproterozoic crustal fragments reworked in the amalgamation of Gondwana (Collins, Clark, and Plavsa 2014; Plavsa et al. 2015; Clark et al. 2020). These are associated with the continental collisions of the microcontinent Azania (Madagascar, Sri Lanka and Southern India) with the Congo Craton (Collins et al. 2007). These record their earliest metamorphic activity to variably high pressure and moderate temperature granulites from ~640 Ma. These include the Kenyan and Tanzanian eastern granulite system from current mountains of the Pare, Usambara, Ukaguru and Uluguru Mountains (Meert, van der Voo, and Ayub 1995; APPEL, MÖLLER*, and SCHENK 1998; Möller, Mezger, and Schenk 2000; Sommer et al. 2003; Huntly Cutten, Simon P. Johnson, and Bert De Waele 2006; Boniface and Schenk 2007; Hauzenberger et al. 2007a; Bingen et al. 2009; Boniface and Schenk 2012; Tenczer et al. 2013; Sommer, Kröner, and Lowry 2017). These correlate to the latter metamorphic events recorded across the ANS supposedly being associated with a large boundary frontal continental collision with the Azanian microcontinent (Collins and Pisarevsky 2005; Fritz et al. 2013). Granulite metamorphism, continuing until approx. 580 Ma has been interpreted to be a prolonged collision/suture (Fritz et al. 2013). The Southern Mozambique Belt continuing in to the Mozambique Cabo-Delgado Nappe System, preserves the final amalgamation of Gondwana, recording upper granulite facies metamorphism with very high pressure and variable mid/high temperatures across ~580–540 Ma (Viola et al. 2008; Bingen et al. 2009; Boyd et al. 2010; Ueda et al. 2012; Engvik, Tveten, and Solli 2019). The ~550 Ma collision between the Indian Dharwar, Antongil and Masora Cratons and the amalgamated Azania/Congo continent recorded upper amphibolite to granulite facies metamorphism. It preserved mid/high pressure, mid temperature metamorphic conditions in the Bemarivo Belt, Antananarivaro Block, Anoysen Block, Vohibory Group and the Androyen Group of Madagascar (Kröner, Braun, and Jaeckel 1996; Markl, Bäuerle, and Grujic 2000; JÖNS et al. 2006; JÖNS and SCHENK 2008; Jöns and Schenk 2011; Boger et al. 2014).

These are also recorded in the southern terranes of India/Sri Lanka in the Southern Granulite Terrane, the Trivandrum-Nagercoil Block, the Vijayan, Highland and Wanni complexes (Kröner and Williams 1993; Raase and Schenk 1994; Prakash 2008; Prakash, Prakash, and Sachan 2010; Li et al. 2019). These granulites retain variable mid/high pressures and ultra-high temperatures. These provinces are inferred to have been a part of the Azanian microcontinent and at the forefront of the final collision involved in the formation of Gondwana (Collins and Pisarevsky 2005).

Analytical Case Study on Garnets from Southern India

As a part of the development of a topographic reconstruction across the East African Orogen, a methodology has been developed as part of a case study to obtain pressure–time data for campaign-style analysis of garnets, these will be applied to the topographic reconstruction. Garnets are a common porphyroblast in metamorphic rocks and preserve geochronological and thermobarometric information, which makes them a perfect target for obtaining data for a topographic reconstruction. Garnet data was collected from a transect across the Southern Granulite Terrane of India.

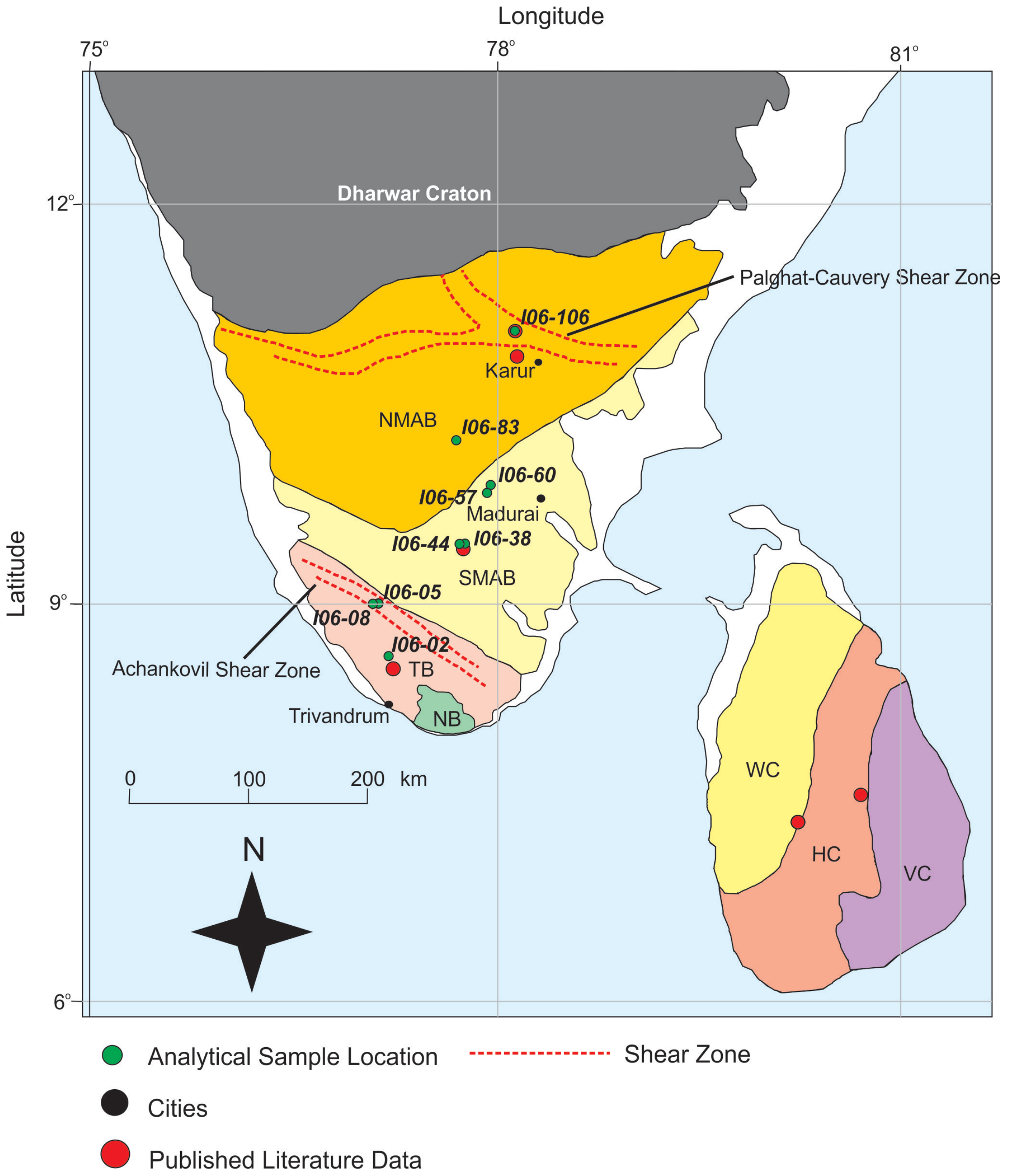

Figure 2: A diagram modified from (Ratheesh-Kumar et al. 2020) detailing the crustal provinces in Southern India showing the whole SGT in NB (Nagercoil Block), TB (Trivandrum Block), SMAB (Southern Madurai Block), NMAB (Northern Madurai Block) as well as their associated complexes from Sri Lankain the WC (Wanni Complex), HC (Highland Complex) and VC (Vijayan Complex). It includes the P-T-t data collected from published literature to define a crustal column and the samples collected as part of the 'case study' on garnets "analytical sample location".

Organisation and Layout

This thesis outlines differing methodologies, their results and their hierarchical position in the overall topographic reconstruction. For the 'Analytical Methods' section, a transect within Southern India was used as a proof-of-concept for obtaining pressure-time data. The methodology outlines the methods applied to these rocks. Along with this, data from different geological provinces was collated from past literature across the areas of the EAO, including from the areas involved with the 'case study' as part of the analytical methodology.

It is important to understand that the purpose of this study is to attempt a new approach to characterise mountain topography in deep time, rather than precisely quantify past topography. Many assumptions with related uncertainties are necessary to carry out this study, which are clearly outlined in the text. The data collected is a separate case study to collect useable pressure-time data across Southern India, which in future can be used to dramatically increase the data needed for paleo-topographic reconstructions.

METHODS

Paleo-elevations are estimated using an isostatic equation at specifically defined areas of the EAO where pressure-time data is extracted from the literature. Using an isostatic equilibrium equation to balance crustal columns from deep time to the present, is undertaken by manually defining physical properties to each of the columns.

Defining the parameters used in the balanced equation was accomplished using past literature from specific locations (geological provinces) across the orogen. These values were highly variable in their quality and reliability. To improve this, a pressure-time workflow was developed coupling Lu–Hf age of garnets (Simpson et al. 2021) with RAMAN spectroscopy of trapped quartz inclusions from samples in Southern India, when undertaking future paleo-topography studies the workflow will keep the dataset obtained consistent. The data collected from both sources will be used to define specific physical properties for the crustal columns used in the isostasy equation (*See Fig. 3)*.

The variability in credibility and reliability of data from past literature created difficulty in data collection. The sparsity and integrity of data across important areas in the EAO such as Somalia, Sudan and Kenya was inherently poor. Therefore, results from studies that are credible and reliable across the EAO, will be interpolated to represent a larger regional setting rather than a localised one, as well as neglecting some areas with poor or few data. To counter the difficulties in obtaining certain data, the limitations, assumptions and uncertainties in the collected literature data as well as the analytically obtained data are discussed.

Analytical Approach

To test the proof-of-concept workflow, data from a credible and reliable source is necessary for the application to the isostasy method. This was done using an analytical methodology to obtain pressure-time (P-t) data from single garnets in relevant samples, by coupling laser Lu–Hf ICP-MS/MS with RAMAN spectroscopy analysis of trapping pressures from quartz inclusions in the garnets. A further proposed analysis to estimate independent temperatures through titanium content in quartz inclusions was not undertaken due to time constraints. Instead, for this study we have constrained trapping pressures using estimated temperatures from published literature. This allows for the efficient determination of peak pressure and age of the metamorphic rocks that are garnet-bearing. In this study, samples were collected from a transect over Southern India. The transect consists of nine samples and covers garnet bearing rocks across the SGT ranging from the Trivandrum-Nagercoil Block in the south to the Northern Madurai Block in the north (*see Fig. 2)*.

Undertaking this study in Southern India is ideal as there is a large amount of good quality thermobarometric studies in the region, which we will use to compare with our study. The results from the samples will also be used in tandem with the developed isostasy method.

GEOCHRONOLOGY

LA-ICP-MS/MS garnet Lu-Hf Geochronology

Lu–Hf age data were collected from in-situ garnet porphryoblasts ranging from 500 µm to 10000 µm from seven samples mounted in epoxy resin pucks. All samples were imaged using the M4 TORNADO Micro-XRF in order to reveal any garnet zonation patterns and obtain the relative yttrium content abundance as a proxy for lutetium, using the methodology developed by Simpson et al. (2021). Based on this, seven samples were chosen for analysis via LA-ICP-MS/MS, using a RESOlution/LR ArF 193 Nanometer Excimer Laser and Agilent 8900x ICP-MS/MS. The ablation of garnets was performed in an argon atmosphere with a frequency of 10Hz. A spot size of 120 µm was used for all the samples with an acquisition time of 110 seconds total. The measured isotopes were ^{176}Lu, ^{176}Hf and ^{177}Hf. The collected age data were processed and calculated in the program LADR (Norris 2018). The samples were corrected to the secondary standard Hogsbo-1 (1039.5 ± 46.8 Ma; MSWD: 0.038) *(see Appendix B).*

LA-ICP-MS monazite and rutile inclusion in garnet U-Pb Geochronology

Where one sample yielded an uncertainty in Lu–Hf age, U–Pb age data were also collected from monazite and rutile inclusions in a garnet porphryoblast from sample I06-106a to further constrain the age of metamorphism (I06-106 a maf). To avoid any complicated zonation within the garnet, the sample was imaged using a Hitachi SEM. These were analysed using LA-ICP-MS, using the RESOlution/LR ArF 193 Nanometer Excimer Laser and Aligent 8900x ICP-MS. The monazite and rutile grains were analysed in an argon atmosphere with a frequency of 5Hz. A spot size of 43 µm for rutile and 13 µm for monazite was used with acquisition time of 120 seconds. The measured isotopes for monazite were ^{206}Pb, ^{207}Pb, ^{208}Pb, ^{238}U, ^{235}U and ^{232}Th. These age data were processed in the program LADR. The monazite data were corrected to the secondary standard MAdel and the rutile data were corrected to the secondary standard R19(499.94 ± 10 Ma; MSWD: (*see Appendix B*).

RAMAN Spectroscopy Barometry

An analysis using the RAMAN spectroscopy method was performed on samples I06-08, I06-83, I06-106a maf, I06-02 and I06-38. Analyses were conducted using a Witec UHTS 300 spectrometer (holographic gratings of 1,800 grooves/mm) attached to a Witec alpha300 confocal Raman microscope at the Scanning Probe Microscopy Facility, Curtin University. Raman spectra were excited using a 532nm solid state Nd:YAG laser. The spectrometer was initially calibrated to the 520.5 cm^{-1} of metallic silicon and subsequently calibrated to the 464.8 cm^{-1} peak of synthetic quartz. The spectra of unstrained (free) crystals of synthetic quartz was measured throughout the analysis session to subsequently calibrate the analytical sessions. The collected spectra were background corrected for the continuum luminescence background. Peak positions, full widths at half maximum (FWHMs), and integrated intensities were determined from fits with pseudo-Voigt functions in Witech Project FOUR. For each of the selected Raman bands the shift in wave number ($\Delta\omega$) was calculated as the difference between the peaks of the analysed inclusion (ω_i) and the peaks of a reference spectra of a free and unstrained quartz crystal (ω_0). Sets of $\Delta\omega$ for each inclusion (modes ω_{128}, ω_{206}, and ω_{464}) have been used to determine strain using the software stRAinMAN (Angel et al. 2019) by employing the Grüneisen tensors for quartz (Murri et al. 2018). Calculation of entrapment pressure and isomekes was conducted in EntraPT, an online MATLAB toolbox (Mazzucchelli, Angel, and Alvaro 2021).

ISOSTASY APPLICATION

Depth Calculation

The results of the analytical methodology detailed above, combined with published literature pressure-time data are needed to effectively test the isostatic equilibrium equation (*see Table 5*). In addition, density data is needed for the crust beneath the surface and the now-eroded crust that lay above the present erosion level (*assumed: see Table 1*). These estimates were collected either directly from the rock geochemistry described by a global geochemical database (Rybach 1988, Jennings et al. 2019, Gard et al 2019, Hasterok et al. 2017, Hasterok et al 2019, Hasterok et al 2021), or from associated density data based on the location in the associated geological province. With these parameters $Eq. 1$, depth can be determined at any time t_n.

$$P = pgh$$

Where P is the pressure of the current rock at surface in pascals, p is the estimated compositional density of the current rock at the surface in kg/m^3 (calculated using a weighted mass equation from the global geochemical database; *see Appendix C*) , g is the gravitational acceleration constant $9.80665\ ms^{-2}$ and h is the depth of the crust in kilometres. Inverting this equation, we are able to determine the depth at which the rocks were buried, assuming that there were no non-gravitational forces contributing to the resultant stresses. This ensures that we can determine a modelled depth at which the now exposed rocks were buried into the crust, an important parameter in defining the thickness of the crustal column at time t_n.

Compositional Isostatic Equilibrium

From applying an estimation of depth in deep time, extrapolating a compositional isostatic height estimation is based on applying thicknesses and density data to a modern-day crust as well as the eroded crust, which is assumed to have a widely accepted overall compositional density of 2850 kg/m^3.

Determining the layout of the modern crustal structure is again based on literature. Seismic survey results across the region were used to define the modern crustal layout. These parameters are used to estimate the compositional density in each layer resulting in a weighted average density of the crust to the Moho (Qureshi 1971; Mooney et al. 1985; Mahatsente, Jentzsch, and Jahr 1999; Rao and Bitragunta 2006; Hansen et al. 2007; Leinweber et al. 2013; Dreiling et al. 2020)(*see Table 4; Appendix C*). The Moho is assumed to be the approximate compensation depth, meaning that this is the theoretical end of the crust in this adaption for each crust (see *Fig. 3*).

When equalising these columns to one another and simplifying the equation we are able to determine the relative displacement in elevation in the crust from time t_n to the modern crust at time t_0, using $Eq. 2$, which was a modified equation from the initial isostatic equilibrium equations proposed by Airy (1855) and Pratt (1855; 1859).

$$-\Delta\varepsilon = \frac{(h_{c1}p_{c1} - h_{c2}p_{c2})}{p_m} - h_{c1} + h_{c2}$$

Where $\Delta\varepsilon$ is the relative change in height (km) from t_n to t_0, h_{c1} & h_{c2} are the crustal thicknesses of the crustal columns at t_n and t_0, p_{c1} & p_{c2} are the associated densities to the individual crustal columns and p_m is the approximate density of the mantle (3330 kg/m^3).

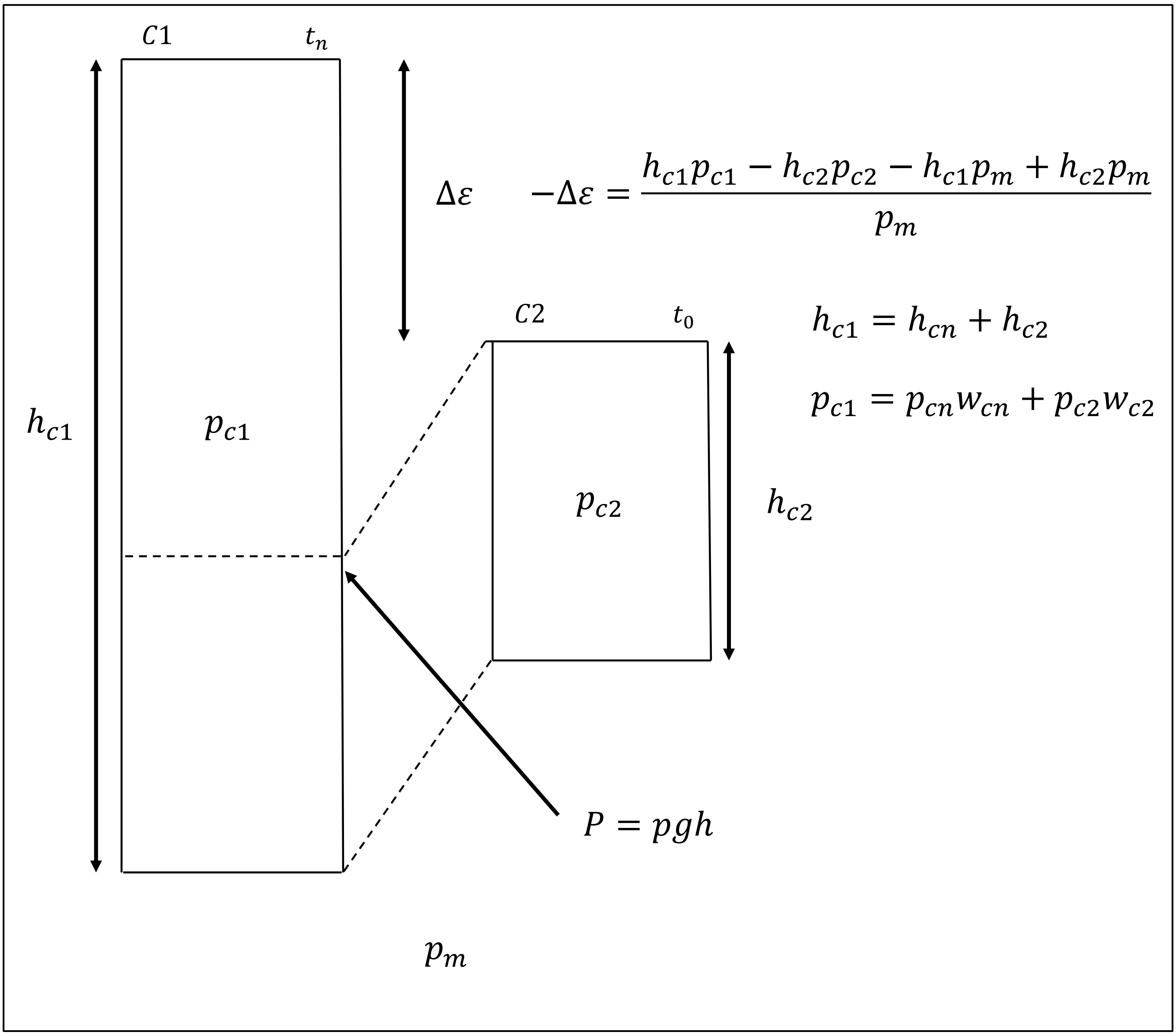

Figure 3: Schematic diagram detailing the compositional isostatic equilibrium equation for both crustal columns C1 the ancient crust and C2 the modern crust and the parameters used to define them. P, is pressure, p is the density, g is the gravity acceleration constant,

Description	Assumed/*Calculated Value	Parameter
Eroded crust homogenous density	2850 kg/m^3	p_{cn}
Mantle constant density	3330 kg/m^3	p_m
Gravitational Acceleration constant	9.80665 m/s^2	g
Weighted density and crustal thickness profile	*From Crustal Structure Seismic Profiles	p_{c2}; W_{c2}
Modern Moho depth	*from Crustal structure Seismic Profiles	h_{c2}
Ancient depth in crust	*from the depth equation (surface density and associated pressures)	h_{cn}

Table 1: Assumed/Calculated values for parameters used to calculate the compositional isostasy from *Eq.1* and *Eq.2*.

This equation (*Eq. 2*) produces a basic elevation referred to as the compositional isostatic elevation, which is the relative difference of the eroded mountains to the current crust after accounting for isostasy. This has had no corrections based on its thermal isostasy, base height from seismic surveys or errors calculated and defined for the height itself. The thermal isostasy is calculated using past temperature data obtained at depth (P-T-t) as well as the thermal conductivity and heat production in each of the layers of the modern crust and the ancient crust. The methodology that should be considered in future studies is detailed below.

THERMAL ADJUSTMENT

The compositional isostasy based on the density for each of the profiles first defined by Pratt then Airy in 1855, produces unadjusted models to their thermal state, which allows for the buoyancy of the crustal columns to be corrected slightly based on their approximate geotherm. Hence, this should produce elevations slightly higher than those calculated from the compositional densities.

Thermal Isostasy

Calculation of two geotherms are needed for each of the crustal columns, a regional geotherm as well as a reference geotherm. An approximate elevation gradient can be calculated the difference between two lithospheric thermal states, from which an approximated depth change can be calculated, thus allowing for a correction to the compositional isostasy.

The thermal isostasy geotherm difference equation is listed below.

$$\Delta\varepsilon_T = a_v \int_{z_0}^{z_{max}} \left[T(z) - T_{ref}(z)\right] dz$$

Where a_v is the thermal expansion coefficient, z_{max} is the maximum depth of integration or the point at which both geotherms have reached the mantle adiabat, $T_{ref}(z)$ is the geotherm calculated for a reference column (C1), $T(z)$ is the regional geotherm calculated for (C2) and $\Delta\varepsilon_T$ is the elevation change for the thermal isostasy.

To calculate the geotherms a simple temperature relationship with depth was developed in a 1-D layered model (Chapman 1986).

$$T_n = T_0 - q_0 \Delta z \sum_{i=1}^{n} \frac{1}{k_i} + \sum_{i=1}^{n} \frac{A_i}{2k_i} \Delta z^2 - \frac{\Delta z^2}{2} \sum_{i=1}^{n-1} \frac{(\sum_{j=1}^{i} A_i)}{k_{i+1}}$$

This calculates the temperature at depth to the n^{th} layer in conjoined steps, where T_0 is the temperature at the surface, A_i is the heat production of the layer, k_i is the layer thermal conductivity, Δz is the depth extent, g_0 is the heat flow at the surface calculated from current databases and n is the consecutive layer number. These parameters were calculated from their rock compositions from the global geochemical database. Adjusting the initial compositional isostasy to its thermal correction is just an addition onto the initial elevation calculation.

For the ancient crust, however, the only information available are the metamorphic P-T conditions. Therefore, an inversion of the typical equation *(See below)* is needed to obtain the surface heat flow for the hypothetical eroded crust which was developed assuming a felsic-dominated continental crust.

$$q_0 = \frac{T_n - T_0 + \Delta z^2 \sum_{i=1}^{n-1} \frac{\sum_{j=1}^{i} A_j}{k_{i+1}} + \frac{\Delta z^2}{2} \sum_{i=1}^{n} \frac{A_i}{k_i}}{\Delta z \sum_{i=1}^{n} \frac{1}{k_i}}$$

Error Calculation

Errors were calculated using the individual parameter errors for pressure, temperature, model thermal conductivity, model heat production, model densities and crustal thickness. This uncertainty will be used to show where some calculations can be relatively unaffected or where the collection of data must be improved in future studies. It also highlights where some assumptions can have large effects.

OBSERVATIONS AND RESULTS

Analytical Method Results

GEOCHRONOLOGY

Lutetium-Hafnium Geochronology

All data can be found in the supplementary material. Analyses were targeted using the yttrium dispersion in the garnets outlined by TXRF scans. The results for samples I06-08, I06-83, I06-02 and I06-38 yielded appropriate ages (*Fig. 5; Fig. 6)*. The other samples analysed, however, returned highly imprecise ages. This was interpreted as being due to the garnets experiencing extreme temperatures allowing the diffusive loss of hafnium. The ages also may have been affected by inclusions within the garnet. All samples produced ages between ~650–550 Ma, apart from I06-02 which produced an irregular age of Paleoproterozoic age (*see Table 2*).

Sample Number	Location	Lithology	Latitude	Longitude	Age (Ma)	MSWD	n
I06-08	Trivandrum Block	Granulite Facies Metapelitic Schist	9.012306	76.877417	591.0 ± 28.3	1.1	65
I06-02	Trivandrum Block	Granulite Facies Metapelitic Gneiss	8.602944	76.952694	1923.9 ± 159.7	1.2	77
I06-83	Northern Madurai Block	Granulite Facies Metabasic Schist	10.281639	77.534361	601.5 ± 52.6	1.1	49
I06-38	Southern Madurai Block	Granulite Facies Metapelitic Gneiss	9.442222	77.5935	578.0 ± 131.3	1.1	60

Table 2: Table summary showing the samples analysed from the Lu–Hf garnet dating technique

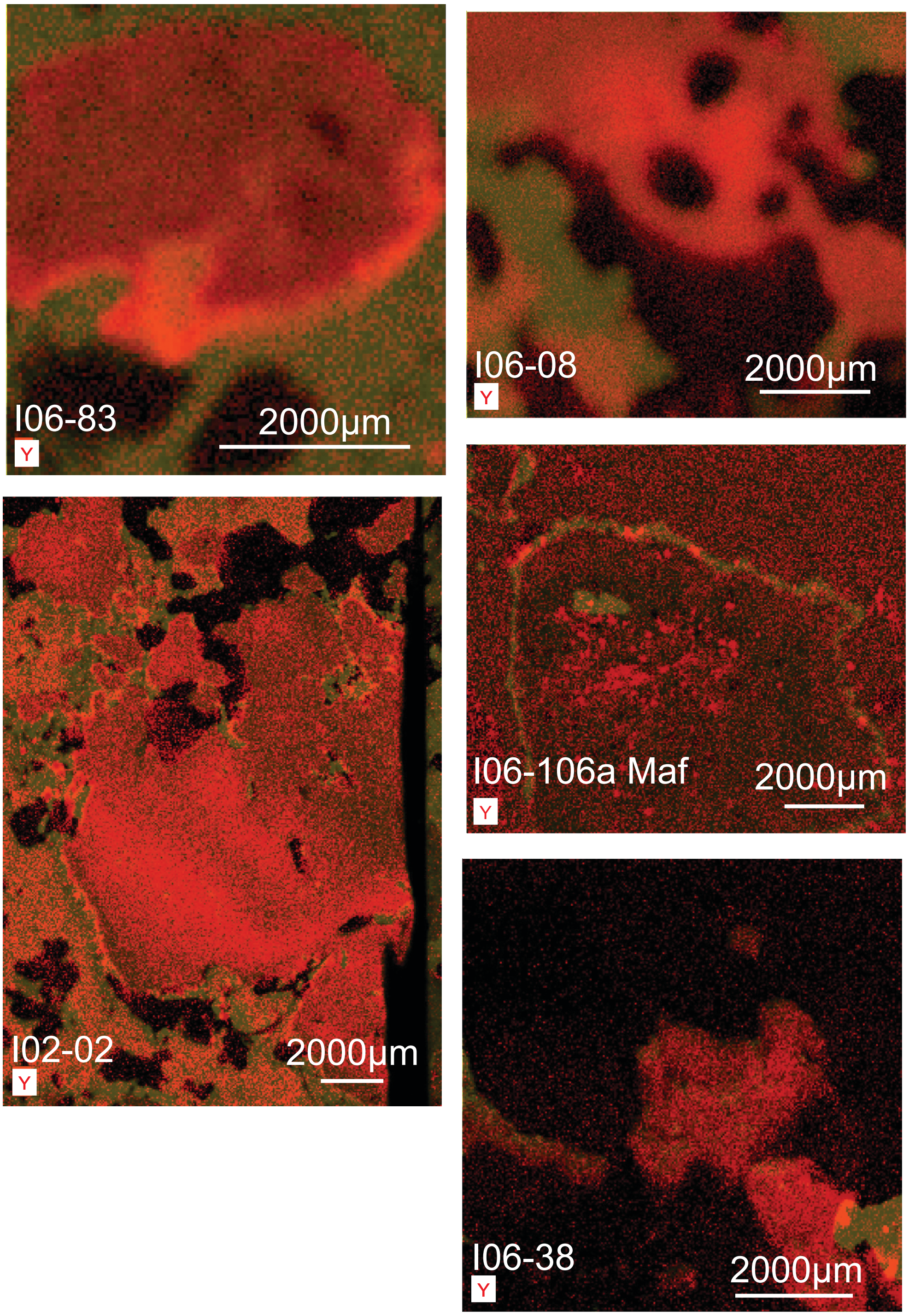

Figure 4: Tornado XRF imaging of dispersed yttrium content across zones in garnet samples used for the Lu–Hf dating method. Red is the concentration of the yttrium across the garnet. I06-83 shows a significant concentration around the rim of the garnet, but lacks yttrium content in the core. I06-08 does not show any yttrium zonation, rather a homogenous concentration throughout. I02-02 shows an erratic zonation with what seems to be multiple zones around a low yttrium concentration core. I06-106a maf shows yttrium concentration on inclusions within the garnet, not the actual garnet mineral. I06-38 alike sample I06-08 shows a homogenous yttrium concentration throughout the garnet.

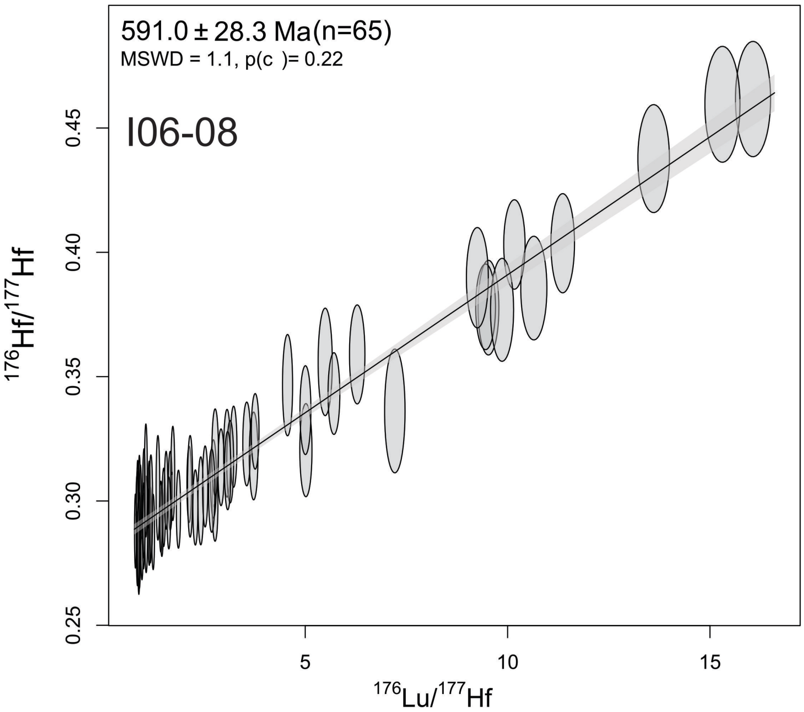

Figure 5: Above: Whole garnet (all zones) Lu/Hf isochron was calculated for sample I06-08, No omitted laser ablation spots, Below: Whole garnet (all zones) Lu/Hf isochron was calculated for sample I06-83, two omitted ablation spots based on uncertainty in errors.

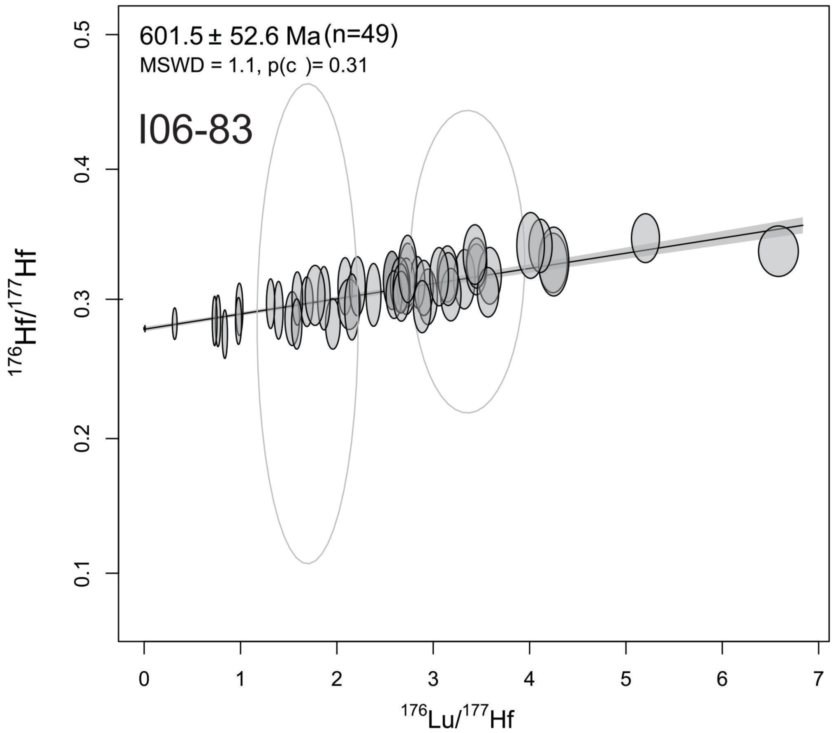

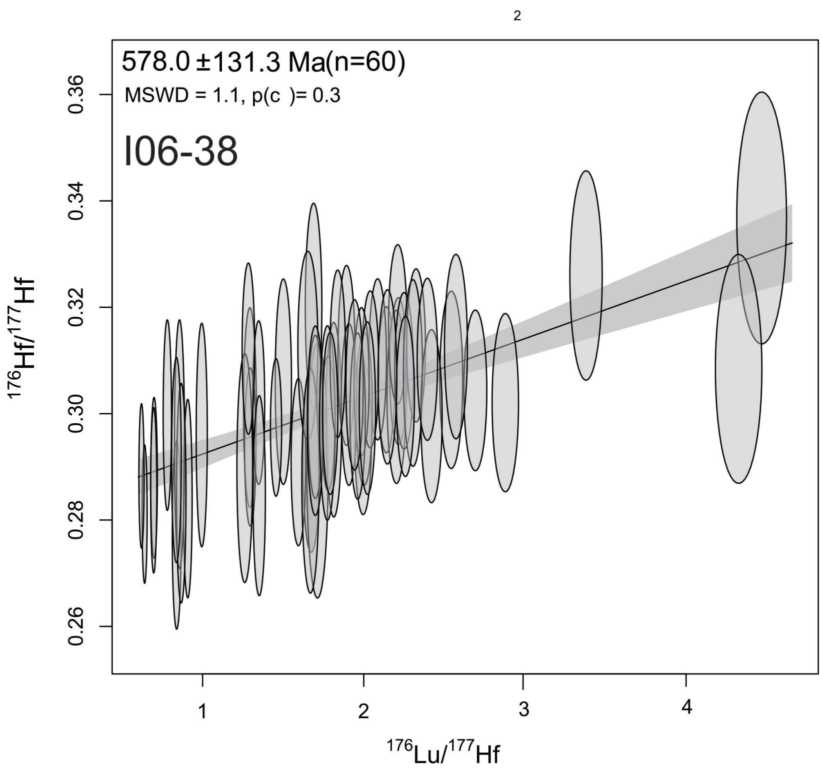

Figure 6: Above: whole garnet (all zones) Lu–Hf isochron was calculated from sample I06-38, no omitted ablation spot. Below: Whole garnet (all zones) Lu–Hf isochron was calculated from sample I06-02, ablation spots omitted, presented as part of a newly discovered age.

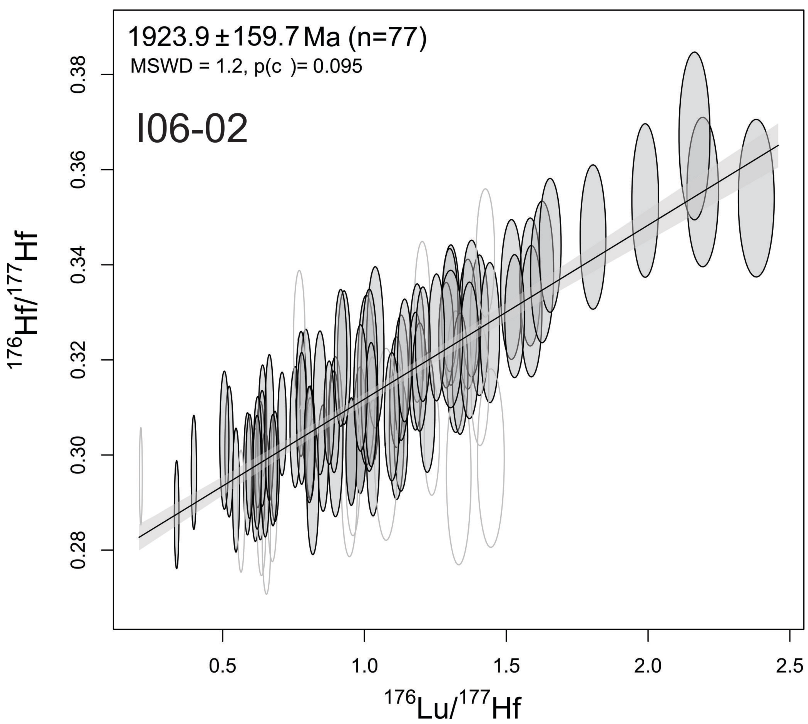

Uranium-Lead monazite and rutile inclusions in Garnet

Monazite and rutile inclusions within garnet were analysed (U–Pb) to confirm the Lu–Hf age, which yielded a large uncertainty from sample I06-106a maf. These were imaged on the SEM to ensure the recognition of complex zoning in the minerals (*Fig 7; Fig 8*). These data have been summarised in *Table 3* (*Fig.9; Fig. 10; Fig.11)*. Raw data found *in Appendix B*.

Sample Number	Location	Lithology	Latitude	Longitude	Mineral	Age (Ma)	MSWD	N
I06-106a maf	Palghat-Cauvery Shear Zone	Granulite Facies Metapelitic Gneiss	11.135694	78.047944	rutile	452.9 ± 2.77	1.75	12
					monazite	535.4 ± 1.4	1.33	39

Table 3: Table summary of sample I06-106a monazite and rutile ($^{206}Pb/^{238}U$) weighted mean ages.

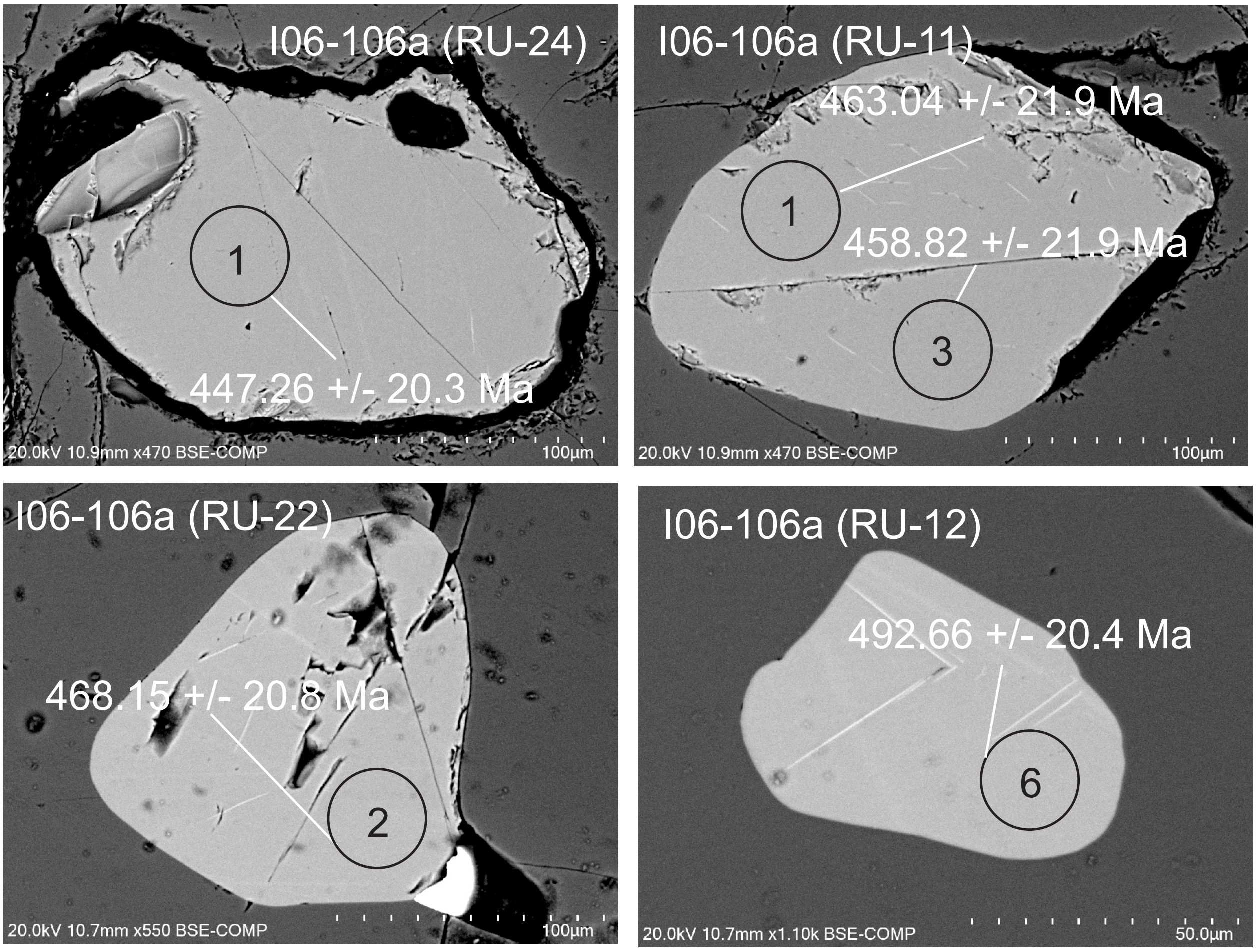

Figure 7: CL imaging of rutile inclusions in garnet sample I06-106a maf, indicating the most concordant rutile grains and their individual laser spots.

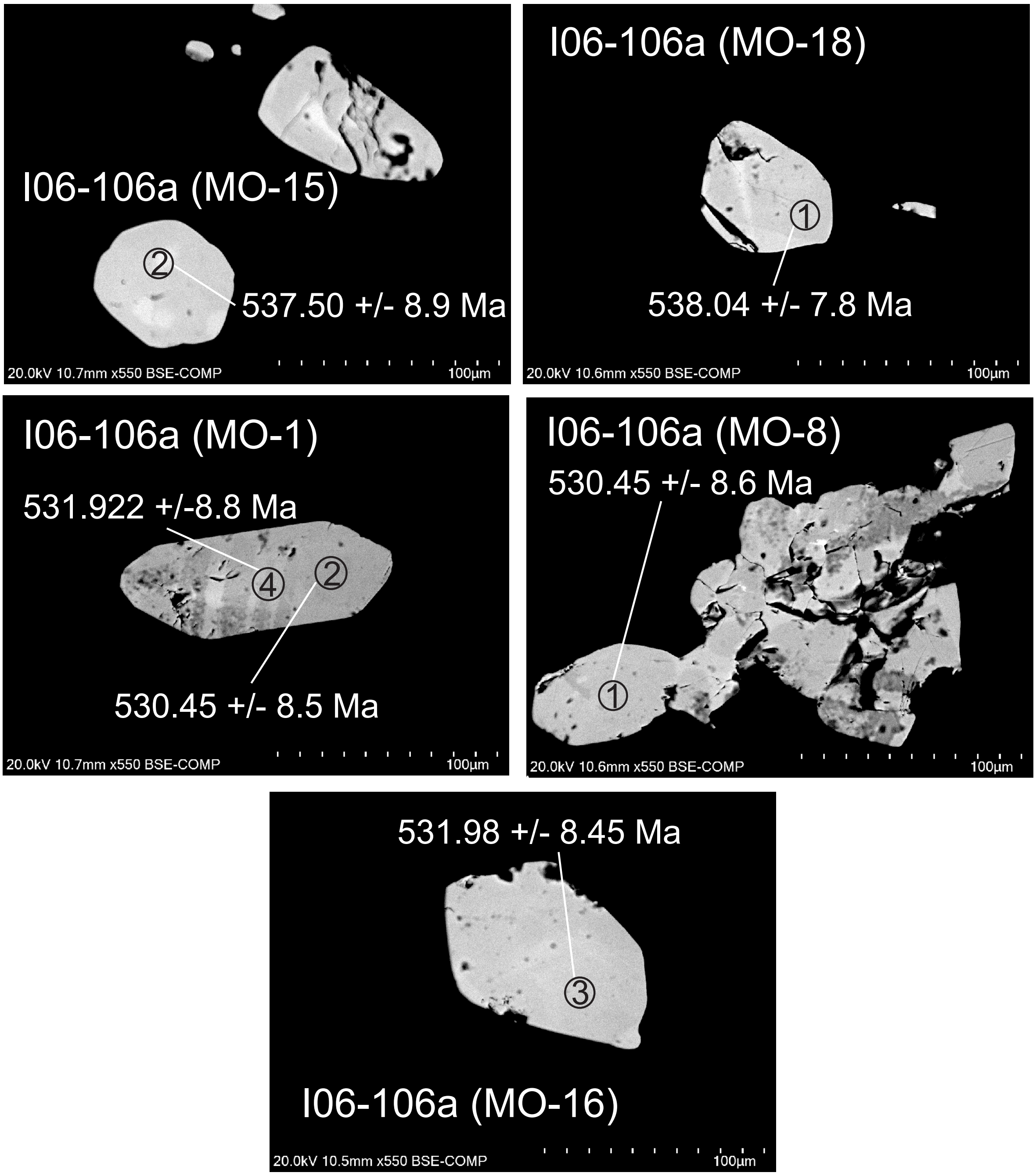

Figure 8: CL imaging of monazite inclusions in garnet sample I06-106a maf, indicating the most concordant monazite grains with their individual laser spots.

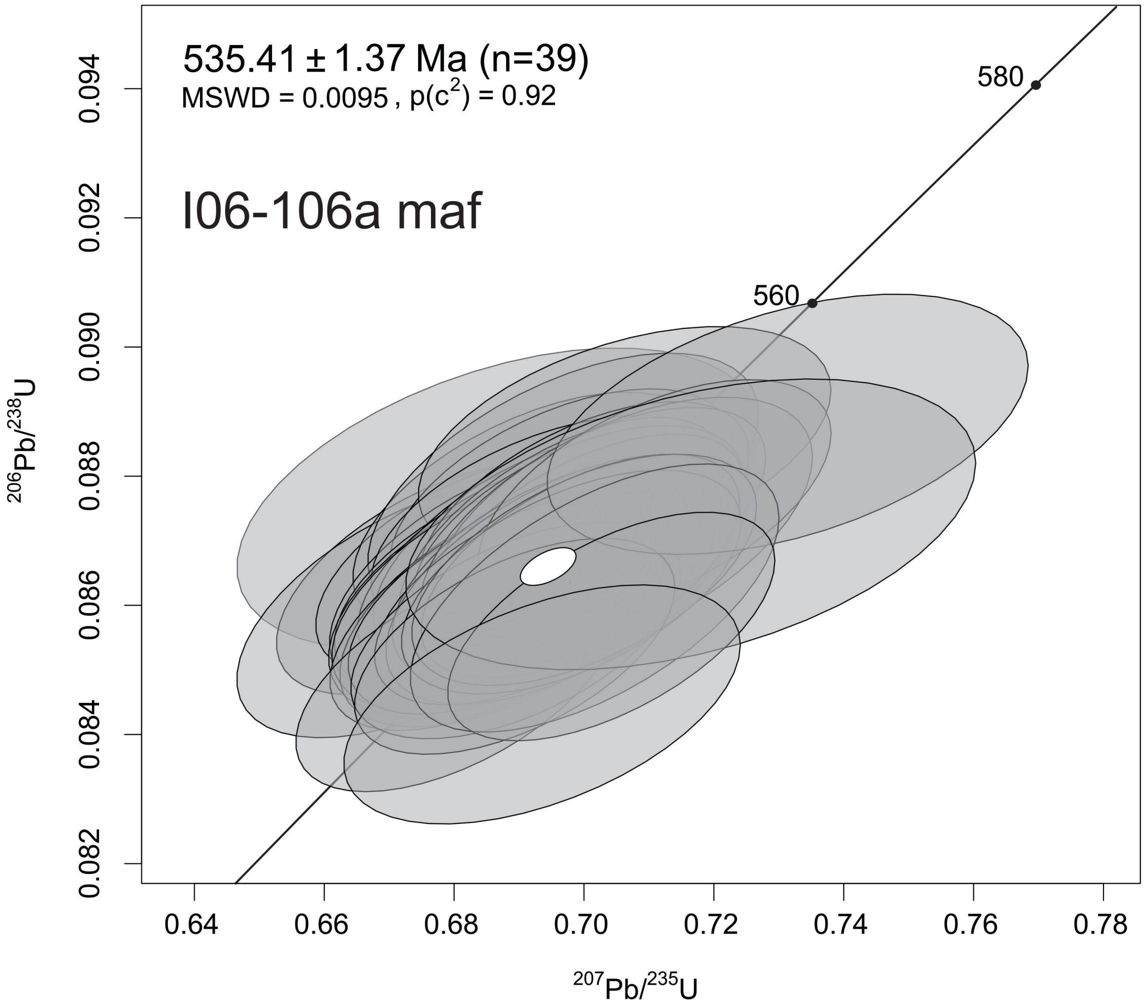

Figure 9: U/Pb concordia diagram calculated from monazite grains in sample IO6-106a Maf, all laser ablation spots used, no omitted data.

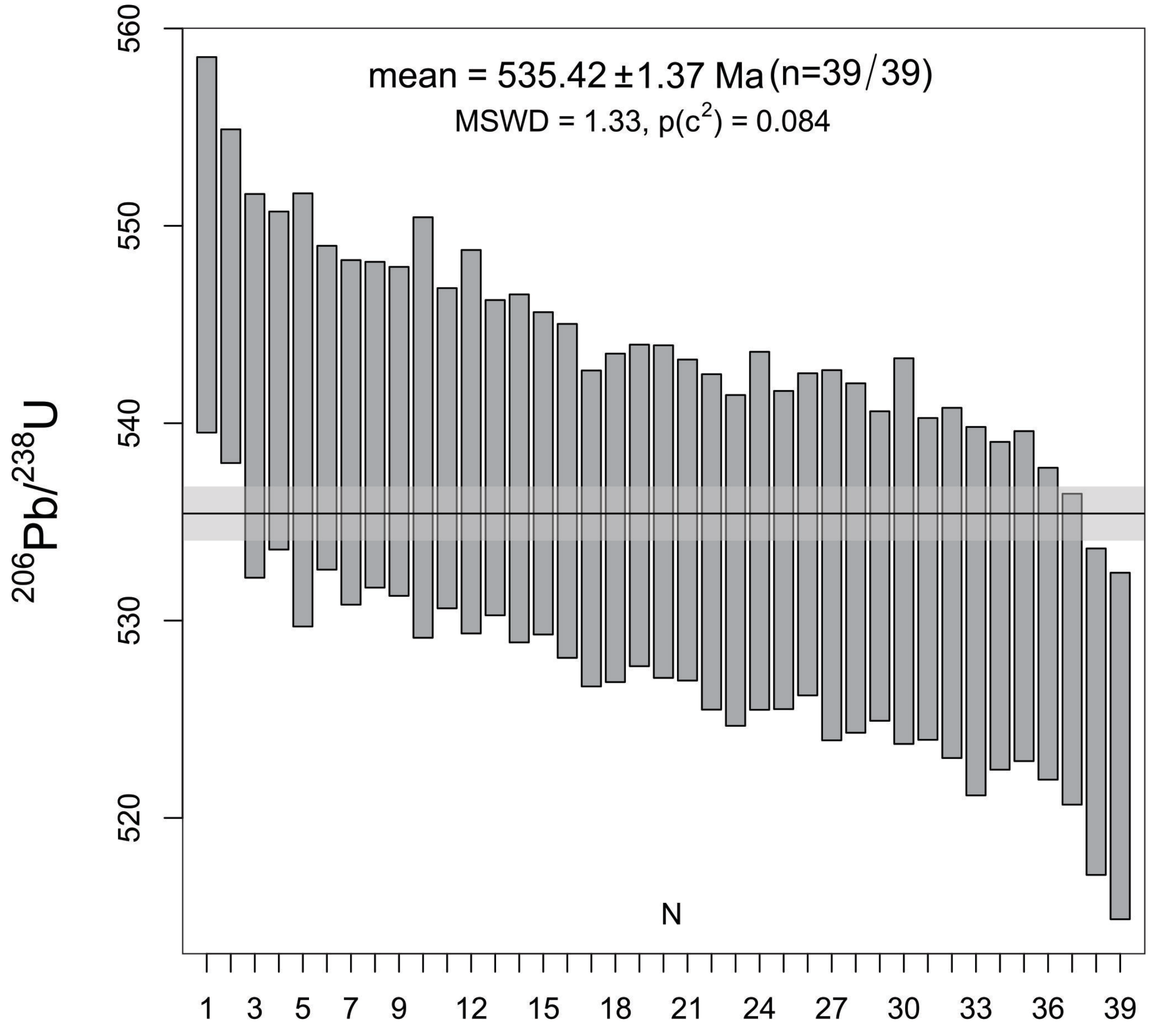

Figure 10: Calculated ($^{206}Pb/^{238}U$) weighted mean with no omitted data, error bars are 2σ in range.

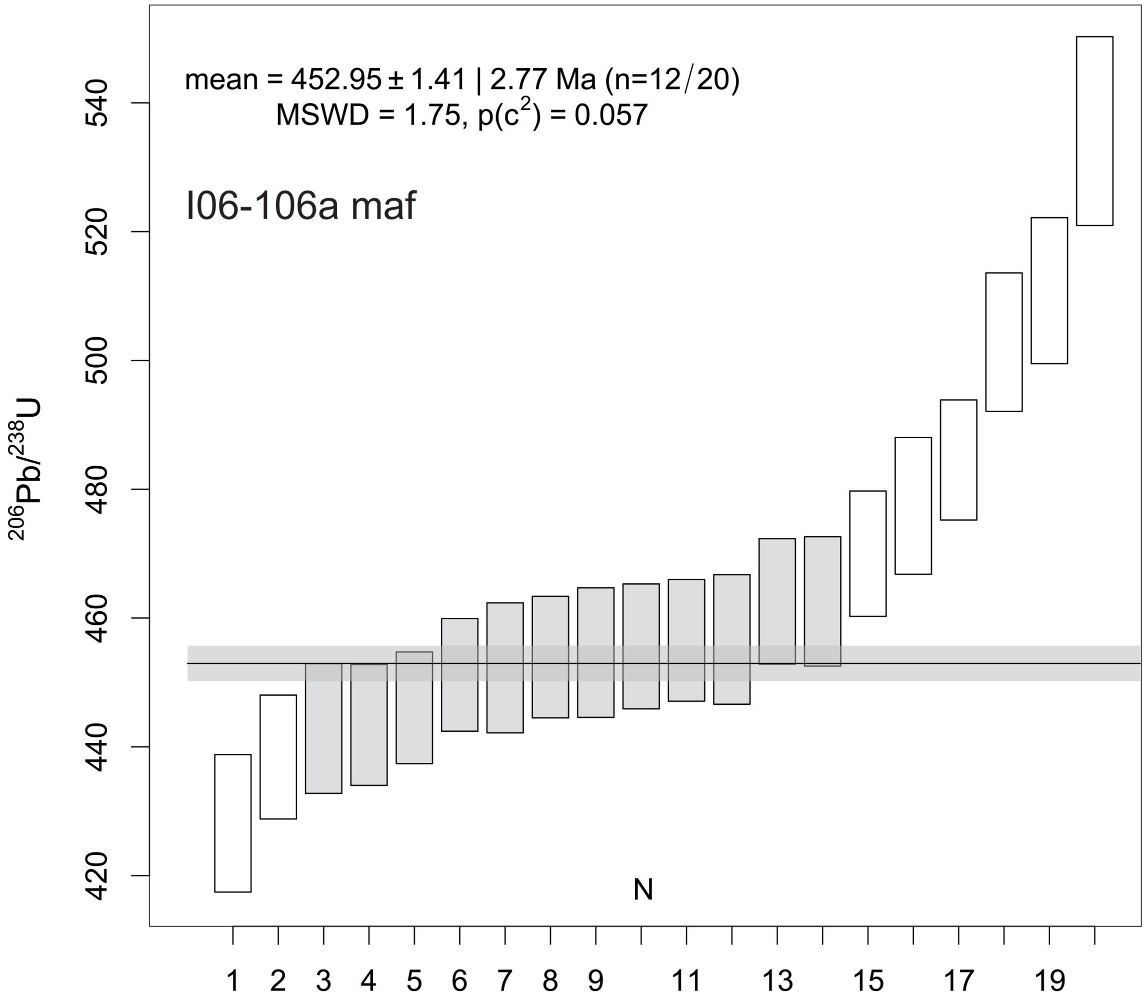

Figure 11: U/Pb Weighted mean calculated from rutile grains in garnet I06-106a (mafic), outlined from most $^{206}Pb/^{238}U$ to the least, the omitted results unshaded are results are quoted by the 2σ range (grey shaded area).

RAMAN Spectroscopy Barometry

Samples I06-08 and I06-83 both produced reasonable results for the RAMAN spectroscopy barometery at temperatures calculated from published data in the Trivandrum and Madurai Blocks respectively (Collins et al. 2007; Prakash, Prakash, and Sachan 2010; Taylor et al. 2014; Harley and Nandakumar 2016). The results are summarised in *Table 4*. The other samples (I06-02, I06-38 and I06-106a maf), however, were fractured to varying degrees, which may have resulted in lower enclosed strains.

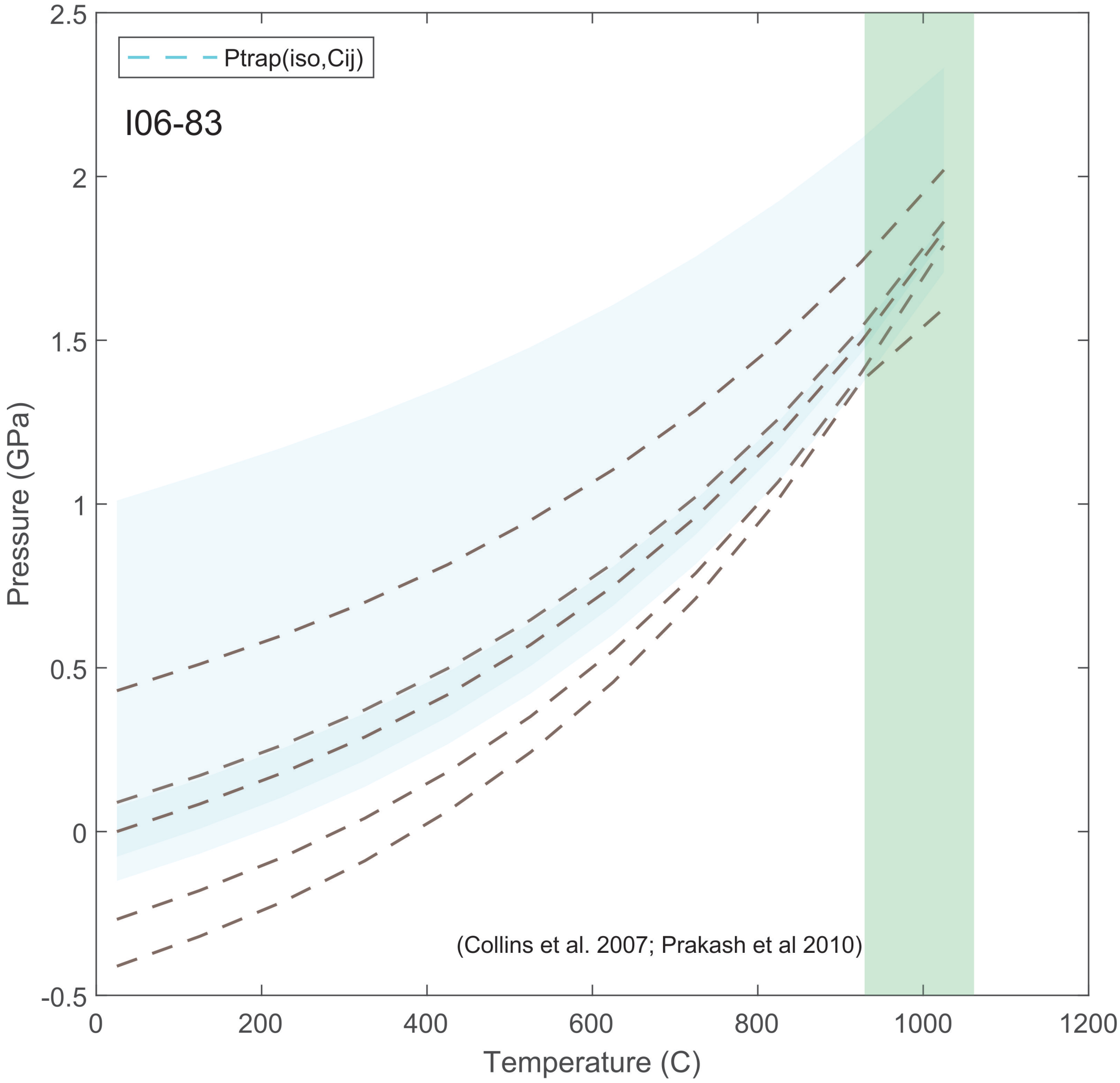

Figure 12: P-T isomekes for sample I06-83 calculated using RAMAN Spectroscopy of quartz inclusions, with the temperatures from the published literature (Collins et al. 2007; Prakash, Prakash, and Sachan 2010) as overlays for identifying possible pressures at peak P-T conditions.

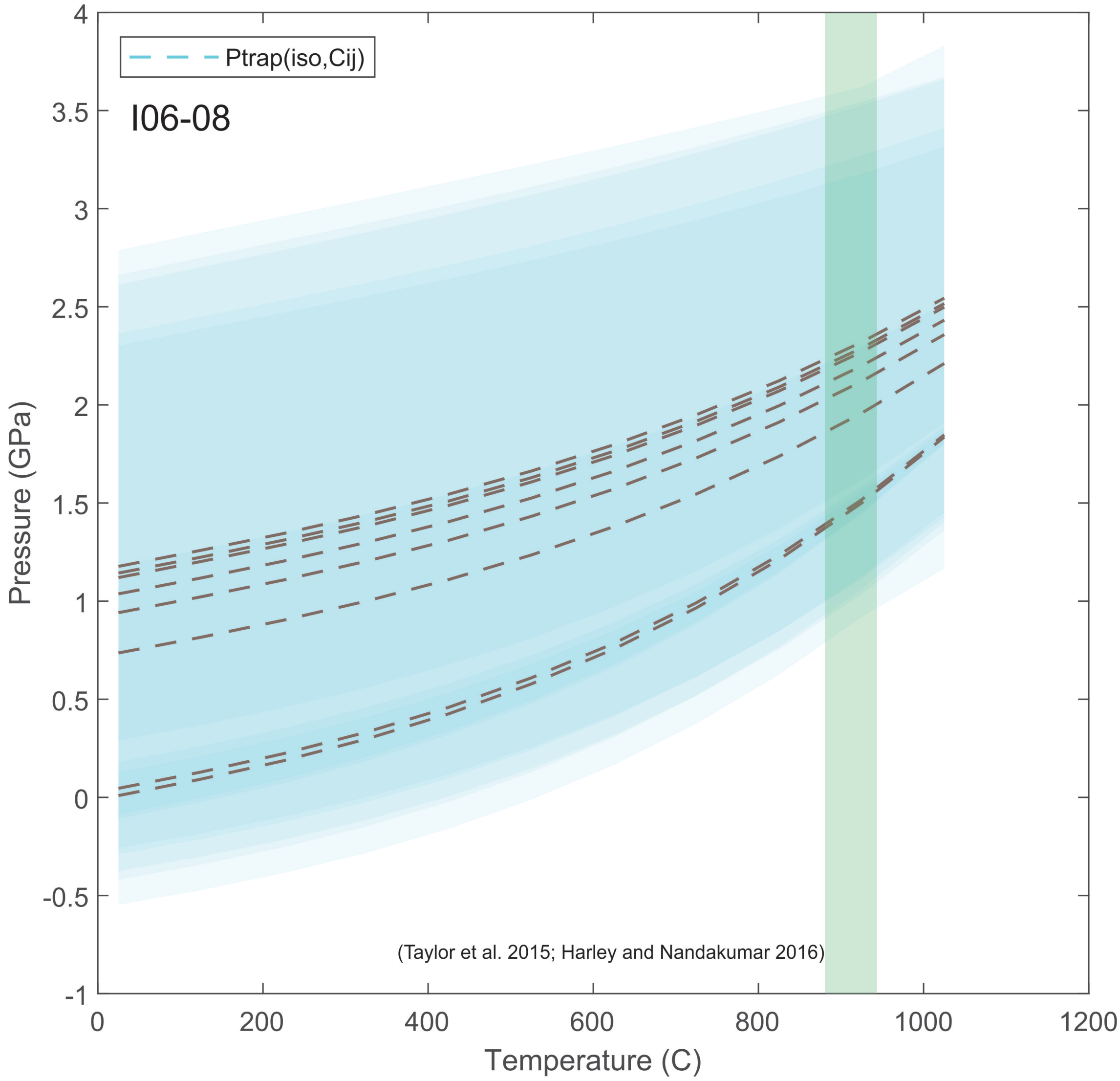

Figure 13: P-T isomekes for sample I06-08 calculated using RAMAN Spectroscopy of quartz inclusions, with the temperatures from the published literature in the Trivandrum Block (Taylor et al. 2015; Harley and Nandakumar 2016) as overlays for identifying possible pressures at peak P-T conditions

ISOSTASY RESULTS

Compositional Isostasy Results

Sample Number	Location	Latitude	Longitude	Pressure (kbar)	Err (kbar)	Depth (km)	Compositional Elevation (km)
I06-08	Trivandrum Block	9.012306	76.877417	14	5	51.92	7.08
I06-83	Northern Madurai Block	10.281639	77.534361	12.5	2	48.04	6.55

Table 4: Table summary detailing the pressure results for RAMAN spectroscopy using a maximum temperature of 950–1100°C for sample I06-83 (Collins et al. 2007; Prakash, Prakash, and Sachan 2010), and a maximum temperature of 900–950°C (Taylor et al. 2014; Harley and Nandakumar 2016). As well as the depths associated and the relative elevation after adjustment for isostasy.

Final Data Table	Peak Age (Ma)	Err (Ma)	Press. (Kbar)	Err (Kbar)	Depth (Km)	Elevation Gradient (km)	Modern Elevation Correction	Reference	Seisimc Profile Reference
India, Madagascar & Sri Lanka	521	21	9.1	0.2	33.37	3.62	3.62	Jons et al, 2006	Rindraharisaona et al. 2017
	534	44	11.2	1.8	42.15	4.99	5.54	Jons & Schenk 2011	Rindraharisaona et al. 2017
	612.3	4.8	12.8	2.2	48.42	5.41	6.83	Jons & Schenk 2007	Rindraharisaona et al. 2017
	539	6	8.7	0.7	34.36	3.64	4.21	Raase & Schenk, 1994, Kroner & Williams 1993	Dreiling et al. 2020
	539	6	6.05	0.85	24.27	2.34	2.45	Raase & Schenk, 1995	Dreiling et al. 2020
	535	4.9	11.5	1.5	39.38	5.37	7.13	Collins et al 2007	Vijaya Rao et al. 2006
	521	8	11.15	1.05	41.50	5.66	5.85	Prakash et al, 2010	Vijaya Rao et al. 2006
	544	5	6.4	0.2	36.93	5.04	5.09	Harley & Nandakumar 2016	Vijaya Rao et al. 2006
	546.7	5.9	11	2	44.50	6.07	7.14	Li et al. 2020	Vijaya Rao et al. 2006
Arabian Nubian Shield	760		7.15	0.35	26.06	2.15	2.97	Abu El-Rus et al 2008	Mooney ad Healey, 1986
	632	3	4.5	0.5	16.13	0.91	1.57	Eliwa, Abu El-Einen, Kahlaf and Murata 2008, Stern and Manton 1987	Hansen et al. 2007
	676		5.4	0.8	17.93	1.15	1.82	Abu-Alam et al 2014	Hansen et al. 2007
	620	6	5.6	0.3	21.15	1.59	2.26	Abu-Alam et al 2014	Hansen et al. 2007
	750		5.35	1.55	24.74	2.08	2.75	Abu-Alam et al 2014	Hansen et al. 2017
	635	15	4.8	1.2	14.34	0.66	1.33	Abu-Alam et al 2014	Hansen et al. 2017
	587		7.5	0.5	29.06	3.97	4.47	Whitehouse and Abu-El-Einen 2014	Saleh et al. 2006
	632	3	4.95	0.95	16.26	2.22	2.59	Eliwa, Abu El-Einen, Kahlaf and Murata 2008, Stern and Manton 1987	Qureshi 1971

	625	5	4.6	0.3	16.36	1.43	1.93	Abu Sharib et al. 2013	Saleh et al. 2006
	582	0.2	7.5	0.5	27.74	3.00	3.34	Stern 2018	Saleh et al. 2006
	593	4	7	0.5	24.79	2.68	3.16	Stern 2018	Saleh et al. 2006
	620	6	5.8	0.1	21.43	1.66	2.16	Elisha, Katzir and Kylander-Clark 2017	Hansen et al. 2007
	625		5.5	0.5	19.88	1.25	1.74	Jarrar et al. 2013	Hansen et al. 2007
	602		5.75	0.25	18.91	1.06	1.45	Karmaker and Schenk (2015b)	Hansen et al. 2007
	593	5	8	0.5	27.51	2.94	4.53	Andersson et al. 2006	Mahatsente et al. 1999
	593	5	9	0.5	31.32	3.45	5.12	Andersson et al. 2007	Mahatsente et al. 2000
	590	6	8.2	1	28.53	3.07	4.74	Johnson et al. 2004	Mahatsente et al. 1999
	533	12	8.1	2.1	28.19	3.03	4.70	Johnson et al. 2004	Mahatsente et al. 1999
	604	6	8.6	2.2	29.93	3.26	4.93	Johnson et al. 2004	Mahatsente et al. 1999
Mozambique Belt	629	6.8	10.9	0.2	39.17	4.16	4.16	Hauzenberger et al. 2005, Hauzenberger et al 2007	Simyu and Keller. 1994
	644	15	12	0.3	43.13	4.69	4.69	Hauzenberger et al. 2005, Hauzenberger et al 2007	Simyu and Keller. 1994
	638	1.8	7.88	0.1	28.32	2.68	2.68	Hauzenberger et al. 2005, Hauzenberger et al. 2007	Simyu and Keller. 1994
	640		12.5	0.5	46.72	5.18	5.18	Sommer et al, 2003	Simyu and Keller. 1994
	635	15	10.25	0.75	39.53	4.20	4.20	Appel et al, 1998	Simyu and Keller. 1994
	593	20	11	3.5	41.63	4.59	4.59	Boniface and Schenk 2012	Simyu and Keller. 1994
	642	0.9	8.5	2.5	55.49	6.44	6.44	Sommer, Kroner and lowry 2017	Simyu and Keller. 1994
	557	16	15.7	1.4	56.42	7.69	7.69	Engvik et al, 2007	Thor Leinweber et al. 2013
	575	1	12.3	1.5	54.27	7.40	7.40	Engvik et al, 2007, Kroner 2001 (AGE)	Thor Leinweber et al. 2013

555	11	9.2	1.8	34.86	4.75	4.75	Viola et al 2009	Thor Leinweber et al. 2013
596	11	11.8	1.8	50.31	6.86	6.86	Viola et al 2009	Thor Leinweber et al. 2013

Table 5: Compositional isostasy calculations for the data collected from the published data across the areas of the EAO, corrected where necessary to the modern elevation above sea level detailing the relevant data sources of the P-t and density data associated with the definition of the crustal columns. The *Fig. 14-16 (reconstructions)* use this data.

Error Results

Parameter		
Pressure	**Change (kbar)**	**Resultant Change Elevation (km)**
	1	0.52
	0.5	0.26
Density at depth	**Change (kg/m³)**	
	50	0.11
	100	0.23
Weighted Modern Crust Density	**Change (kg/m³)**	
	50	0.64
	100	1.29

Table 6: Summary table displaying the individual effect of change in each parameter on the resultant elevation after application of the compositional isostasy equation.

DISCUSSION

Uncertainties in data, Assumptions and Limitations

This thesis is a first attempt at calculating elevations for terranes and therefore like any pilot study, assumptions must be made. These assumptions are made at multiple stages within the process. Each parameter used in the building of the crustal column has its own individual assumptions, limitations and uncertainties. Understanding these assumptions, limitations and uncertainties is as important as the model itself and therefore, will be discussed below.

P-T CONDITIONS

The P–T conditions were collated from published literature and from this comes a level of uncertainty. Many of the terranes have had little work done on them, and often the studies undertaken have used outdated methods, or do not provide the information required to effectively control the quality of data. In some cases, determining whether the quoted age represents peak metamorphism is difficult to ascertain due to the ambiguity within the literature. It is important to also note, that in some published literature data, extremely low geothermal gradients were avoided, as they likely represent evidence for subduction-zone metamorphism, which do not represent a crust in isostatic equilibrium.

When applying the isostasy equation to the dataset, caution was taken through accounting for the uncertainties on each parameter involved and how each parameter separately changes the final result *Table 6.*

Large regions of the EAO lacked adequate metamorphic data, or metamorphic data linked to age constraints. This limits the regional resolution of this study. Additionally the peak pressures used are assumed to be an exclusive result of gravitational forces alone in $Eq. 1$. No non-gravitational forces were accounted for in the collisional environment. Adjusting the result to account for these forces should be considered in future studies of this nature. A summary of the assumed parameters is found in the methods (*see Table 1).*

ASSUMPTIONS ON THE CRUSTAL STRUCTURE AND COMPOSITION

The composition of the crustal columns were determined via the use of crustal structure analysis of seismic surveys for the modern crust. This allowed for observed estimation of the physical properties through the crust, including changes in layer thickness. The interpolation of the P-T data discussed above is used to identify the area, the metamorphic facies and its composition, this allows for large areas to be assigned as being at the same depth. To improve upon this assumption and remove this limitation, high quality surface surveys, seismic surveys and mapping of the region should be considered.

The composition of the eroded crust for the ancient crust was estimated simply to be a generic felsic crust with homogenous density (2850 kg/m^2), with standard values for thermal conductivity, heat production, heat flow and layer thicknesses (*Appendix C*). The uncertainty in the calculation surrounding changes in each parameter in terms of how they affect the compositional elevations is shown above in *Table 6*.

The compositional isostasy methods have their parameters defined by the composition and layer structure of the crustal columns. Consequentially, a reduction of uncertainty and or limitations on the collection of these parameters is necessary to improve upon the results. To reduce the number and magnitude of assumptions a more detailed understanding of crustal layouts and the geological background is needed.

The Moho depth was assumed to be representative of the total crustal thickness for the modern crust, which was stacked below the hypothetical crustal column based off the depth calculations obtained from the P-t data. The Moho was assumed to be static and to change relative to the modern depth plus the above (eroded) crust. No other factors influencing the Moho depth were taken into consideration.

ANALYTICAL APPROACH

Obtaining these parameters manually by applying the 'analytical methodology' also has its assumptions, limitations and uncertainties.

The collection of the pressures calculated from quartz inclusions using RAMAN spectroscopy may not be associated with the peak assemblage, suggesting pressures may not be directly associated with the 'peak age' calculated using the Lu–Hf dating method (Godet et al. 2021).

This study's purpose was to simply characterise pressure-time data from garnets alone. Understanding the full P-T-t history of the mineral assemblages and undertaking petrochronological studies would be preferable, but less practical in collecting numerous spatial data.

COMPOSITIONAL AND THERMAL ISOSTASY

The compositional isostasy results in *Table 5* show elevations with systematic variability based on their input pressures and densities, which give relatively applicable elevations for the reconstructions uncorrected to the thermal isostatic gradient. The uncertainties on these are relatively large and are affected by changes in the pressures, which for every 1 kbar change, there is a change of approx. 0.516 km elevation change. The densities associated with these rocks are less effective on the final elevation for every 50 kg/m^3 the final elevation changes by approx. 0.111 km. A change in the total weighted density for the modern crustal column, causes large changes in the elevation greatly in which every 50 kg/m^3 change, the final elevation changes by approx. 0.645 km.

The thermal isostasy adjustment can, in theory, adjust the compositional component to account for the thermal effect on the crustal buoyancy. In this study , however, calculating the reference and observed geotherms in a steady state environment is not supported due to a mismatch in heat production between the two crustal columns and the total crustal thickness. To achieve better results on the thermal isostasy, calculating each geotherm needs further study on each of the crustal columns and the thermal properties on the surface rocks must be better constrained.

Model Reconstructions and Elevations of the East African Orogen

The calculated elevations allow for global/regional paleo-geographic reconstructions, which are used to show the associated events in the latter stages. Georeferencing the modern locations to their approximate locations associated with their ages in deep time, details the multistage mountain building events of the EAO. The georeferenced reconstruction is based off a global tectonic (GPLATES) reconstruction from Merdith et al. (2021).

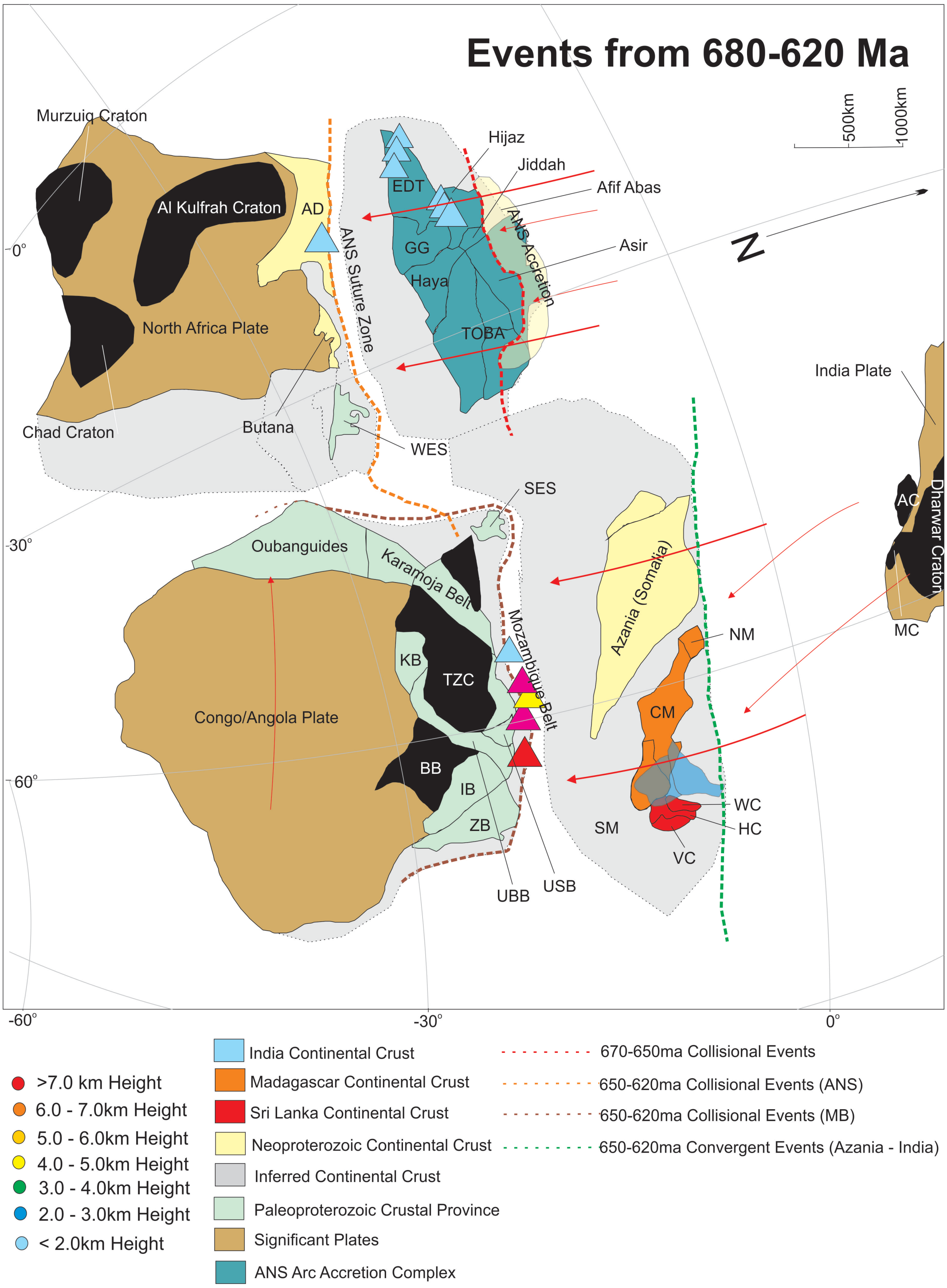

Figure 14: Paleogeographic Reconstruction of the first amalgamation events from ~680ma - 620ma, showing the separate events, involved crustal provinces, the present collision/suture zones along with the paleo-georeferenced elevations (Uncorrected), EDT: Egyptian Desert Terrane, AD: Atmur-Delgo, GG: Gebeit-Gabgaga, TOBA: Tokar-Barka Terranes, WES: Western Ethiopia Shield, SES: Southern Ethiopia Shield, KB: Kibaran Belt, TZC: Tanzania Craton, USB: Usagaran Belt, UBB: Ubendian Belt, BB: Bangwelu Block, IB: Irumide Belt, ZB: Zambesi Belt, SM: Southern Madagascar, CM: Central Madagascar, NM: Northern Madagascar, SGT: Southern Granulite Terrane, TNB: Trivandrum-Nagercoil Block, WC: Wanni Complex, HC: Highland Complex, VC: Vijayan Complex, AC: Antogil Craton, MC: Masora Craton. References for the data sources are listed in *Table 5*.

The earliest prevalent metamorphic data that was inverted is associated with accretionary orogenesis in the EAO that dates back to ~680 Ma. These ages are recorded in samples from across the Arabian-Nubian Shield (*see Table 5*). In the north, the extent and age of metamorphism is associated with the accretion ages of the Afif–Abas Terrane to the previously accreted western ANS platform.

The first paleo-elevation models (*Fig. 14*;~670–650 Ma) coincide with the final accretion and collision of the ANS (Collins et al. 2021). This involved the Afif–Abas microcontinent colliding with the western side of the already accreted ANS terrane, recording peak P-T conditions (in northern ANS) to ~5 kbar and ~600–700°C, which equates to approximately ~17 km depth. Applying this to a modern crust shows crustal thickening estimates of ~45–50 km. From this, the compositional isostasy of the columns suggests an approximate 1.15 km above sea level (see *Fig. 14).*

At approximately ~650–620 Ma, metamorphism was seemingly more widespread throughout the northern ANS, implying a major tectonic reorganisation (Meert 2003; Collins and Pisarevsky 2005). Peak pressures of 4–6 kbar and temperatures of up to 600–800°C were reported in assemblages across the ANS, causing burial to approximately 15–22 km depth. Application of this to the modern column produces a crustal thickness of ~44–53 km, and balancing this to a modern crustal column produces elevations from 0.6–2.2km (*Fig. 14*).

To the south in the Mozambique Belt rocks record higher peak pressures, ranging between 7.8–15 kbar and temperatures of ~750–850°C. Applying this to a crustal column produces crustal thicknesses ranging from ca. 68–93 km. Balancing this to a modern crustal column produces elevations of 2.6–6.5 km height (*Fig. 14*).

Both of these events in the ANS and the MB may have been associated with the continental collision of the Azanian microcontinent in the south with the amalgamated Archean and Paleoproterozoic crustal fragments of the Congo/Angola Plate (Collins and Pisarevsky 2005; Merdith et al. 2021). To the north, the collision did not appear to have the same intensity, but it still resulted in the closure of the ocean basin, separating the ANS from the Archean/Paleoproterozoic crustal fragments of the North Africa plate (Blades et al. 2021).

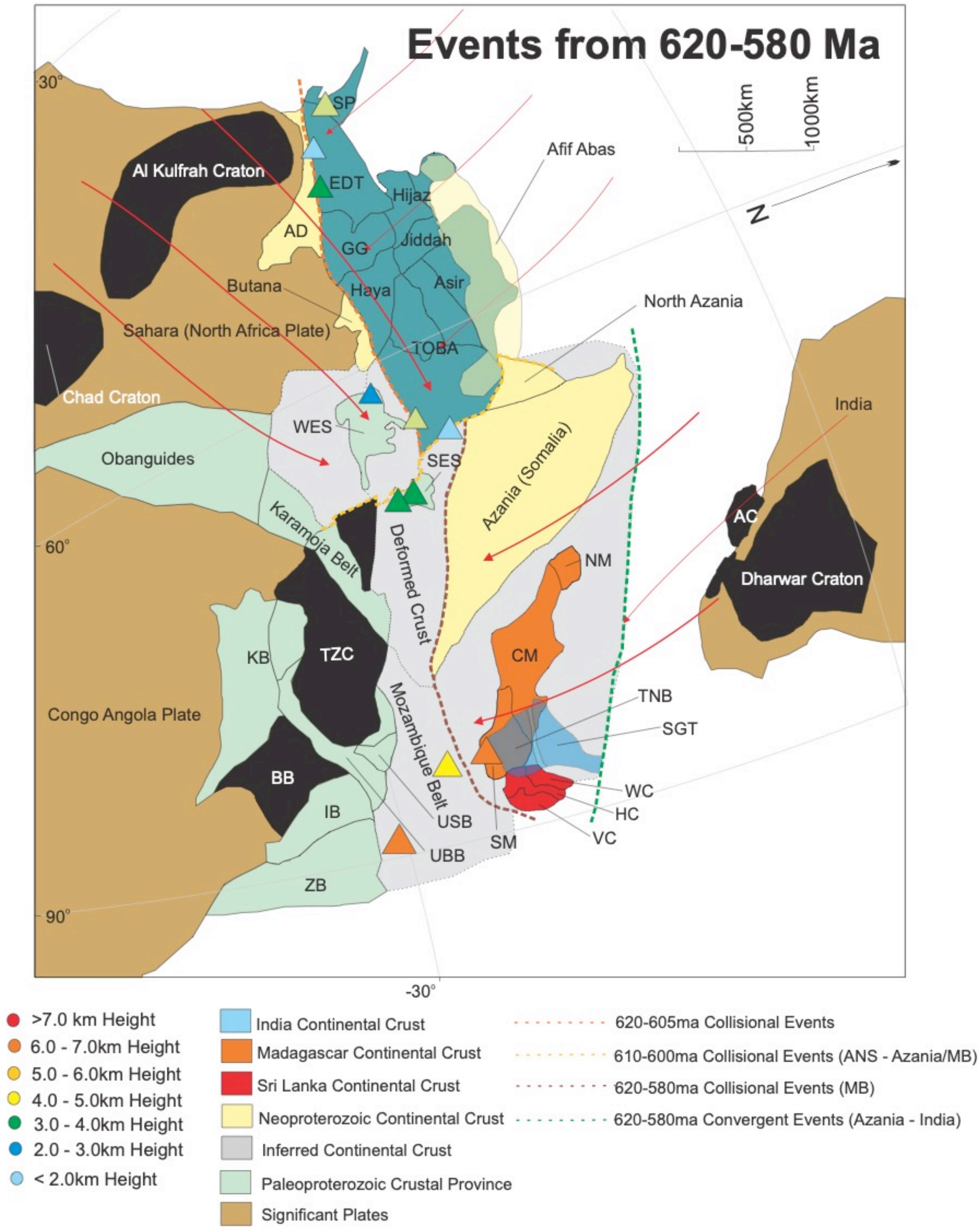

Figure 15: Paleogeographic Reconstruction of the first amalgamation events from ~680ma - 620ma, showing the separate events, involved crustal provinces, the present collision/suture zones along with the paleo-georeferenced elevations (Uncorrected), EDT: Egyptian Desert Terrane, AD: Atmur-Delgo, GG: Gebeit-Gabgaga, TOBA: Tokar-Barka Terranes, WES: Western Ethiopia Shield, SES: Southern Ethiopia Shield, KB: Kibaran Belt, TZC: Tanzania Craton, USB: Usagaran Belt, UBB: Ubendian Belt, BB: Bangwelu Block, IB: Irumide Belt, ZB: Zambesi Belt, SM: Southern Madagascar, CM: Central Madagascar, NM: Northern Madagascar, SGT: Southern Granulite Terrane, TNB: Trivandrum-Nagercoil Block, WC: Wanni Complex, HC: Highland Complex, VC: Vijayan Complex, AC: Antogil Craton, MC: Masora Craton. References for the data sources are listed in *Table 5.*

From ~620 Ma, published studies show many differing metamorphic constraints across the ANS, with pressures varying from 5.5–8.6 kbar and temperatures from 570–770°C. These have been modelled as depths ranging from 18–31 km. Application of the depths to a crustal column produces crustal thicknesses of ~49–60 km. Balancing this to a modern crust produces elevations ranging from 1–4 km. These are highly variable depending on their position and could be associated with the final amalgamation of the North African Plate, arc amalgamation and/or the movement of the amalgamated ANS towards the converging Azania and Congo/Angola Plates, creating a triple-junction collision at ~600 Ma (*see Fig. 15*).

In the Mozambique Belt, two locations record pressures to 12–14 kbar, modelling burial depths of ~41–50km, which when applied to the crustal column produce a crustal thickness of ~78–90 km. Balancing this to the modern crustal column produces elevations of ~4.6–6.8 km respectively for ages within this time domain. These are associated with the continuation of the Azanian microcontinent's southernmost collision with the Congo/Angola Plate (Collins et al. 2007; Merdith et al. 2021).

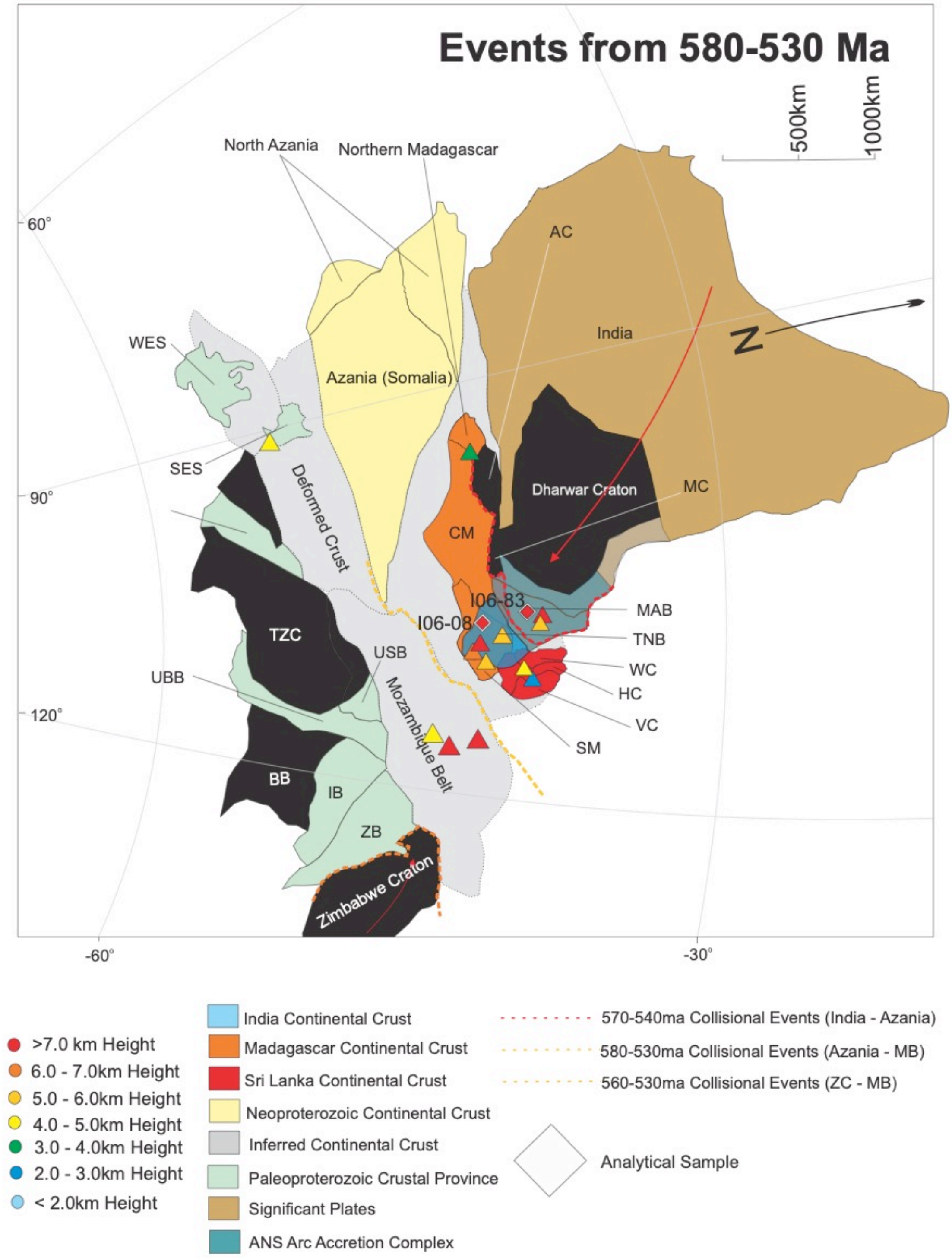

Figure 16: Paleogeographic Reconstruction of the first amalgamation events from ~580ma - 530ma, showing the separate events, involved crustal provinces, the present collision/suture zones along with the paleo-georeferenced elevations (Uncorrected), WES: Western Ethiopia Shield, SES: Southern Ethiopia Shield, KB: Kibaran Belt, TZC: Tanzania Craton, USB: Usagaran Belt, UBB: Ubendian Belt, BB: Bangwelu Block, IB: Irumide Belt, ZB: Zambesi Belt, SM: Southern Madagascar, CM: Central Madagascar, NM: Northern Madagascar, SGT: Southern Granulite Terrane, TNB: Trivandrum-Nagercoil Block, WC: Wanni Complex, HC: Highland Complex, VC: Vijayan Complex, AC: Antogil Craton, MC: Masora Craton. Also detailing the samples I06-08 and I06-83 compositional isostasy results. Referrences for data sources are listed in *Table 5.*

From ~580 the final amalgamation events of Gondwana were underway, producing peak metamorphic assemblages focussed in the MB. However, a second phase of orogenesis is also recorded in the southern ANS (Johnson et al. 2011a). Between ~580–530 Ma the rocks in the Mozambique Belt locally record pressures from 9.7–15.7 kbar, suggesting burial depths of ~34–36 km, Applying this to a crustal column produces a crustal thickness to 79–96 km, which when balanced to a modern crust produces uncorrected elevations ranging from 4.5–7.7 km. This extreme thickening is associated with the initiation of continual collision between the now amalgamated Azania and the Congo/Angola Plate and proto-India (Collins and Pisarevsky 2005; Merdith et al. 2021)(*see Fig. 16*). This is referred to as the Malagasy Orogeny (Collins 2006).

The event between the proto-Indian plate and the southern Azanian microcontinent in Madagascar/Sri Lanka/Modern Southern India at ~540 Ma, record pressures from 7–13 kbar producing depths of ~25–48 km. These correlate to a crustal column with crustal thicknesses ranging from 54–89 km, balancing this to a modern crustal column produces heights ranging from 2.3–6 km for ages associated with this final collision time domain (*Fig. 16*). The areas in the Mozambique Belt also have associated heights with the previous collisions, suggesting these were re-uplifted at the result of this Malagasy Orogeny.

The collision between India and Africa was the final event in the multistage formation of the EAO and thus, the amalgamation of Gondwana. In the north, the accretionary orogenesis in the ANS dominated the early-stage collisions, with mountain formation not exceeding ~2 km elevation until ~620 Ma. At this time, mountains reached ~2–4 km elevation throughout the mid-southern ANS. Further south, in the MB, contemporary summits are modelled to exceed ~7 km elevation. This magnitude of orogenesis lasted through to the ca. 540 Ma Malagasy Orogeny; the final collision to form central Gondwana, which caused a further uplift to similar heights. These elevations are analogous to those found in the modern Himalaya. I suggest that the southern EAO preserves evidence for Himalayan-scale mountain belts over ~100 Myr from ~630–530 Ma due to the two-stage collision as first Azania, then Neoproterozoic India, collided with the core of what is now central Africa.

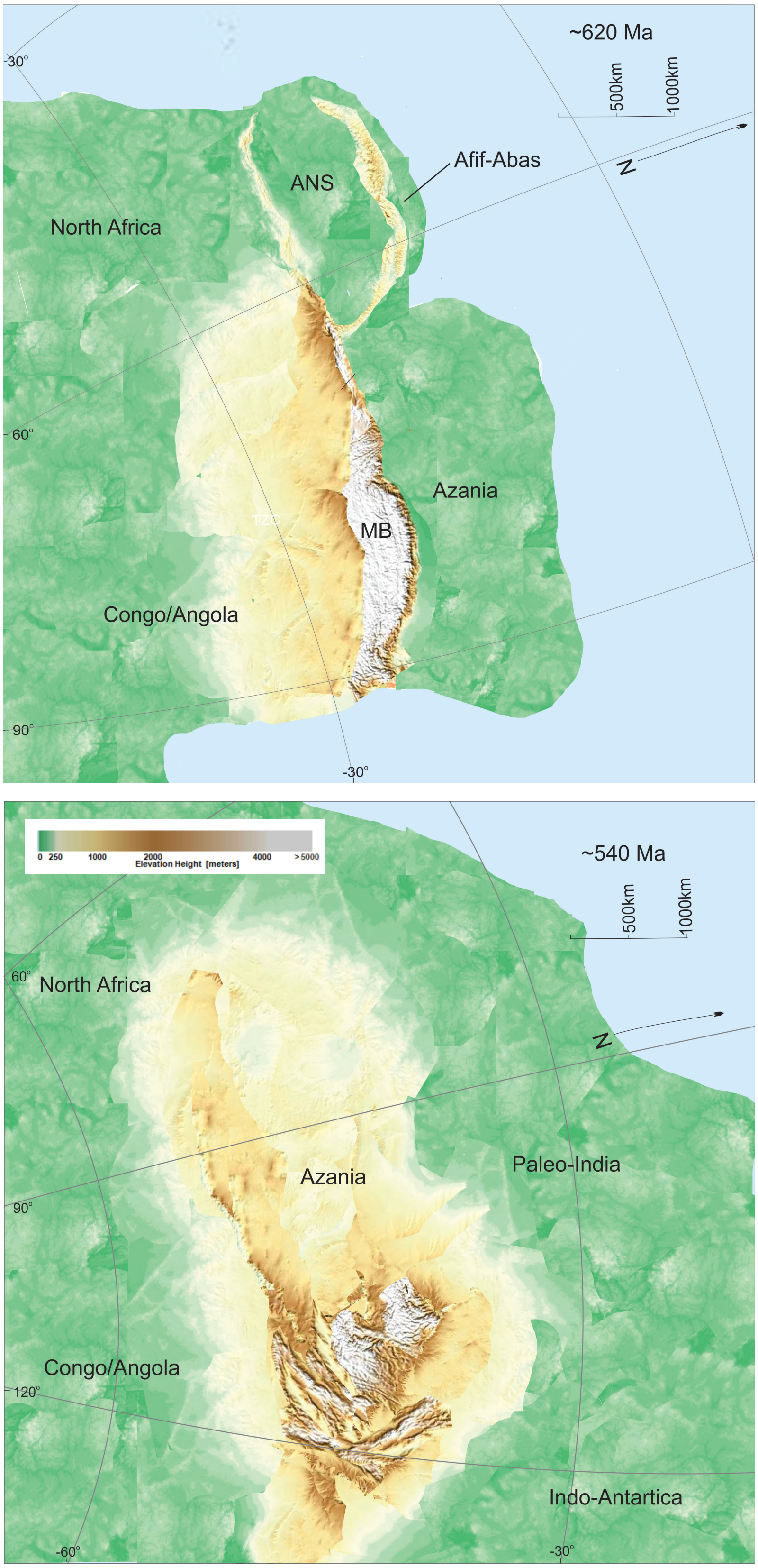

Figure 17: Schematic Paleo–Reconstructions of the times at which the mountain summits were greatest. During the formation of the Mozambique Belt (~620 Ma) and the Malagasy Orogeny (~540 Ma), Reconstructed from the models above (*Fig. 12; Fig 13*). This is a depiction of what future mountain reconstructions may look like.

THERMAL CORRECTIONS

A thermal correction on all these reconstructions would slightly increase each of the heights, producing higher mountain belts. These corrections, based on the region, would increase the elevations by up to 2 km higher than the compositional elevations.

The Trivandrum and Madurai Blocks of the Southern Granulite Terrain (a Case Study)

AGES AND METAMORPHIC CONDITIONS AND THEIR TECTONIC IMPLICATIONS

The final amalgamation of central Gondwana is widely accepted to be ~550 Ma through the collision of the Paleo-Indian continental crust (Dhawar, Antogil and Masora Cratons) with the Azanian microcontinent and its collision with the Congo craton *(see Fig.16).* Many of the provinces of southern India record this event including the Trivandrum and the Madurai Blocks of the Southern Granulite Terrain (*see Fig. 2*).

The Trivandrum Block is an elongate NW–SE trending gneiss complex that forms part of the SGT. It is bounded to the NE by the Anchankovil Shear Zone separating it from the southern Madurai Block and the Nagercoil Block to the SW. Each of these blocks preserve the latest Neoproterozoic to Cambrian (ca. 570–515 Ma) high grade metamorphic and deformational events associated with the amalgamation of eastern Gondwana. For this a peak metamorphic age of 544 ± 5 Ma (Harley and Nandakumar 2016) is comparable to the Lu–Hf garnet ages obtained in this study (I06-08; 591 ± 28.3 Ma). This age is supported by other studies in the Trivandrum block (Singh et al. 2010; Taylor et al. 2014; Taylor et al. 2015; Harley and Nandakumar 2016). The age obtained in this study, however, is slightly older than expected.

Sample IO6-02 from the Trivandrum Block preserves a Lu–Hf garnet age much older age than expected (1923.9 ± 159.7 Ma). Though this has a large uncertainty, it supports a Paleoproterozoic tectonothermal not yet previously recorded in this area, due to the Neoproterozoic-Cambrian overprint. Harley and Nandakumar (2016) however, suggest that the metasedimentary paragneisses in the Trivandrum Block are polymetamorphic, initially metamorphosed in the Paleoproterozoic in an event preceding the recognised 1.89–1.85 Ga granitic orthogenesis from the area, with a disconcordant zircon age at 1.92 Ga, providing evidence of this event.

Samples I06-83 and I06-38 are from the Northern Madurai Block, the northernmost province in the SGT. This, much like the Trivandrum Block, experienced metamorphism associated with the final collision in the EAO (~550–530 Ma). Studies in this area reveal peak metamorphic ages from metamorphic zircons of 535 ± 4.9 Ma (Collins et al. 2007). Lu–Hf garnet ages from these samples however, preserve relatively unprecise Neoproterozoic ages (I06-83, 601.5 ± 52.6 Ma; I06-38, 578.0 ± 131.3). Interpretations made from these data are, therefore, not precise enough to distinguish between the previous Azania–Congo collision (~650-550 Ma) or the widely recognised India–Azania/Congo collision (~550–530 Ma).

All the Lu–Hf results for the Neoproterozoic–Cambrian event produced ages of around ~600ma from analysis of whole garnets. All of these ages are interpreted to be the prograde-peak condition metamorphic ages and assumed to be associated with pressures calculated from the RAMAN spectroscopy (Godet et al. 2021).

Sample I06-106a maf from the Palghat Cauvery shear zone to the north of the Madurai Block did not produce precise Lu–Hf age data. However, the garnet contained monazite and rutile inclusions, these were dated to yield more precise ages of garnet growth across the P-t pathway. The monazites age of 535.41 ± 1.37, is interpreted to be a prograde–peak phase in the metamorphic pathway. This age is supported by previous work from these localities (Collins et al. 2007; Prakash 2008; Prakash, Prakash, and Sachan 2010) which recorded peak metamorphic ages of ~540 Ma. The rutile inclusions in garnet yield a U–Pb age of 452.9 ± 2.77 Ma, which is ~80 Myr younger than the monazite ages and likely represents a cooling age, whereby the associated collisional regime maintained its temperature at depth before cooling and disallowing further diffusion of Pb from the rutile, or alternatively may have undergone a reheating event (Kooijman et al. 2011; Zhang et al. 2014).

The age of metamorphism associated with this collision is interpreted to be the age of its prograde-peak conditions (Godet et al. 2021). Through RAMAN spectroscopy, peak pressures from samples I06-08 and I06-83 in the Trivandrum and Northern Madurai Blocks were calculated for their associated ages discussed above (I06-83, 601.5 ± 52.6 Ma, 591.0 ± 28.3 Ma. The quartz inclusions for sample I06-08 produced approximate peak pressures of ~14 +/- 5 kbar at constant temperatures of ~900°C– 950°℃, based on the thermometry presented in (Harley and Nandakumar 2016; Taylor et al. 2015; Taylor et al. 2014). The pressures lie within error of pressures calculated from thermobarometric studies in the Trivandrum Block and result in depths to approx. 50km, thus resulting in the relative elevation reaching approx. 7.5 km elevation.

The inclusions from I06-83 produced approximate peak pressures of ~12.5 +/- 3 kbar at a constant temperature of ~950–1100°C based on the thermometry studies undertaken in the Northern Madurai Block by (Prakash, Prakash, and Sachan 2010; Collins et al. 2007). This produces depths of ~36 km depth, producing isostatic elevations reaching ~5.1 km.

CONCLUSION

- The compositional isostasy calculates accurate bulk reconstructed elevations with the uncertainty weighing on the involved individual parameter errors e.g. pressure.

- The thermal component, in theory would make the crust more buoyant, thus the correction applied to the compositional isostasy would slightly increase the elevations calculated. In future studies the thermal isostasy should be calculated to account for all isostasy variables.

- The analytical workflow developed can be applied to any metamorphic rock bearing garnets. The potential of this workflow is significant and can be used as an efficient tool for collection of pressure-time data in large scale tectonic/topographic reconstructions.

- In terms of this study on the EAO, the outcomes distinctly show that paleo-elevations can be produced. When applying the method in future studies, however, consideration into the reduction of the assumptions, limitations and uncertainties must be taken into account. The analysis of the assumptions, limitations and uncertainties outlines where parts of this methodology can be improved by a more in depth review of the literature from the region as well as conducting surveys across the region of interest.

- The overall elevations across the amalgamation of Gondwana reveal that some areas in the EAO may have reached to similar heights to the Himalayas possibly even higher, thus confirming that the amalgamation event could be a collision style producing heights similar to that of the Himalayas.

- In the Arabian-Nubian Shield the results show much lower elevations up to 3 km from ~750 through to 600 Ma.

- In the Mozambique Belt and Madagascan/Indian belts much higher elevations were reached.
    - From ~630 Ma elevations in the Mozambique belt reached heights of up to ~7.5 km, through the coming together of the Azanian microcontinent and the Congo/Angola plate (*see Fig. 17*).
    - From ~540 Ma the formation of mountains in India and Madagascar reached elevations of up to ~8 km at result of the Malagasy Orogeny (Collins 2006)(*see Fig. 17*).

- These first paleo-topographic reconstructions show that the large-scale topography associated with the latter collisions in the amalgamation of Gondwana, may have played a significant role in the changes of climate throughout the Neoproterozoic-Cambrian time period.

ACKNOWLEDGMENTS

I would like to give my biggest thanks to supervisors Prof. Alan Collins and Dr. Derrick Hasterok, for their invaluable support, guidance and lifelong teachings they have given through the course of this project. Dr. Morgan Blades, is thanked for her continual academic inspiration, scientific and emotional support throughout the year. Prof. Chris Clark and Sean Makin from Curtin University are thanked for their help with the RAMAN spectroscopy they conducted on samples. Alex Simpson is thanked for his help with Lu–Hf LA-ICP-MS/MS analyses and data processing. Mitchell Bockman is thanked for his support with SEM imaging and LA-ICP-MS analysis of samples. Dr. Ben Wade and Dr. Sarah Gilbert are thanked for their help and with Tornado XRF and LA-ICP-MS analyses of samples. I would also like to thank the honours cohort for making the final year of undergrad a memory I will never forget.

REFERENCES

Abu El-Enen, Mahrous M., and Martin J. Whitehouse. 2013. 'The Feiran–Solaf metamorphic complex, Sinai, Egypt: Geochronological and geochemical constraints on its evolution', *Precambrian Research*, 239: 106-25.

Abu Sharib, Ahmed, Ayman Maurice, Yasser Abd El-Rahman, Ioan Sanislav, B. Schulz, and Bottros Bakhit. 2018. 'Neoproterozoic arc sedimentation, metamorphism and collision: Evidence from the northern tip of the Arabian-Nubian Shield and implication for the terminal collision between East and West Gondwana', *Gondwana Research*, 66: 13-42.

Abu-Alam, T. S., M. Hassan, K. Stüwe, S. E. Meyer, and C. W. Passchier. 2014. 'Multistage Tectonism and Metamorphism During Gondwana Collision: Baladiyah Complex, Saudi Arabia', *Journal of Petrology*, 55: 1941-64.

Airy, George Biddell. 1855. 'III. On the computation of the effect of the attraction of mountain-masses, as disturbing the apparent astronomical latitude of stations in geodetic surveys', *Philosophical Transactions of the Royal Society of London*, 145: 101-04.

Andersson, U. B., W. Ghebreab, and M. Teklay. 2006. 'Crustal evolution and metamorphism in east-central Eritrea, south-east Arabian-Nubian Shield', *Journal of African Earth Sciences*, 44: 45-65.

Angel, R. J., M. Murri, B. Mihailova, and M. Alvaro. 2019. 'Stress, strain and Raman shifts', *Zeitschrift Fur Kristallographie-Crystalline Materials*, 234: 129-40.

APPEL, P., A. MÖLLER*, and V. SCHENK. 1998. 'High-pressure granulite facies metamorphism in the Pan-African belt of eastern Tanzania: P–T–t evidence against granulite formation by continent collision', *Journal of Metamorphic Geology*, 16: 491-509.

Bingen, B., J. Jacobs, G. Viola, I. H. C. Henderson, Ø Skår, R. Boyd, R. J. Thomas, A. Solli, R. M. Key, and E. X. F. Daudi. 2009. 'Geochronology of the Precambrian crust in the Mozambique belt in NE Mozambique, and implications for Gondwana assembly', *Precambrian Research*, 170: 231-55.

Blades, Morgan L., Alan S. Collins, John Foden, Justin L. Payne, Kurt Stüwe, Tamer Abu-Alam, Farid Makroum, and Mahmoud Hassan. 2021. 'Age and hafnium isotope evolution of Sudanese Butana and Chad illuminates the Stenian to Ediacaran evolution of the south and east Sahara', *Precambrian Research*, 362: 106323.

Boger, S. D., W. Hirdes, C. A. M. Ferreira, Bernd Schulte, T. Jenett, and Christopher Fanning. 2014. 'From passive margin to volcano–sedimentary forearc: The Tonian to Cryogenian evolution of the Anosyen Domain of southeastern Madagascar', *Precambrian Research*, 247: 159–86.

Boniface, Nelson, and Volker Schenk. 2007. 'Polymetamorphism in the Paleoproterozoic Ubendian Belt, Tanzania', *Geochimica et Cosmochimica Acta*, 71: A107.

———. 2012. 'Neoproterozoic eclogites in the Paleoproterozoic Ubendian Belt of Tanzania: Evidence for a Pan-African suture between the Bangweulu Block and the Tanzania Craton', *Precambrian Research*, 208-211: 72-89.

Boyd, R., Ø Nordgulen, R. J. Thomas, B. Bingen, T. BjerkgåRd, T. Grenne, I. Henderson, V. A. Melezhik, M. Often, J. S. Sandstad, A. Solli, E. Tveten, G. Viola, R. M. Key, R. A. Smith, E. Gonzalez, L. J. Hollick, J. Jacobs, D. Jamal, G. Motuza, W. Bauer, E. Daudi, P. Feitio, V. Manhica, A. Moniz, and D. Rosse. 2010. 'THE

GEOLOGY AND GEOCHEMISTRY OF THE EAST AFRICAN OROGEN IN NORTHEASTERN MOZAMBIQUE', *South African Journal of Geology*, 113: 87-129.

Chamberlin, TC. 1899. 'An attempt to frame a working hypothesis of the cause of glacial periods on an atmospheric basis (continued)', *The Journal of Geology*, 7: 667-85.

Chapman, D. S. 1986. 'Thermal gradients in the continental crust', *Geological Society, London, Special Publications*, 24: 63-70.

Clark, Chris, Alan S. Collins, Richard J. M. Taylor, and Martin Hand. 2020. 'Isotopic systematics of zircon indicate an African affinity for the rocks of southernmost India', *Scientific Reports*, 10: 5421.

Collins, Alan S. 2006. 'Madagascar and the amalgamation of Central Gondwana', *Gondwana Research*, 9: 3-16.

Collins, Alan S., Morgan L. Blades, Andrew S. Merdith, and John D. Foden. 2021. 'Closure of the Proterozoic Mozambique Ocean was instigated by a late Tonian plate reorganization event', *Communications Earth & Environment*, 2: 75.

Collins, Alan S., Chris Clark, and Diana Plavsa. 2014. 'Peninsular India in Gondwana: The tectonothermal evolution of the Southern Granulite Terrain and its Gondwanan counterparts', *Gondwana Research*, 25: 190-203.

Collins, Alan S., Chris Clark, K. Sajeev, M. Santosh, David E. Kelsey, and Martin Hand. 2007. 'Passage through India: the Mozambique Ocean suture, high-pressure granulites and the Palghat-Cauvery shear zone system', *Terra Nova*, 19: 141-47.

Collins, Alan S., and Sergei A. Pisarevsky. 2005. 'Amalgamating eastern Gondwana: The evolution of the Circum-Indian Orogens', *Earth-Science Reviews*, 71: 229-70.

Dreiling, Jennifer, Frederik Tilmann, Xiaohui Yuan, Christian Haberland, and S. W. Mahinda Seneviratne. 2020. 'Crustal Structure of Sri Lanka Derived From Joint Inversion of Surface Wave Dispersion and Receiver Functions Using a Bayesian Approach', *Journal of Geophysical Research: Solid Earth*, 125: e2019JB018688.

Elisha, Bar, Yaron Katzir, and Andrew Kylander-Clark. 2017. 'Ediacaran (~620Ma) high-grade regional metamorphism in the northern Arabian Nubian Shield: U-Th-Pb monazite ages of the Elat schist', *Precambrian Research*, 295: 172-86.

Eliwa, Hassan, Mahrous Abu El-Enen, I. Khalaf, Tetsumaru Itaya, and Mamoru Murata. 2008. 'Metamorphic evolution of Neoproterozoic metapelites and gneisses in the Sinai, Egypt: Insights from petrology, mineral chemistry and K–Ar age dating', *Journal of African Earth Sciences - J AFR EARTH SCI*, 51: 107-22.

Engvik, Ane K., Einar Tveten, and Arne Solli. 2019. 'High-grade metamorphism during Neoproterozoic to Early Palaeozoic Gondwana assembly, exemplified from the East African Orogen of northeastern Mozambique', *Journal of African Earth Sciences*, 151: 490-505.

Fritz, H., M. Abdelsalam, K. A. Ali, B. Bingen, A. S. Collins, A. R. Fowler, W. Ghebreab, C. A. Hauzenberger, P. R. Johnson, T. M. Kusky, P. Macey, S. Muhongo, R. J. Stern, and G. Viola. 2013. 'Orogen styles in the East African Orogen: A review of the Neoproterozoic to Cambrian tectonic evolution', *Journal of African Earth Sciences*, 86: 65-106.

Goddéris, Yves, Yannick Donnadieu, Sébastien Carretier, Markus Aretz, Guillaume Dera, Mélina Macouin, and Vincent Regard. 2017. 'Onset and ending of the late Palaeozoic ice age triggered by tectonically paced rock weathering', *Nature Geoscience*, 10: 382-86.

Godet, Antoine, Carl Guilmette, Loic Labrousse, Matthijs A. Smit, Jamie A. Cutts, Donald W. Davis, and Marc-Antoine Vanier. 2021. 'Lu–Hf garnet dating and the timing of collisions: Palaeoproterozoic accretionary tectonics revealed in the Southeastern Churchill Province, Trans-Hudson Orogen, Canada', *Journal of Metamorphic Geology*, 39: 977-1007.

Halverson, Galen P., Matthew T. Hurtgen, Susannah M. Porter, and Alan S. Collins. 2009. 'Chapter 10 Neoproterozoic-Cambrian Biogeochemical Evolution.' in Claudio Gaucher, Alcides N. Sial, Hartwig E. Frimmel and Galen P. Halverson (eds.), *Developments in Precambrian Geology* (Elsevier).

Hansen, Samantha, James Gaherty, Susan Schwartz, Arthur Rodgers, and A. Al-Amri. 2007. 'Seismic Velocity Structure and Depth-Dependence of Anisotropy in the Red Sea and Arabian Shield from Surface Wave Analysis', *Journal of Geophysical Research*, 113.

Harley, Simon, and V. Nandakumar. 2016. 'New evidence for Palaeoproterozoic High Grade Metamorphism in the Trivandrum Block, Southern India', *Precambrian Research*, 280.

Hasterok, Derrick, and David S. Chapman. 2007. 'Continental thermal isostasy: 1. Methods and sensitivity', *Journal of Geophysical Research: Solid Earth*, 112.

Hauzenberger, Christoph A., Jörg Robl, and Kurt StÜWe. 2005. 'Garnet zoning in high pressure granulite-facies metapelites, Mozambique belt, SE-Kenya : constraints on the cooling history', *European Journal of Mineralogy*, 17: 43-55.

Hauzenberger, Christoph A., Holger Sommer, Harald Fritz, Andreas Bauernhofer, Alfred Kröner, Georg Hoinkes, Eckart Wallbrecher, and Martin Thöni. 2007a. 'SHRIMP U–Pb zircon and Sm–Nd garnet ages from the granulite-facies basement of SE Kenya: evidence for Neoproterozoic polycyclic assembly of the Mozambique Belt', *Journal of the Geological Society*, 164: 189-201.

———. 2007b. 'SHRIMP U–Pb zircon and Sm–Nd garnet ages from the granulite-facies basement of SE Kenya: evidence for Neoproterozoic polycyclic assembly of the Mozambique Belt', *Journal of the Geological Society*, 164: 189.

Hilton, Robert G., and A. Joshua West. 2020. 'Mountains, erosion and the carbon cycle', *Nature Reviews Earth & Environment*, 1: 284-99.

Hoffman, Paul F., Dorian S. Abbot, Yosef Ashkenazy, Douglas I. Benn, Jochen J. Brocks, Phoebe A. Cohen, Grant M. Cox, Jessica R. Creveling, Yannick Donnadieu, Douglas H. Erwin, Ian J. Fairchild, David Ferreira, Jason C. Goodman, Galen P. Halverson, Malte F. Jansen, Guillaume Le Hir, Gordon D. Love, Francis A. Macdonald, Adam C. Maloof, Camille A. Partin, Gilles Ramstein, Brian E. J. Rose, Catherine V. Rose, Peter M. Sadler, Eli Tziperman, Aiko Voigt, and Stephen G. Warren. 2017. 'Snowball Earth climate dynamics and Cryogenian geology-geobiology', *Science Advances*, 3: e1600983.

Huntly Cutten, Simon P. Johnson, and Bert De Waele. 2006. 'Protolith Ages and Timing of Metasomatism Related to the Formation of Whiteschists at Mautia Hill, Tanzania: Implications for the Assembly of Gondwana', *The Journal of Geology*, 114: 683-98.

Jacobs, J., W. Bauer, and C. M. Fanning. 2003. 'Late Neoproterozoic/Early Palaeozoic events in central Dronning Maud Land and significance for the southern extension of the East African Orogen into East Antarctica', *Precambrian Research*, 126: 27-53.

Jarrar, Ghaleb, Thomas Theye, Najel Yaseen, Martin Whitehouse, Victoria Pease, and Cees Passchier. 2013. 'Geochemistry and P–T–t evolution of the Abu-Barqa Metamorphic Suite, SW Jordan, and implications for the tectonics of the northern Arabian–Nubian Shield', *Precambrian Research*, 239: 56-78.

Johnson, P. R., A. Andresen, A. S. Collins, A. R. Fowler, H. Fritz, W. Ghebreab, T. Kusky, and R. J. Stern. 2011a. 'Late Cryogenian–Ediacaran history of the Arabian–Nubian Shield: A review of depositional, plutonic, structural, and tectonic events in the closing stages of the northern East African Orogen', *Journal of African Earth Sciences*, 61: 167-232.

Johnson, Peter, Arild Andresen, Alan Collins, Abdel-Rahman Fowler, Harald Fritz, Woldai Ghebreab, Timothy Kusky, and Bob Stern. 2011b. 'Late Cryogenian–Ediacaran history of the Arabian–Nubian Shield: A review of depositional, plutonic, structural, and tectonic events in the closing stages of the northern East African Orogen', *Journal of African Earth Sciences - J AFR EARTH SCI*, 61: 167-232.

Johnson, Timothy E., Teklewold Ayalew, Aberra Mogessie, F. Johan Kruger, and Marc Poujol. 2004. 'Constraints on the tectonometamorphic evolution of the Western Ethiopian Shield', *Precambrian Research*, 133: 305-27.

JÖNS, N., and V. SCHENK. 2008. 'Relics of the Mozambique Ocean in the central East African Orogen: evidence from the Vohibory Block of southern Madagascar', *Journal of Metamorphic Geology*, 26: 17-28.

JÖNS, N., V. SCHENK, P. APPEL, and T. RAZAKAMANANA. 2006. 'Two-stage metamorphic evolution of the Bemarivo Belt of northern Madagascar: constraints from reaction textures and in situ monazite dating', *Journal of Metamorphic Geology*, 24: 329-47.

Jöns, Niels, and Volker Schenk. 2011. 'The ultrahigh temperature granulites of southern Madagascar in a polymetamorphic context: implications for the amalgamation of the Gondwana supercontinent', *European Journal of Mineralogy*, 23: 127-56.

Karmakar, Shreya, and Volker Schenk. 2015. 'Neoproterozoic metamorphic events along the eastern margin of the East Sahara Ghost Craton at Sabaloka and Bayuda, Sudan: Petrology and texturally controlled in-situ monazite dating', *Precambrian Research*, 269: 217-41.

Kooijman, Ellen, Dewashish Upadhyay, Klaus Mezger, Michael M. Raith, Jasper Berndt, and C. Srikantappa. 2011. 'Response of the U–Pb chronometer and trace elements in zircon to ultrahigh-temperature metamorphism: The Kadavur anorthosite complex, southern India', *Chemical Geology*, 290: 177-88.

Kröner, A, I Braun, and P Jaeckel. 1996. 'Zircon geochronology of anatectic melts and residues from a highgrade pelitic assemblage at Ihosy, southern Madagascar: evidence for Pan-African granulite metamorphism', *Geological Magazine*, 133: 311-23.

Kröner, A., and I. S. Williams. 1993. 'Age of Metamorphism in the High-Grade Rocks of Sri Lanka', *The Journal of Geology*, 101: 513-21.

Leinweber, Volker Thor, Frauke Klingelhoefer, Sönke Neben, Christian Reichert, Daniel Aslanian, Luis Matias, Ingo Heyde, Bernd Schreckenberger, and Wilfried Jokat. 2013. 'The crustal structure of the Central Mozambique continental margin—Wide-angle seismic, gravity and magnetic study in the Mozambique Channel, Eastern Africa', *Tectonophysics*, 599: 170-96.

Lenton, Timothy M., Richard A. Boyle, Simon W. Poulton, Graham A. Shields-Zhou, and Nicholas J. Butterfield. 2014. 'Co-evolution of eukaryotes and ocean oxygenation in the Neoproterozoic era', *Nature Geoscience*, 7: 257-65.

Li, Shan-Shan, Richard M. Palin, M. Santosh, E. Shaji, and T. Tsunogae. 2019. 'Extreme thermal metamorphism associated with Gondwana assembly: Evidence from sapphirine-bearing granulites of Rajapalayam, southern India', *GSA Bulletin*, 132: 1013-30.

Mahatsente, Rezene, Gerhard Jentzsch, and T. Jahr. 1999. 'Crustal structure of the Main Ethiopian Rift from gravity data: 3-dimensional modeling', *Tectonophysics*, 313: 363-82.

Markl, Gregor, Jürgen Bäuerle, and Djordje Grujic. 2000. 'Metamorphic evolution of Pan-African granulite facies metapelites from Southern Madagascar', *Precambrian Research*, 102: 47-68.

Mazzucchelli, Mattia Luca, Ross John Angel, and Matteo Alvaro. 2021. 'EntraPT: An online platform for elastic geothermobarometry', *American Mineralogist*, 106: 830-37.

Meert, Joseph. 2003. 'A synopsis of events related to the assembly of Eastern Gondwana', *Tectonophysics*, 362: 1-40.

Meert, Joseph G., Rob van der Voo, and Samwel Ayub. 1995. 'Paleomagnetic investigation of the Neoproterozoic Gagwe lavas and Mbozi complex, Tanzania and the assembly of Gondwana', *Precambrian Research*, 74: 225-44.

Merdith, Andrew S., Simon E. Williams, Alan S. Collins, Michael G. Tetley, Jacob A. Mulder, Morgan L. Blades, Alexander Young, Sheree E. Armistead, John Cannon, Sabin Zahirovic, and R. Dietmar Müller. 2021. 'Extending full-plate tectonic models into deep time: Linking the Neoproterozoic and the Phanerozoic', *Earth-Science Reviews*, 214: 103477.

Mills, Benjamin J. W., Yannick Donnadieu, and Yves Goddéris. 2021. 'Spatial continuous integration of Phanerozoic global biogeochemistry and climate', *Gondwana Research*.

Mills, Benjamin J. W., Alexander J. Krause, Christopher R. Scotese, Daniel J. Hill, Graham A. Shields, and Timothy M. Lenton. 2019. 'Modelling the long-term carbon cycle, atmospheric CO2, and Earth surface temperature from late Neoproterozoic to present day', *Gondwana Research*, 67: 172-86.

Möller, Andreas, Klaus Mezger, and Volker Schenk. 2000. 'U–Pb dating of metamorphic minerals: Pan-African metamorphism and prolonged slow cooling of high pressure granulites in Tanzania, East Africa', *Precambrian Research*, 104: 123-46.

Mooney, W. D., M. E. Gettings, H. R. Blank, and J. H. Healy. 1985. 'Saudi Arabian seismic-refraction profile: A traveltime interpretation of crustal and upper mantle structure', *Tectonophysics*, 111: 173-246.

Murri, M., M. L. Mazzucchelli, N. Campomenosi, A. V. Korsakov, M. Prencipe, B. D. Mihailova, M. Scambelluri, R. J. Angel, and M. Alvaro. 2018. 'Raman elastic geobarometry for anisotropic mineral inclusions', *American Mineralogist*, 103: 1869-72.

Plavsa, Diana, Alan S. Collins, John D. Foden, and Chris Clark. 2015. 'The evolution of a Gondwanan collisional orogen: A structural and geochronological appraisal from the Southern Granulite Terrane, South India', *Tectonics*, 34: 820-57.

Prakash, D. 2008. 'UHT metamorphism and its significance in Madurai block, South India'.

Prakash, D., S. Prakash, and H. K. Sachan. 2010. 'Petrological evolution of the high pressure and ultrahigh-temperature mafic granulites from Karur, southern India: evidence for decompressive and cooling retrograde trajectories', *Mineralogy and Petrology*, 100: 35-53.

Pratt, Archdeacon, and George Gabriel Stokes. 1859. 'II. On the deflection of the plumb-line in India caused by the attraction of the Himalaya mountains and the elevated regions beyond, and its modification by the compensating effect of a deficiency of matter below the mountain mass', *Proceedings of the Royal Society of London*, 9: 493-96.

Pratt, John Henry, and James Challis. 1855. 'I. On the attraction of the Himalaya Mountains, and of the elevated regions beyond them, upon the plumb-line in India', *Philosophical Transactions of the Royal Society of London*, 145: 53-100.

Qureshi, Iftikhar R. 1971. 'Gravity Measurements in the North-eastern Sudan and Crustal Structure of the Red Sea', *Geophysical Journal International*, 24: 119-35.

Raase, P., and V. Schenk. 1994. 'Petrology of granulite-facies metapelites of the Highland Complex, Sri Lanka: implications for the metamorphic zonation and the P-T path', *Precambrian Research*, 66: 265-94.

Rao, V., and Rajendra Bitragunta. 2006. 'Structure and evolution of the Cauvery Shear Zone system, Southern Granulite Terrain, India: Evidence from deep seismic and other geophysical studies', *Gondwana Research - GONDWANA RES*, 10: 29-40.

Ratheesh-Kumar, R. T., P. L. Dharmapriya, B. F. Windley, W. J. Xiao, and U. Jeevan. 2020. 'The Tectonic "Umbilical Cord" Linking India and Sri Lanka and the Tale of their Failed Rift', *Journal of Geophysical Research: Solid Earth*, 125: e2019JB018225.

Raymo, Maureen E., William F. Ruddiman, and Philip N. Froelich. 1988. 'Influence of late Cenozoic mountain building on ocean geochemical cycles', *Geology*, 16: 649-53.

Robinson, F. A., J. D. Foden, A. S. Collins, and J. L. Payne. 2014. 'Arabian Shield magmatic cycles and their relationship with Gondwana assembly: Insights from zircon U–Pb and Hf isotopes', *Earth and Planetary Science Letters*, 408: 207-25.

Shields, Graham. 2007. 'A normalised seawater strontium isotope curve: Possible implications for Neoproterozoic-Cambrian weathering rates and the further oxygenation of the Earth', *eEarth*, 2.

Simpson, Alexander, Sarah Gilbert, Renee Tamblyn, Martin Hand, Carl Spandler, Jack Gillespie, Angus Nixon, and Stijn Glorie. 2021. 'In-situ LuHf geochronology of garnet, apatite and xenotime by LA ICP MS/MS', *Chemical Geology*, 577: 120299.

Singh, Yengkhom, Bert Waele, Subrata Karmakar, Sunayana Sarkar, and Tapas Biswal. 2010. 'Tectonic setting of the Balaram-Kui-Surpagla-Kengora granulites of the South Delhi Terrane of the Aravalli Mobile Belt, NW India and its implication on correlation with the East African Orogen in the Gondwana assembly', *Precambrian Research*, 183: 669-88.

Sommer, H., A. Kröner, C. Hauzenberger, S. Muhongo, and M. T. D. Wingate. 2003. 'Metamorphic petrology and zircon geochronology of high-grade rocks from the central Mozambique Belt of Tanzania: crustal recycling of Archean and

Palaeoproterozoic material during the Pan-African orogeny', *Journal of Metamorphic Geology*, 21: 915-34.
Sommer, Holger, Alfred Kröner, and J. Lowry. 2017. 'Neoproterozoic eclogite- to high-pressure granulite-facies metamorphism in the Mozambique belt of east-central Tanzania: A petrological, geochemical and geochronological approach', *Lithos*, 284.
Squire, Richard, Ian Campbell, Charlotte M. Allen, and Christopher Wilson. 2006. 'Did the Transgondwanan Supermountain trigger the explosive radiation of animals on Earth?', *Earth and Planetary Science Letters*, 250: 116-33.
STERN, R. J., and W. I. MANTON. 1987. 'Age of Feiran basement rocks, Sinai: implications for late Precambrian crustal evolution in the northern Arabian–Nubian Shield', *Journal of the Geological Society*, 144: 569-75.
Stern, Robert J. 1994. 'Arc assembly and continental collision in the Neoproterozoic East African Orogen: implications for the consolidation of Gondwanaland', *Annual Review of Earth and Planetary Sciences*, 22: 319-51.
Taylor, Richard J. M., Chris Clark, Ian C. W. Fitzsimons, M. Santosh, M. Hand, Noreen Evans, and Brad McDonald. 2014. 'Post-peak, fluid-mediated modification of granulite facies zircon and monazite in the Trivandrum Block, southern India', *Contributions to Mineralogy and Petrology*, 168: 1044.
Taylor, Richard J. M., Chris Clark, Tim E. Johnson, M. Santosh, and Alan S. Collins. 2015. 'Unravelling the complexities in high-grade rocks using multiple techniques: the Achankovil Zone of southern India', *Contributions to Mineralogy and Petrology*, 169: 51.
Tenczer, V., Ch Hauzenberger, H. Fritz, G. Hoinkes, S. Muhongo, and U. Klötzli. 2013. 'Crustal age domains and metamorphic reworking of the deep crust in Northern-Central Tanzania: a U/Pb zircon and monazite age study', *Mineralogy and Petrology*, 107: 679-707.
Ueda, K., J. Jacobs, R. J. Thomas, J. Kosler, F. Jourdan, and R. Matola. 2012. 'Delamination-induced late-tectonic deformation and high-grade metamorphism of the Proterozoic Nampula Complex, northern Mozambique', *Precambrian Research*, 196-197: 275-94.
Viola, G., I. H. C. Henderson, B. Bingen, R. J. Thomas, M. A. Smethurst, and S. de Azavedo. 2008. 'Growth and collapse of a deeply eroded orogen: Insights from structural, geophysical, and geochronological constraints on the Pan-African evolution of NE Mozambique', *Tectonics*, 27.
Zhang, Jianxin, C. G. Mattinson, Shengyao Yu, and Yunshuai Li. 2014. 'Combined rutile-zircon thermometry and U-Pb geochronology: New constraints on Early Paleozoic HP/UHT granulite in the south Altyn Tagh, north Tibet, China', *Lithos*, 200.

APPENDIX A: ANALYTICAL SAMPLES

Samples were collected from a transect survey by Prof. Alan Collins in a 2006 Indian Geological field trip. The targeted samples were those with large enough garnets for analysis.

Locations	N	E	latitude	longitude
IO6-02	08 36 10.6	76 57 09.7	8.602944	76.952694
IO6-05	09 00 44.3	76 52 38.7	9.012306	76.877417
IO6-08	09 00 44.3	76 52 38.7	9.012306	76.877417
IO6-38	09 26 32.0	77 35 36.6	9.442222	77.5935
IO6-44	09 26 44.2	77 34 23.2	9.445611	77.573111
IO6-57	N 09 52 46.7	E 77 48 11.0	9.879639	77.803056
IO6-60	N 09 56 25.1	E 77 49 33.4	9.940306	77.825944
IO6-83	N 10 16 53.9	E 77 32 03.7	10.281639	77.534361
IO6-106	N 11 08 08.5	E 78 02 52.6	11.135694	78.047944

Appendix A 1: List of the Samples collected as part of the campaign-style analytical method.

These samples were prepared for geochronology and RAMAN spectroscopy by first obtaining individual garnets from each sample and setting them in individual Epoxy Resin Pucks as part of the standard sample preparation methodology. Proper safety precautions were taken throughout this process.

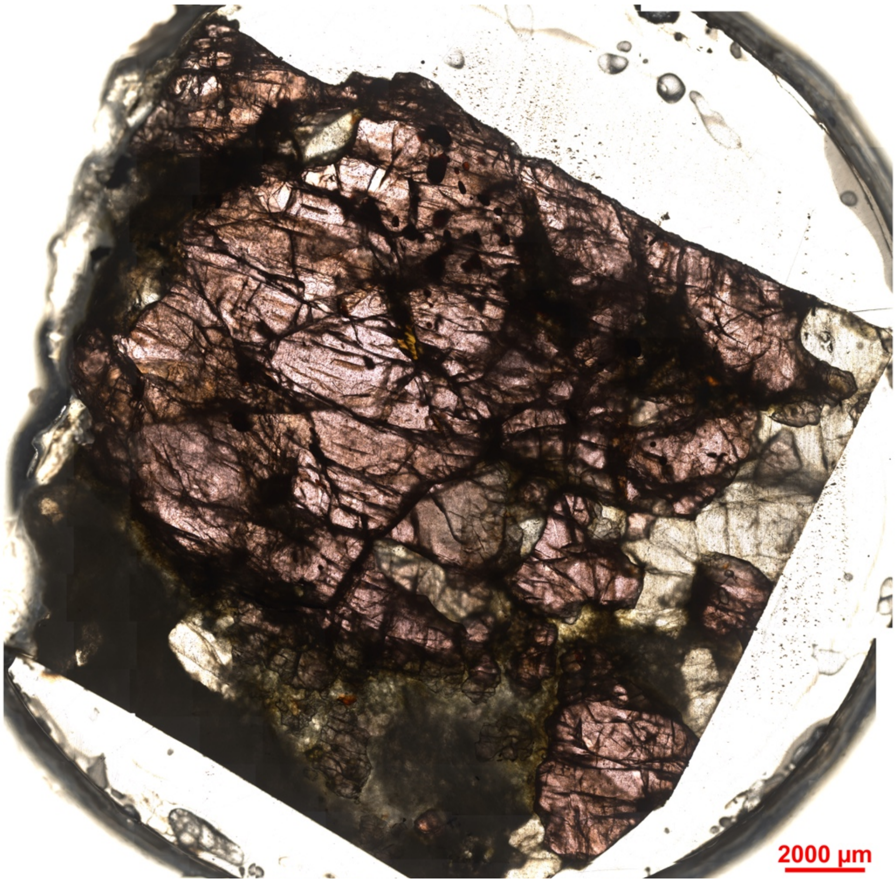

Appendix A 2: A garnet porphryoblast from sample I06-02: From a metapelitic granulite gneiss, with biotite rich layers ranging from 0.5 – 1cm thickness, with large 0.5 – 2cm garnet porphryoblasts within the biotite rich layers. The garnet is highly fractured and incudes quartz grainsof varying size

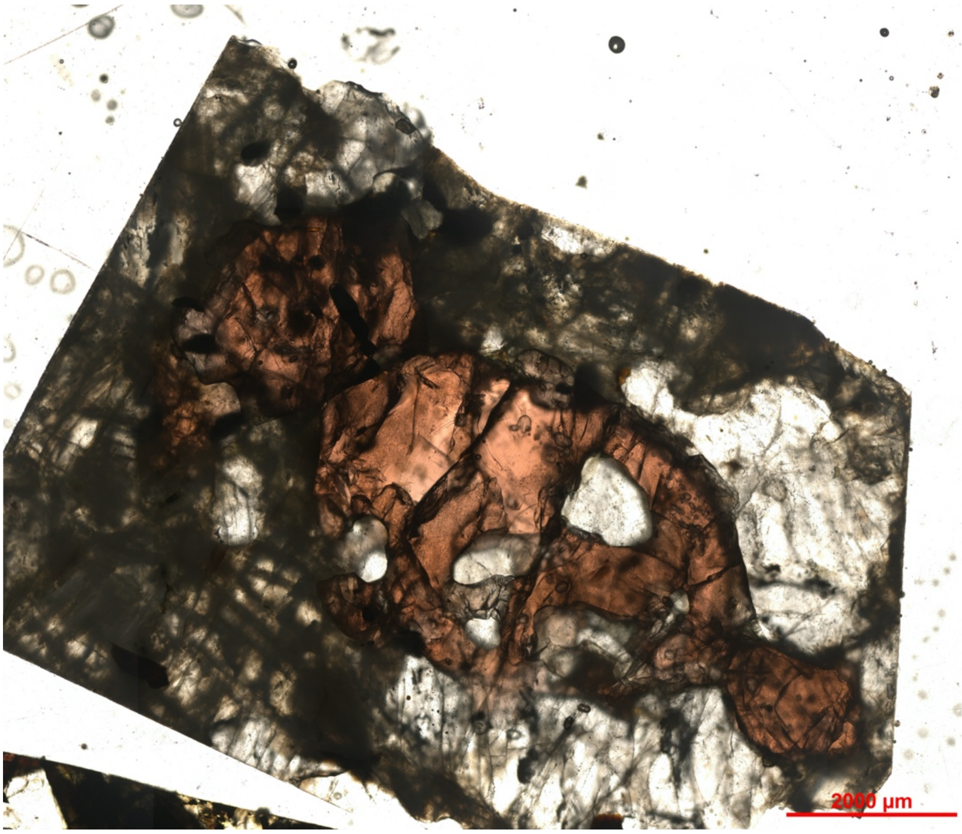

Appendix A 3: A garnet porphyroblast from sample I06-08: From a metapelitic schistose granulite, with thin interchanging mica rich layers and quartz layers (5mm). Garnet porphryoblasts are erratically placed throughout 5mm-10mm. The garnet porphryoblasts include large quartz inclusions relatively unfractured.

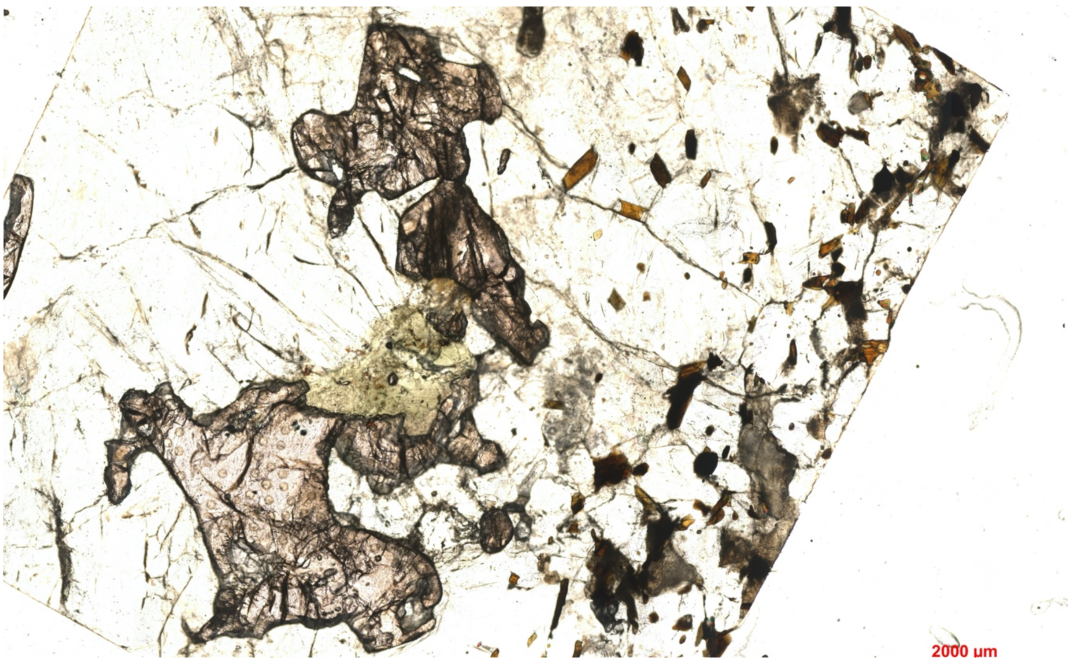

Appendix A 4: A garnet Porphyroblast from sample I06-38: From a metapelitic gneiss granulite, with thick biotite and quartz dominated layers, with small garnet porphryoblasts residing in the quartz dominated layers ranging from 5mm to 10 mm. small qtz inlcusions are in the garnet porphyroblast, however, the garnets are relatively fractured.

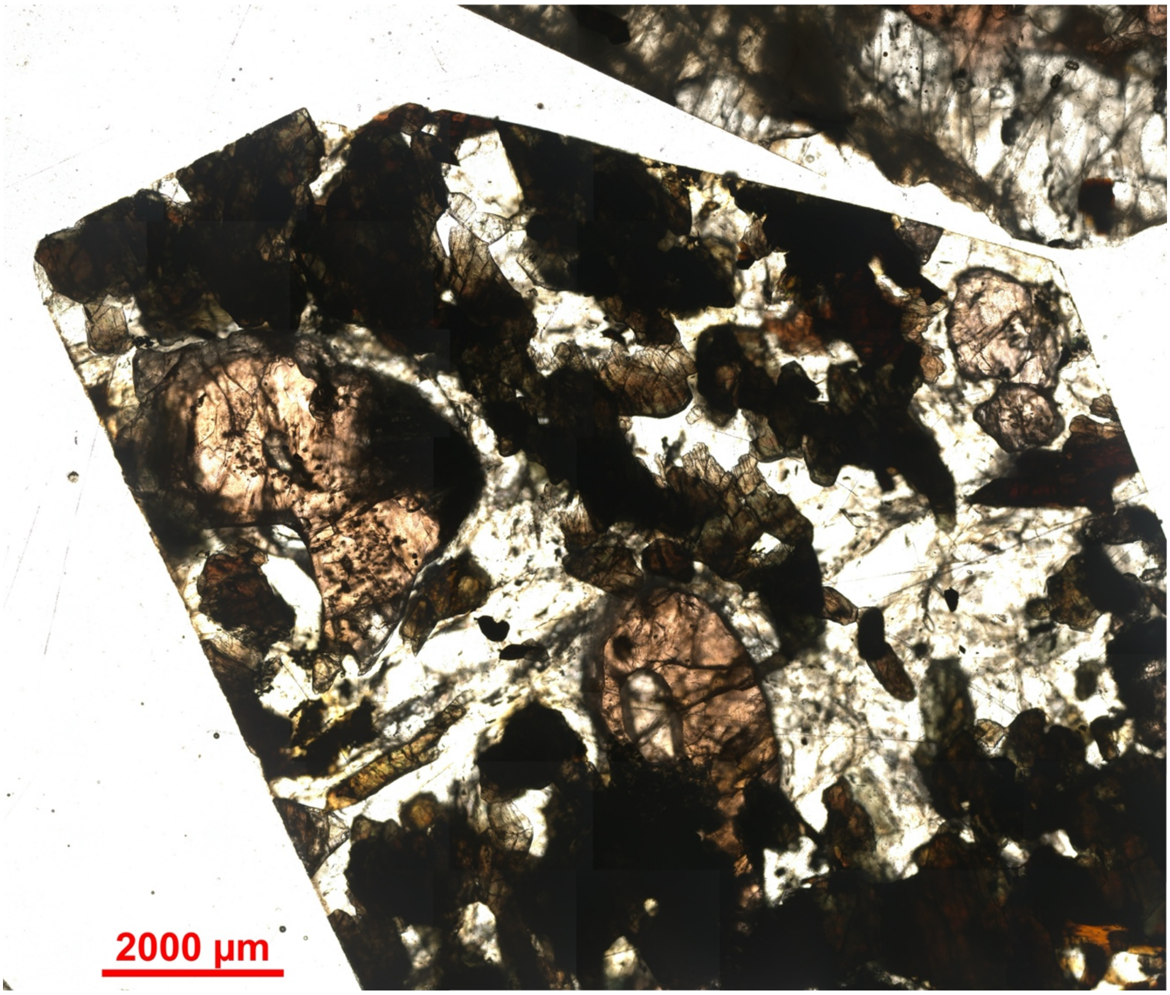

Appendix A 5: A garnet porphyroblast from sample I06-83: From a metabasic granulite schist, dominated by pyroxenes and biotite with quartz rimming the garnet porphryoblasts, the garnets themselves are relatively unfractured with quartz inclusions.

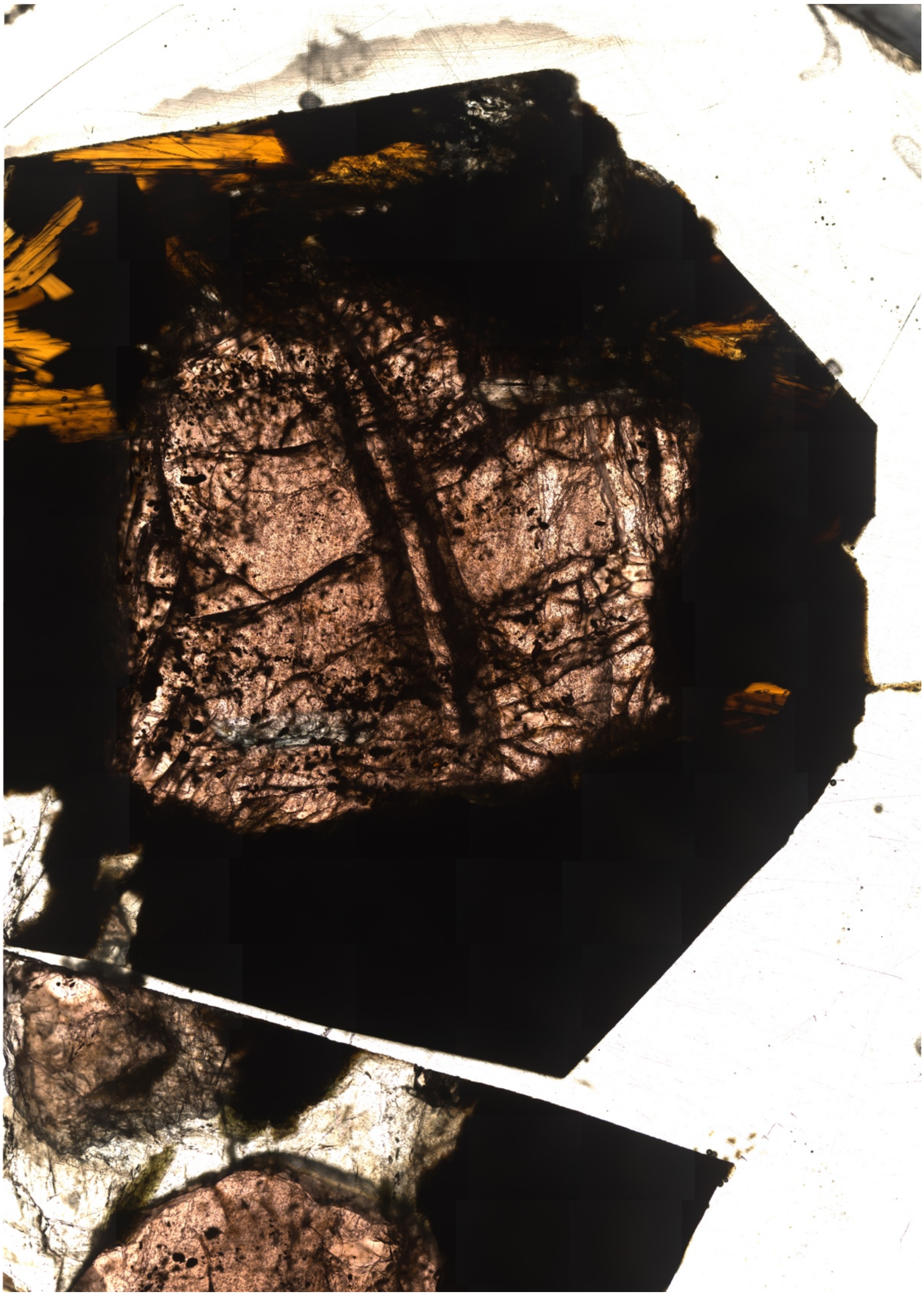

Appendix A 6: Garnet Porphyroblast from sample I06-106a maf: A metapelitic grnulite gneiss, with varying thick quartz and mica rich layers, the garnet porphryoblasts are varied in their placement throughout and had a fine inclusions assemblage of rutile and monazite, the analysed one in the sample seen above was found in a biotite rich layers.

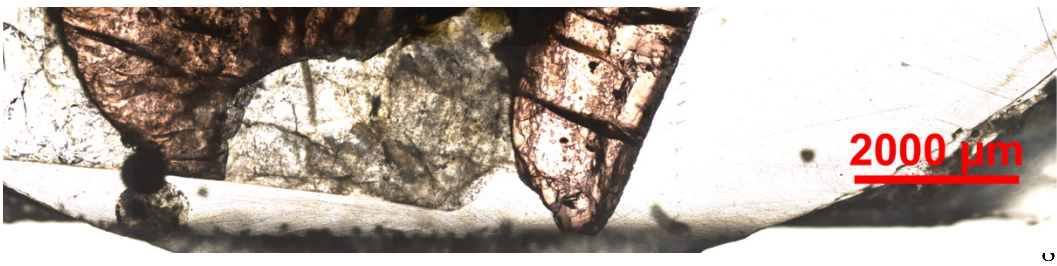

APPENDIX B: GEOCHRONOLOGY DATA

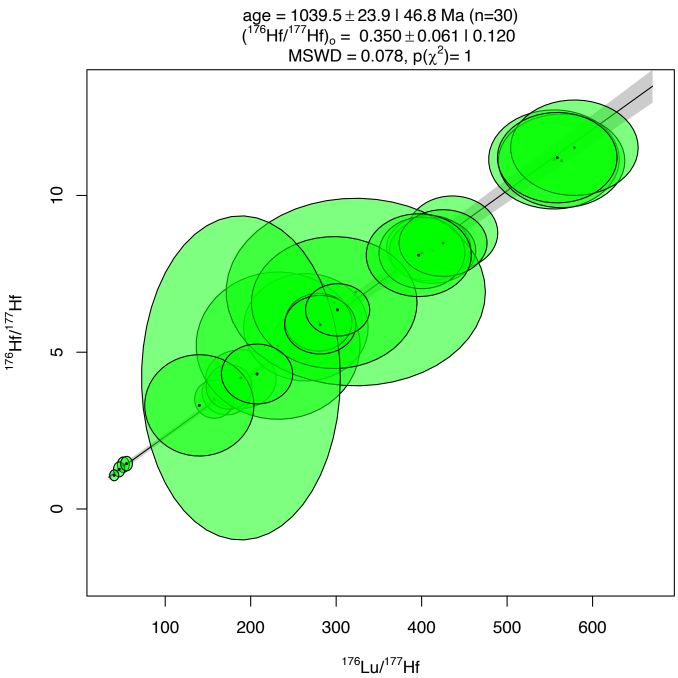

Appendix B 2: Calculated isochron Concordia age for standard Hogsbo

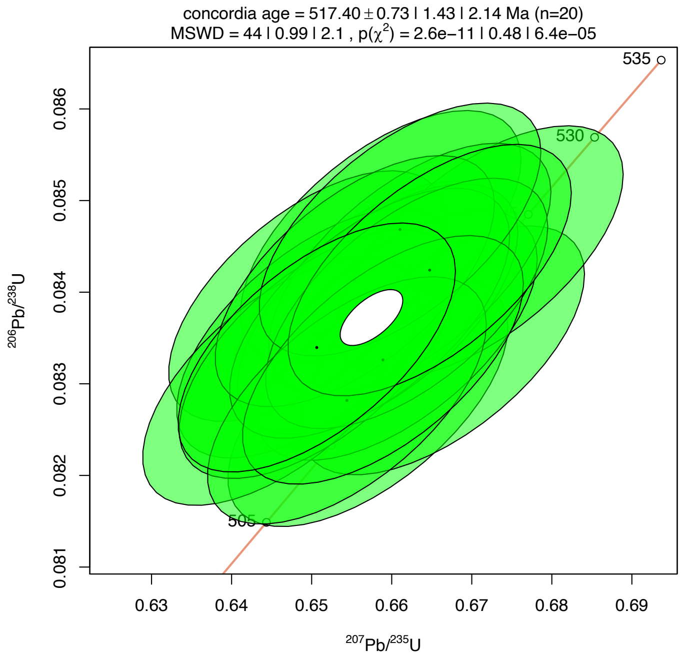

Appendix B 1: Calculated isochron Concordia age for standard MAdel

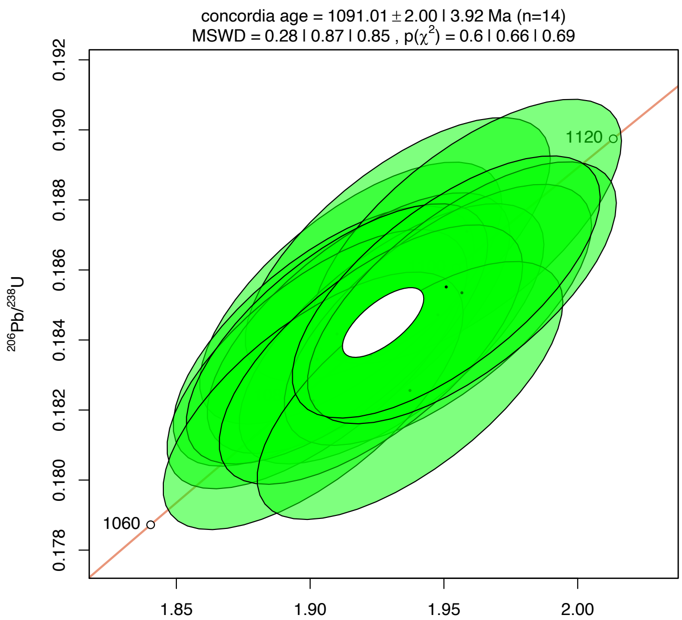

Appendix B 3: Calculated isochron Concordia age for standard R10

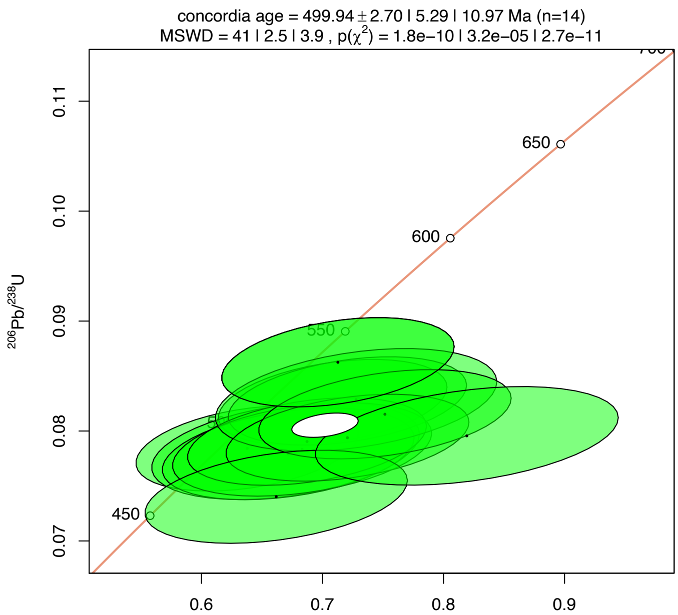

Appendix B 4: Calculated isochron Concordia age for standard R19

Sample	Analysis	206Pb/238U	206Pb/238U	207Pb/235U(calc)	207Pb/235U(calc)	238U/206Pb	238U/206Pb	207Pb/206Pb	207Pb/206Pb
IO6-106a Ru4 - 1	NIST610	0.086944122	0.029809625	0.654969853	0.075941207	11.52727412	0.336568828	0.054715266	0.006191729
IO6-106a Ru11 - 3	NIST610	0.074616893	0.00196104	0.571242487	0.027326182	13.43181422	0.309809834	0.055420924	0.002743478
IO6-106a Ru22 - 2	NIST610	0.074160203	0.001683119	0.585750304	0.026048481	13.45121655	0.300953474	0.056921616	0.002220038
IO6-106a Ru11 - 1	NIST610	0.073151439	0.001798615	0.577794106	0.027370487	13.69816087	0.321612157	0.057137962	0.002489139
IO6-106a Ru12 - 6	NIST610	0.07795303	0.001731493	0.624495798	0.025785557	12.82531609	0.262703061	0.058084793	0.002192478
IO6-106a Ru24 - 1	NIST610	0.0703629	0.00148144	0.553465904	0.025130687	14.22277835	0.330722659	0.056717036	0.00239484
IO6-106a Ru14 - 1	NIST610	0.080839318	0.002201269	0.655243604	0.026398743	12.35110857	0.281724373	0.058990749	0.002175126
IO6-106a Ru23 - 3	NIST610	0.083607938	0.001732383	0.683733748	0.047634319	12.13236033	0.286133109	0.059064294	0.0042695
IO6-106a Ru18 - 1	NIST610	0.073145372	0.001949117	0.581011907	0.024754783	13.67816446	0.308860309	0.057968777	0.002297735
IO6-106a Ru13 - 2	NIST610	0.075325614	0.002140774	0.604272299	0.025514033	13.24505169	0.291252078	0.0583475	0.002250473
IO6-106a Ru11 - 2	NIST610	0.073451094	0.001934227	0.590511976	0.02798255	13.64445103	0.29908389	0.058197624	0.002607481
IO6-106a Ru1 - 3	NIST610	0.075890061	0.002003798	0.617919355	0.028983323	13.03615324	0.307822805	0.058958716	0.002421514
IO6-106a Ru12 - 2	NIST610	0.071609002	0.001628121	0.576300143	0.022451231	13.98512292	0.287916729	0.058297442	0.002092177
IO6-106a Ru11 - 4	NIST610	0.073271053	0.001818944	0.592568867	0.02625605	13.64949603	0.318559834	0.05859309	0.002396661
IO6-106a Ru18 - 2	NIST610	0.068500941	0.001756684	0.546783582	0.025590613	14.59854067	0.384895255	0.05810244	0.002412764
IO6-106a Ru4 - 2	NIST610	0.072510526	0.001706811	0.588528389	0.020989774	13.81241043	0.326869229	0.058957525	0.001864409
IO6-106a Ru10 - 1	NIST610	0.072556199	0.001373674	0.59024543	0.026986935	13.81286874	0.283653227	0.05884029	0.002640393
IO6-106a Ru10 - 3	NIST610	0.071121036	0.001815921	0.576985495	0.025747745	14.09400427	0.338928787	0.058677209	0.00241844
IO6-106a Ru8 - 2	NIST610	0.072975006	0.001739016	0.595487932	0.023999511	13.74214726	0.302654675	0.059148819	0.002161218
IO6-106a Ru10 - 2	NIST610	0.071236196	0.001455745	0.581956789	0.024948472	14.07392889	0.314522968	0.059077611	0.002425046
IO6-106a Ru3 - 3	NIST610	0.076144381	0.002240259	0.6355662	0.060326738	13.05794671	0.307013484	0.060628957	0.005367423
IO6-106a Ru23 - 2	NIST610	0.073332444	0.001230775	0.609156972	0.025414595	13.62953189	0.291685177	0.059821304	0.002268425
IO6-106a Ru2 - 4	NIST610	0.074057385	0.001924894	0.621935422	0.029356294	13.36652981	0.297683239	0.060842579	0.002533808
IO6-106a Ru9 - 1	NIST610	0.071729373	0.001383083	0.601054145	0.033930705	13.9782509	0.296168369	0.060668234	0.003257085
IO6-106a Ru12 - 3	NIST610	0.072882977	0.001707671	0.614715057	0.02777409	13.73386672	0.31339057	0.061124064	0.00244943
IO6-106a Ru10 - 4	NIST610	0.066347796	0.001821236	0.550255065	0.027642942	15.100406	0.408689877	0.059962987	0.002846047
IO6-106a Ru23 - 1	NIST610	0.069062547	0.001564676	0.580720678	0.031999869	14.43309352	0.31735362	0.060568082	0.003244085
IO6-106a Ru17 - 1	NIST610	0.075330264	0.001901472	0.655952107	0.028416154	13.26234467	0.278605706	0.06352342	0.002436133
IO6-106a Ru12 - 5	NIST610	0.074065447	0.001717064	0.643434366	0.029349488	13.48527025	0.296471545	0.062894518	0.002470577
IO6-106a Ru2 - 3	NIST610	0.075176126	0.001803589	0.656454373	0.041213844	13.16884393	0.277631387	0.063270894	0.00382138
IO6-106a Ru16 - 2	NIST610	0.068935741	0.002059723	0.593246909	0.028538682	14.47473157	0.356673258	0.062707292	0.003106472
IO6-106a Ru22 - 1	NIST610	0.076474432	0.001751469	0.676579775	0.038153389	13.04859578	0.280914708	0.063825453	0.003520447
IO6-106a Ru21 - 3	NIST610	0.075547301	0.001969707	0.671266529	0.028806952	13.20781926	0.309225761	0.064109193	0.002464711
IO6-106a Ru16 - 1	NIST610	0.071862749	0.001962701	0.63898321	0.031170513	13.8932272	0.304515214	0.064794233	0.003093626
IO6-106a Ru8 - 1	NIST610	0.064423603	0.001816283	0.561351172	0.030580086	15.5549148	0.50480373	0.063177	0.00392395
IO6-106a Ru21 - 1	NIST610	0.073845334	0.00169659	0.664423293	0.033924619	13.50962323	0.308227254	0.065026103	0.003090975
IO6-106a Ru14 - 3	NIST610	0.080146325	0.002277095	0.737195102	0.031712972	12.47359741	0.296592234	0.067019658	0.002449972
IO6-106a Ru2 - 5	NIST610	0.07840648	0.002153836	0.729598369	0.042643001	12.64196974	0.287569494	0.067483598	0.003812686
IO6-106a Ru20 - 3	NIST610	0.071586478	0.002128306	0.665533837	0.041334045	14.14458005	0.411872263	0.067406355	0.003901589
IO6-106a Ru25 - 2	NIST610	0.464728692	0.059503206	16.64763799	0.822408014	2.173841084	0.402233053	0.257406512	0.012873209
IO6-106a Ru20 - 1	NIST610	0.077927383	0.001763752	0.763866149	0.055296994	12.9611475	0.293968821	0.071103934	0.005240907
IO6-106a Ru6 - 1	NIST610	0.073071243	0.002079937	0.714758467	0.057150968	13.70621005	0.316129144	0.071046366	0.005427189
IO6-106a Ru8 - 3	NIST610	0.080098744	0.001684622	0.817801905	0.031485339	12.51380899	0.279321654	0.07392768	0.002381078
IO6-106a Ru12 - 1	NIST610	0.074292384	0.001607929	0.757083512	0.043849702	13.48611607	0.273488531	0.073851667	0.003881291
IO6-106a Ru3 - 1	NIST610	0.078510673	0.004861098	0.824541904	0.112851955	12.62339846	0.361972383	0.076092054	0.009574399
IO6-106a Ru1 - 2	NIST610	0.078079705	0.002244458	0.819678335	0.048542453	12.67219609	0.306170335	0.07594847	0.004386204
IO6-106a Ru13 - 3	NIST610	0.07547916	0.001945312	0.793020722	0.048310267	13.22428742	0.284307051	0.076536745	0.004061609
IO6-106a Ru2 - 2	NIST610	0.081105343	0.002212793	0.877850912	0.052788388	12.19657532	0.262889278	0.07836788	0.004402321
IO6-106a Ru1 - 1	NIST610	0.075469438	0.00200656	0.805770741	0.080870941	13.11207738	0.29335839	0.077185501	0.007827981
IO6-106a Ru12 - 4	NIST610	0.073990438	0.001777788	0.786985701	0.04351699	13.51739316	0.296875267	0.077068245	0.004275073
IO6-106a Ru25 - 1	NIST610	0.081203472	0.001744466	0.887330334	0.132773097	12.34283115	0.289481958	0.078968679	0.013462436
IO6-106a Ru17 - 2	NIST610	0.086025155	0.002496461	0.959137174	0.048590882	11.7224909	0.272005237	0.081271498	0.003765411
IO6-106a Ru13 - 1	NIST610	0.07825132	0.002121518	0.86362295	0.065027718	12.74956964	0.290102669	0.080216561	0.005208951
IO6-106a Ru7 - 1	IO6-106a R	0.073317825	0.001493403	0.806607775	0.279333358	13.70820759	0.31329339	0.079665803	0.025536878
IO6-106a Ru19 - 1	NIST610	0.070581514	0.001746963	0.774174051	0.126389637	14.15974495	0.336808431	0.0797477	0.01135625
IO6-106a Ru2 - 1	NIST610	0.080416269	0.003049389	0.927369584	0.099203605	12.29871989	0.320488816	0.083484545	0.009124867
IO6-106a Ru3 - 2	NIST610	0.074939264	0.00200089	0.850113328	0.048760096	13.25451053	0.305587565	0.082272749	0.004159663
IO6-106a Ru7 - 2	IO6-106a R	0.080033967	0.001686654	0.983151181	0.051613287	12.68315819	0.291415926	0.089204737	0.004625612
IO6-106a Ru - 1	NIST610	0.075928207	0.00199412	0.937351418	0.076515737	13.05375937	0.298235519	0.089307145	0.007187666
IO6-106a Ru20 - 2	NIST610	0.085773453	0.001970155	1.115304597	0.04521244	11.63309913	0.259560167	0.094145165	0.003418334
IO6-106a Ru9 - 2	NIST610	0.075740081	0.001751938	0.947834435	0.053605539	13.23688332	0.303189977	0.09052384	0.004725922
IO6-106a Ru7 - 2	NIST610	0.085779909	0.002254879	1.145354013	0.06052238	11.69009924	0.321758382	0.096803379	0.00406588
IO6-106a Ru7 - 1	NIST610	0.074097724	0.001803621	0.949928796	0.195940439	13.52377577	0.3370461	0.093108848	0.01826203
IO6-106a Ru17 - 3	NIST610	0.082005537	0.002648378	1.213085313	0.074629389	12.24750126	0.358202283	0.107807119	0.005234674
IO6-106a Ru21 - 2	NIST610	0.080415135	0.001829752	1.279312244	0.107302243	12.41444738	0.267184577	0.114959144	0.009582413
IO6-106a Ru19 - 2	NIST610	0.080712454	0.002156784	1.298302449	0.148297684	12.39017723	0.290577166	0.116919632	0.011366143
IO6-106a Ru14 - 2	NIST610	0.088478891	0.002294882	1.767908569	0.087828217	11.28934031	0.250639828	0.145556748	0.006233796

Appendix B 5: U/Pb Results for the rutile assemblage in sample I06-106a maf

Analysis	206Pb/238U	207Pb/206Pb	207Pb/206Pb	207Pb/235U(calc)	207Pb/235U(calc)	208Pb/206Pb	208Pb/206Pb	208Pb/232Th	208Pb/232Th	238U/206Pb	238U/206Pb
IO6-106a Mo	0.001342355	0.057684835	0.00151583	0.698460446	0.017049365	3.286954985	0.064648927	0.026624045	0.000574294	11.41534536	0.186455882
IO6-106a Mo	0.001421256	0.058132298	0.001511352	0.691100497	0.017013073	3.668924515	0.053289559	0.02692707	0.000592508	11.6274034	0.208796422
IO6-106a Mo	0.001425397	0.057891825	0.001899635	0.707253484	0.021903133	3.778677853	0.107785994	0.027106183	0.000639079	11.29700303	0.187509672
IO6-106a Mo	0.001613544	0.058089283	0.001734386	0.691378284	0.019241361	3.45423175	0.130211032	0.026570779	0.000615544	11.59386122	0.219122587
IO6-106a Mo	0.001298202	0.057683255	0.001437732	0.68997821	0.016381473	3.195056889	0.111517356	0.027300755	0.00059367	11.57923692	0.18833184
IO6-106a Mo	0.001336039	0.057818622	0.001642341	0.69856205	0.019375508	2.365992372	0.037750661	0.026834036	0.00056754	11.4657818	0.185420661
IO6-106a Mo	0.001453439	0.058061705	0.001363958	0.699903365	0.016501096	4.022997879	0.147956083	0.025470321	0.000540307	11.4908645	0.203607072
IO6-106a Mo	0.00135576	0.05964218	0.001423524	0.707781782	0.016328488	5.012658714	0.382201894	0.026442599	0.000550849	11.67242673	0.197052579
IO6-106a Mo	0.001386274	0.056927016	0.001444318	0.681534486	0.016228295	2.25110507	0.033809724	0.026888109	0.000593696	11.57244742	0.19632508
IO6-106a Mo	0.001365475	0.058063639	0.001425653	0.692247097	0.015877817	3.174228765	0.172640311	0.025803158	0.000549097	11.62114763	0.191587949
IO6-106a Mo	0.001327193	0.058361504	0.001459304	0.699351351	0.015868054	2.078212396	0.06044608	0.027728711	0.000601534	11.55800116	0.188866385
IO6-106a Mo	0.001334421	0.058647853	0.001516436	0.701338736	0.017712956	2.334622467	0.029289506	0.026716388	0.000557211	11.57936683	0.189886339
IO6-106a Mo	0.001442126	0.057416082	0.00157019	0.695082373	0.017355996	2.425357221	0.082898979	0.026272813	0.000609859	11.43709275	0.199443497
IO6-106a Mo	0.001441251	0.057527525	0.001385361	0.688856859	0.015486577	2.045885754	0.028670342	0.026265254	0.000547574	11.56372585	0.198690085
IO6-106a Mo	0.001265719	0.058245393	0.001456347	0.701996678	0.017469695	2.980573808	0.100247785	0.02785712	0.000633003	11.48337693	0.183280534
IO6-106a Mo	0.001335921	0.058445382	0.001365835	0.703281971	0.015671478	5.900491463	0.426446852	0.026939357	0.000549047	11.50596603	0.188327419
IO6-106a Mo	0.001607621	0.059757178	0.002211641	0.72940994	0.026302043	3.801394479	0.154268679	0.027997436	0.000850406	11.2608231	0.208858182
IO6-106a Mo	0.001620862	0.058690346	0.001713648	0.704942126	0.021157813	3.344717465	0.094173129	0.027208779	0.000622125	11.47372591	0.222391579
IO6-106a Mo	0.001390846	0.058833734	0.00154288	0.711831635	0.017283493	5.108095618	0.349274108	0.02665068	0.00063605	11.40607414	0.193723722
IO6-106a Mo	0.001463015	0.058498243	0.001520305	0.698305329	0.016776377	4.592282307	0.086381555	0.026789234	0.00057437	11.57412384	0.21139924
IO6-106a Mo	0.001614194	0.059120543	0.001570356	0.703414374	0.017624738	4.242107007	0.129176239	0.02758881	0.000711001	11.61260526	0.228820123
IO6-106a Mo	0.001395944	0.059578064	0.001859041	0.696289463	0.019900696	3.627728602	0.058089136	0.026274587	0.000583326	11.83916001	0.212037922
IO6-106a Mo	0.001810131	0.059577571	0.002705683	0.716925922	0.035501615	3.889888452	0.200028444	0.026582434	0.000817217	11.46081756	0.241693646
IO6-106a Mo	0.001280986	0.05843785	0.001490844	0.693186955	0.016776337	4.078805965	0.074755131	0.026460049	0.000575239	11.68074376	0.186955257
IO6-106a Mo	0.001340838	0.058597428	0.001377874	0.702382748	0.015753195	8.086022051	0.452612468	0.02676327	0.000552277	11.54641517	0.188943797
IO6-106a Mo	0.001285179	0.05859209	0.001434835	0.692328571	0.016130062	6.013452597	0.378525389	0.026093979	0.000633556	11.71441021	0.187388575
IO6-106a Mo	0.001331013	0.058179391	0.001433845	0.6832541	0.016224404	5.598573831	0.278062789	0.02555977	0.000573945	11.78245604	0.199360673
IO6-106a Mo	0.001322575	0.057285141	0.001449977	0.686496363	0.016601496	3.271280343	0.074240306	0.027434488	0.00055729	11.54573744	0.186178254
IO6-106a Mo	0.001519321	0.056995242	0.001647524	0.677428015	0.018244346	3.117042225	0.048444131	0.026746596	0.000588256	11.63545677	0.220621139
IO6-106a Mo	0.001406137	0.058686861	0.001524869	0.703028512	0.017566139	3.661267694	0.063276032	0.026645052	0.000617483	11.55404435	0.195323992
IO6-106a Mo	0.00149903	0.057933242	0.001581301	0.691979097	0.017897659	3.723179685	0.056596682	0.026149993	0.00052926	11.59390347	0.207114147
IO6-106a Mo	0.001989035	0.056856119	0.002424677	0.687634253	0.023660004	4.344023386	0.10618074	0.026705577	0.000659248	11.40936092	0.248639199
IO6-106a Mo	0.001360474	0.058400129	0.001430587	0.706049023	0.015876231	5.486912535	0.389159202	0.02735861	0.00059978	11.45632103	0.190585459
IO6-106a Mo	0.001557725	0.05756729	0.001698619	0.698506653	0.020922961	4.364449129	0.247589077	0.027653035	0.000643859	11.38622517	0.220317132
IO6-106a Mo	0.00132998	0.058111419	0.001442647	0.703261716	0.01617539	9.710478695	0.81520743	0.027335565	0.000610648	11.44265195	0.188390117
IO6-106a Mo	0.001381687	0.057966245	0.00140966	0.689237588	0.015350734	2.792953175	0.069558685	0.027123919	0.000551706	11.65078826	0.196302564
IO6-106a Mo	0.001358323	0.057894198	0.001485532	0.69468645	0.016934464	6.847149737	0.471667983	0.026227345	0.00057998	11.54605969	0.193221787
IO6-106a Mo	0.001270969	0.0583066	0.001398995	0.695560145	0.01538132	3.518713774	0.19087148	0.02626404	0.000585851	11.6108737	0.183723792
IO6-106a Mo	0.001388787	0.057895936	0.001429458	0.696560245	0.016018925	6.408460472	0.881917129	0.025888797	0.000544834	11.51394333	0.195718741

Appendix B 6: U/Pb results for the monazite assemblage in sample I06-06a maf

Analysis	176Lu/177Hf	176Lu/177Hf	176Hf/177Hf	176Hf/177Hf
I06-83 D2 - 9	2.57179264	0.07301056	0.31742798	0.01770178
I06-83 D2 - 8	2.73452826	0.07579655	0.32141172	0.01936563
I06-83 D2 - 7	1.39458967	0.03843111	0.29526412	0.01754337
I06-83 D2 - 6	0.76614754	0.02219742	0.28737234	0.01560945
I06-83 D2 - 5	2.08544029	0.06067202	0.31305955	0.0173971
I06-83 D2 - 4	2.94388508	0.08100103	0.30525031	0.01688865
I06-83 D2 - 3	0.83701324	0.02222051	0.27753855	0.01473104
I06-83 D2 - 20	0.98779798	0.0300977	0.29594699	0.01590566
I06-83 D2 - 2	0.97918514	0.02592087	0.28735835	0.01423692
I06-83 D2 - 19	2.38050497	0.06282929	0.30670525	0.01907865
I06-83 D2 - 18	2.72034874	0.07465065	0.31307704	0.01709844
I06-83 D2 - 17	1.31222134	0.03515004	0.30017325	0.01506698
I06-83 D2 - 16	1.68872183	0.05253255	0.3016369	0.01505137
I06-83 D2 - 15	0.73143671	0.02022132	0.28734083	0.01501172
I06-83 D2 - 14	3.32275528	0.09049331	0.31834695	0.01806137
I06-83 D2 - 13	0.31700491	0.01981551	0.2853474	0.00960815
I06-83 D2 - 12	3.14837938	0.08812182	0.32223866	0.01705873
I06-83 D2 - 11	1.95832184	0.06226267	0.2851483	0.01533088
I06-83 D2 - 10	0.00850571	0.00103685	0.28164047	0.00190651
I06-83 D2 - 1	1.536624	0.06163364	0.28912344	0.01639606
I06-83 D1 - 9	2.65592993	0.08150024	0.31411237	0.01669058
I06-83 D1 - 8	4.24327316	0.12187233	0.33040765	0.01808903
I06-83 D1 - 7	4.25029362	0.12802161	0.33145301	0.02091445
I06-83 D1 - 6	3.44810647	0.08746587	0.32565812	0.01546383
I06-83 D1 - 5	3.18279771	0.08610732	0.30687237	0.01596122
I06-83 D1 - 4	3.58628838	0.09828354	0.32086877	0.01725286
I06-83 D1 - 31	2.83773417	0.06159761	0.31598278	0.01561606
I06-83 D1 - 30	2.5936548	0.06791441	0.30684675	0.01446147
I06-83 D1 - 3	2.90231892	0.07920223	0.31187693	0.01675543
I06-83 D1 - 29	2.1283373	0.09637981	0.29968676	0.01529814
I06-83 D1 - 28	3.45118236	0.08570515	0.33032782	0.01523223
I06-83 D1 - 27	3.1554487	0.08414835	0.31843954	0.01606753
I06-83 D1 - 26	3.06132653	0.07917534	0.32021832	0.01770805
I06-83 D1 - 25	1.5892238	0.04479684	0.30402136	0.01618208
I06-83 D1 - 24	1.8653419	0.05320758	0.30421341	0.01922478
I06-83 D1 - 23	2.21267221	0.06643854	0.31311537	0.01788419
I06-83 D1 - 22	2.66450438	0.06762032	0.3114791	0.01494063
I06-83 D1 - 21	1.58349476	0.04375402	0.28508429	0.01525616
I06-83 D1 - 20	1.77363727	0.08405893	0.30633431	0.01823032
I06-83 D1 - 2	2.66864548	0.06941735	0.30571396	0.01515935
I06-83 D1 - 19	2.15651711	0.06168396	0.29771617	0.02002668
I06-83 D1 - 18	1.69601256	0.42832139	0.28531918	0.14569622
I06-83 D1 - 17	3.35600582	0.48480429	0.3313606	0.0918144
I06-83 D1 - 16	4.11334879	0.09855829	0.34313334	0.01617737
I06-83 D1 - 15	5.20290318	0.11859291	0.34882725	0.0148425
I06-83 D1 - 14	2.88533569	0.07470287	0.29794882	0.01583694
I06-83 D1 - 13	6.58261426	0.16882756	0.33915455	0.01534729
I06-83 D1 - 12	3.56836357	0.09066415	0.30864891	0.01503954
I06-83 D1 - 11	3.43222414	0.09879568	0.33663191	0.01811681
I06-83 D1 - 10	4.01058257	0.11713655	0.34343533	0.02000345
I06-83 D1 - 1	2.73447161	0.07855901	0.32598721	0.02045171
I06-60 - 9	1.15120406	0.0326491	0.30260148	0.01729806
I06-60 - 80	1.36064516	0.03697637	0.27910444	0.01692238
I06-60 - 8	1.24494773	0.03619391	0.29482259	0.01778071
I06-60 - 79	1.326842	0.03661665	0.30464664	0.01677639
I06-60 - 78	1.46544929	0.04144231	0.28588101	0.01841898
I06-60 - 77	1.34489813	0.03769481	0.290141	0.01799245
I06-60 - 76	1.21147486	0.03269958	0.30286536	0.01522772
I06-60 - 75	1.19094929	0.03243028	0.29345561	0.01705451
I06-60 - 74	1.198711	0.03305093	0.30524998	0.01719609
I06-60 - 73	1.23460425	0.03371883	0.29490621	0.01518134
I06-60 - 72	1.47721299	0.04327273	0.29335868	0.01647858
I06-60 - 71	1.37307138	0.04176143	0.30406827	0.02067463
I06-60 - 70	1.3042174	0.0391179	0.28752462	0.01775046
I06-60 - 7	1.22177957	0.03537073	0.27975086	0.01566858
I06-60 - 69	1.308412	0.03593014	0.29835593	0.01542256
I06-60 - 68	1.41150115	0.04256918	0.28106303	0.01652812
I06-60 - 67	1.30073339	0.0362706	0.30592807	0.01590454
I06-60 - 66	1.25854491	0.03421851	0.30065473	0.01705156
I06-60 - 65	1.20146292	0.03193858	0.30233912	0.0149433
I06-60 - 64	1.17190266	0.03137877	0.30626196	0.01574578
I06-60 - 63	1.06163249	0.02776507	0.27426789	0.01588526
I06-60 - 62	1.10887228	0.02877439	0.28259423	0.01514442
I06-60 - 61	1.4400254	0.04083867	0.30751394	0.01692481
I06-60 - 60	1.47211889	0.04324997	0.31465277	0.01753015
I06-60 - 6	1.32765538	0.03970531	0.2906269	0.01669321
I06-60 - 59	1.39534683	0.0399111	0.30614379	0.01643638
I06-60 - 58	1.43506496	0.03904561	0.29460549	0.01538976
I06-60 - 57	1.46714926	0.04457829	0.30464122	0.01880595
I06-60 - 56	1.46528507	0.04343949	0.30661623	0.01850147
I06-60 - 55	1.47767949	0.04417126	0.30174044	0.01773857
I06-60 - 54	1.30250272	0.03664755	0.31378781	0.01757437
I06-60 - 53	1.29338442	0.036363	0.3013243	0.01683164
I06-60 - 52	1.16999444	0.0315386	0.28672381	0.01470045
I06-60 - 51	1.20905603	0.03305767	0.29898886	0.01600182
I06-60 - 50	1.12448465	0.03028432	0.30255846	0.01682807
I06-60 - 5	1.34050579	0.03939419	0.29368955	0.01805044
I06-60 - 49	1.1354607	0.03171049	0.28633388	0.01600235
I06-60 - 48	1.25572944	0.03572774	0.31077044	0.01717871
I06-60 - 47	1.29921463	0.03686052	0.2929006	0.01583555
I06-60 - 46	1.27284628	0.0361981	0.28960898	0.01573438
I06-60 - 45	1.2762937	0.03533868	0.29762647	0.01555493
I06-60 - 44	1.31866577	0.03890602	0.30339599	0.01868417
I06-60 - 43	1.42448254	0.04136948	0.30220924	0.01798494
I06-60 - 42	1.44196095	0.04421188	0.28902273	0.01920975
I06-60 - 41	1.54238023	0.0486271	0.30101551	0.01940669
I06-60 - 40	1.40349584	0.04264985	0.29638281	0.01719973
I06-60 - 4	1.29859492	0.03857256	0.29981455	0.01949492
I06-60 - 39	1.36518365	0.04379382	0.30517908	0.0212227
I06-60 - 38	1.31266995	0.04279069	0.29543031	0.01846494
I06-60 - 37	1.24403768	0.03507774	0.29221255	0.01669665
I06-60 - 36	1.22908853	0.03515829	0.29076862	0.01666868
I06-60 - 35	1.16611347	0.03204908	0.29258968	0.01632026
I06-60 - 34	1.25447803	0.03618981	0.29478949	0.01834782
I06-60 - 33	1.23540188	0.03605671	0.29905781	0.01647887
I06-60 - 32	1.18836374	0.03418797	0.2903685	0.01589215
I06-60 - 31	1.16609475	0.03379083	0.29942742	0.0162827
I06-60 - 30	1.22297493	0.03483434	0.29678391	0.01826603
I06-60 - 3	1.26977891	0.03781575	0.29505995	0.01669135
I06-60 - 29	1.32604103	0.03878149	0.31591596	0.01870142
I06-60 - 28	1.09556145	0.03015096	0.2898147	0.0156207
I06-60 - 27	1.25926753	0.03685659	0.30669941	0.01680981
I06-60 - 26	1.22613498	0.03668579	0.29638798	0.01737544
I06-60 - 25	1.11264631	0.0319319	0.28443367	0.01560848
I06-60 - 24	1.33746316	0.03932311	0.32131562	0.02078845
I06-60 - 23	1.33792397	0.03945347	0.30214226	0.01697824
I06-60 - 22	1.46977999	0.04557377	0.30458229	0.01913225
I06-60 - 21	1.31417331	0.03726327	0.30101635	0.01650516
I06-60 - 20	1.2819892	0.0367802	0.29723413	0.01615537

I06-60 - 2	1.23726414	0.03621733	0.29512726	0.01635292
I06-60 - 19	1.40519243	0.04227381	0.30508971	0.01735375
I06-60 - 18	1.55470325	0.04887629	0.30062479	0.02205567
I06-60 - 17	1.39804428	0.04337944	0.29802861	0.02017757
I06-60 - 16	1.25843657	0.03653524	0.29302593	0.01618551
I06-60 - 15	1.23791577	0.0359135	0.29320587	0.01719658
I06-60 - 14	1.21456417	0.0336756	0.2861044	0.01606276
I06-60 - 13	1.24851489	0.03622317	0.28197196	0.0157918
I06-60 - 12	1.20313403	0.03356621	0.29205535	0.01710245
I06-60 - 11	1.22395698	0.03447242	0.30365952	0.01600291
I06-60 - 10	1.26041652	0.03626298	0.28950719	0.01596491
I06-60 - 9	1.24750313	0.0373443	0.31323636	0.01802813
I06-57 D3 - 9	0.05630639	0.00285921	0.28846828	0.01754005
I06-57 D3 - 8	0.02843449	0.00181896	0.28602006	0.01488108
I06-57 D3 - 7	0.07532467	0.00307341	0.28101413	0.01495714
I06-57 D3 - 6	0.0514646	0.00221608	0.27563352	0.01247168
I06-57 D3 - 5	0.05310062	0.00247043	0.28144024	0.0135392
I06-57 D3 - 4	0.02410039	0.00129057	0.28528743	0.0117201
I06-57 D3 - 3	0.01976274	0.0012124	0.28895265	0.01456385
I06-57 D3 - 2C	0.04278862	0.0020894	0.28166975	0.01341122
I06-57 D3 - 2	0.0269834	0.00165554	0.2786517	0.01399446
I06-57 D3 - 19	0.05977259	0.00227426	0.28682572	0.01197819
I06-57 D3 - 18	0.06729963	0.00261558	0.28483168	0.01326591
I06-57 D3 - 17	0.08732635	0.00304826	0.29222845	0.01250239
I06-57 D3 - 16	0.10045099	0.00353007	0.28184021	0.01454446
I06-57 D3 - 15	0.12365323	0.0043396	0.27204901	0.01335621
I06-57 D3 - 14	0.06860472	0.00299715	0.27674109	0.01476264
I06-57 D3 - 13	0.06216267	0.00302813	0.2744612	0.01433373
I06-57 D3 - 12	0.07305305	0.00285349	0.27652809	0.01157895
I06-57 D3 - 11	0.04579968	0.0019037	0.28406673	0.01188951
I06-57 D3 - 1C	0.02453146	0.00157412	0.29057035	0.01435838
I06-57 D3 - 1	0.04219062	0.00223616	0.29079407	0.0148561
I06-57 D2 - 9	0.1019857	0.00446964	0.27872087	0.01807502
I06-57 D2 - 8	0.04633604	0.00240591	0.29124766	0.01576458
I06-57 D2 - 7	0.10398194	0.00449839	0.3005242	0.01678518
I06-57 D2 - 6	0.07681739	0.00357574	0.27504558	0.0155626
I06-57 D2 - 5	0.05800425	0.00289392	0.28755575	0.01739444
I06-57 D2 - 4	0.05235981	0.00251109	0.29628505	0.01440785
I06-57 D2 - 3	0.03331521	0.00134372	0.28026582	0.00994331
I06-57 D2 - 2	0.01976729	0.0009268	0.28573406	0.00954422
I06-57 D2 - 1C	0.02396664	0.00133696	0.27296448	0.01336355
I06-57 D2 - 1	0.08478328	0.00396042	0.2864811	0.01477144
I06-57 D1 - 9	0.09992665	0.00318137	0.28298877	0.0109688
I06-57 D1 - 8	0.21063631	0.00691154	0.27165824	0.01416821
I06-57 D1 - 7	0.37686088	0.01250174	0.2959199	0.01718143
I06-57 D1 - 6	0.62129536	0.01790769	0.28144964	0.01486561
I06-57 D1 - 5	0.34340415	0.00813638	0.27760943	0.0111216
I06-57 D1 - 4	0.32568845	0.00809538	0.27904366	0.01157973
I06-57 D1 - 3	0.32635071	0.00805763	0.29105033	0.0126061
I06-57 D1 - 2	0.20936511	0.0040186	0.28846432	0.00835763
I06-57 D1 - 16	0.34139045	0.00757951	0.28114017	0.01033416
I06-57 D1 - 15	0.15574465	0.00523912	0.272386	0.01361364
I06-57 D1 - 14	0.24582417	0.00750356	0.26665246	0.01380604
I06-57 D1 - 13	0.13485259	0.00368265	0.28184775	0.01186334
I06-57 D1 - 12	0.30542699	0.00762401	0.28178752	0.01238762
I06-57 D1 - 11	0.09417861	0.00264035	0.27701752	0.0098239
I06-57 D1 - 1C	0.06505505	0.00172751	0.28479951	0.00773409
I06-57 D1 - 1	0.4528405	0.01590428	0.29727302	0.02052257
I06-38 D2 - 9	1.67431996	0.04286698	0.29141642	0.01429275
I06-38 D2 - 8	1.2935778	0.03247851	0.30114864	0.01534937

I06-38 D2 - 7	1.29588473	0.0289034	0.29372698	0.01216136
I06-38 D2 - 6	1.68873472	0.0421772	0.32025751	0.01579198
I06-38 D2 - 5	0.90795353	0.02226835	0.28401901	0.01526299
I06-38 D2 - 4	0.83942221	0.02252552	0.27718093	0.01446828
I06-38 D2 - 3	1.50106027	0.04121048	0.30600165	0.01579227
I06-38 D2 - 2C	0.64024062	0.01281701	0.28111606	0.01063691
I06-38 D2 - 2	0.85672433	0.02563367	0.29426502	0.01911328
I06-38 D2 - 19	1.34813826	0.03046763	0.30206892	0.01258093
I06-38 D2 - 17	0.62088279	0.01314828	0.28829857	0.01110485
I06-38 D2 - 16	0.69889849	0.01663915	0.28792003	0.01236848
I06-38 D2 - 15	0.86751381	0.02403312	0.2850384	0.01688624
I06-38 D2 - 14	0.69668215	0.01565082	0.28559289	0.0127115
I06-38 D2 - 13	0.78126036	0.02104237	0.29971587	0.01465274
I06-38 D2 - 12	1.26166436	0.03988656	0.28976797	0.01760696
I06-38 D2 - 11	0.99488165	0.02820056	0.29597598	0.01718254
I06-38 D2 - 1C	1.71304733	0.05368018	0.28928423	0.0195808
I06-38 D2 - 1	0.83766409	0.0244484	0.29127879	0.01577504
I06-38 D1 - 9	1.99616519	0.04241573	0.29549039	0.01183026
I06-38 D1 - 8	2.14031931	0.04275455	0.30636674	0.01123654
I06-38 D1 - 7	2.21507445	0.04429571	0.307997	0.01130169
I06-38 D1 - 6	2.20319218	0.04815756	0.30317218	0.01332202
I06-38 D1 - 5	2.08632885	0.0444308	0.31021098	0.01239124
I06-38 D1 - 41	2.69237896	0.05819479	0.30437714	0.01235147
I06-38 D1 - 4C	4.46891614	0.12624021	0.33678317	0.01936616
I06-38 D1 - 4	2.00262109	0.04178824	0.30086225	0.01172365
I06-38 D1 - 39	4.32626908	0.1179203	0.30841919	0.01759572
I06-38 D1 - 38	2.8784783	0.06699	0.30206743	0.01370221
I06-38 D1 - 37	2.21076249	0.04665003	0.31679296	0.0122516
I06-38 D1 - 36	1.35135284	0.03138461	0.2845797	0.01538342
I06-38 D1 - 35	1.28403924	0.03168696	0.31222045	0.01316784
I06-38 D1 - 34	1.59478818	0.03722221	0.29088307	0.01285416
I06-38 D1 - 33	1.65317541	0.05072703	0.31280777	0.01448284
I06-38 D1 - 32	1.66908162	0.04345542	0.28737586	0.01727513
I06-38 D1 - 31	2.54286004	0.05822791	0.30635208	0.01363273
I06-38 D1 - 3C	3.37935036	0.08210069	0.32598011	0.01609898
I06-38 D1 - 3	1.81408769	0.04003872	0.29886654	0.01496752
I06-38 D1 - 29	2.25012761	0.04745818	0.3080538	0.01203797
I06-38 D1 - 28	1.77892749	0.03368997	0.29821023	0.01032425
I06-38 D1 - 27	2.5721727	0.05822823	0.31261283	0.01418592
I06-38 D1 - 26	2.3244931	0.04767157	0.31282279	0.01178324
I06-38 D1 - 25	1.69959943	0.03667844	0.2993887	0.01254788
I06-38 D1 - 24	1.45578821	0.02838789	0.29739904	0.01057396
I06-38 D1 - 23	1.89307164	0.04354195	0.31094257	0.01384567
I06-38 D1 - 22	1.6997034	0.04107761	0.29867696	0.01456445
I06-38 D1 - 21	1.77459472	0.03972762	0.29824354	0.01495236
I06-38 D1 - 2C	1.90837992	0.0397635	0.30171575	0.01243622
I06-38 D1 - 2	1.83854595	0.03926161	0.31124487	0.01288451
I06-38 D1 - 19	2.04014778	0.04322665	0.30832093	0.01207092
I06-38 D1 - 18	2.3055134	0.04855462	0.30764389	0.01435743
I06-38 D1 - 17	2.42038527	0.05401573	0.29953399	0.01330836
I06-38 D1 - 16	1.98611076	0.03844064	0.30602468	0.01137879
I06-38 D1 - 15	1.96228849	0.03903784	0.29954361	0.01278236
I06-38 D1 - 14	1.79167873	0.03873171	0.30003877	0.01246776
I06-38 D1 - 13	1.94307227	0.04396965	0.30541786	0.01308692
I06-38 D1 - 12	2.39477417	0.05176173	0.31021616	0.01246486
I06-38 D1 - 11	2.25817923	0.04590024	0.3032456	0.01232054
I06-38 D1 - 1C	2.02271714	0.04144835	0.30104067	0.01326569
I06-38 D1 - 1	2.14688485	0.04758136	0.30690764	0.0134043
I06-106a m D	2.00212846	0.12401095	0.28802261	0.03650135
I06-106a m D	0.04895528	0.00398318	0.26781313	0.02359032

I06-106a m D	0.05177678	0.00410509	0.27733168	0.02328723
I06-106a m D	2.17893504	0.14289045	0.27611336	0.03897157
I06-106a m D	0.09527337	0.00601349	0.29008831	0.02879504
I06-106a m D	0.07880186	0.00597812	0.2726646	0.0255759
I06-106a m D	3.34028881	0.27915255	0.3439737	0.05488502
I06-106a m D	0.15025945	0.00892799	0.27784353	0.02436043
I06-106a m D	0.19851007	0.01114392	0.30768502	0.03009133
I06-106a m D	0.22400587	0.01299899	0.30465013	0.02700944
I06-106a m D	0.13123609	0.00845323	0.28851478	0.02434694
I06-106a m D	0.17319874	0.00769586	0.28819405	0.01915702
I06-106a m D	0.24301464	0.01405162	0.29366079	0.02736105
I06-106a m D	0.18432283	0.00950491	0.28929874	0.02109483
I06-106a m D	1.53708251	0.09324228	0.28810339	0.03829645
I06-106a m D	0.09687309	0.00649971	0.29611067	0.02874173
I06-106a m D	0.4835303	0.01927072	0.28864472	0.02084454
I06-106a m D	0.63997628	0.03742761	0.27787052	0.02996109
I06-106a m D	0.70240137	0.06967056	0.2583888	0.06271255
I06-106a m D	0.76868818	0.05480142	0.2824682	0.03959833
I06-106a m D	0.52941948	0.02974969	0.29720158	0.03014785
I06-106a m D	4.12372337	0.26815361	0.31528359	0.0408351
I06-106a m D	2.46112563	0.21334866	0.3251558	0.06047306
I06-106a m D	0.14021711	0.01114275	0.29058784	0.02810943
I06-106a m D	0.20453309	0.01087931	0.27265555	0.02317248
I06-106a m D	0.35728484	0.01879531	0.27973375	0.0257514
I06-106a m D	1.44980486	0.13470348	0.2944786	0.06801534
I06-106a m D	1.40912009	0.11287693	0.2726778	0.04414532
I06-106a m D	0.41523253	0.02264803	0.26416473	0.02987677
I06-106a m D	0.174197	0.00973288	0.27632379	0.02365236
I06-106a m D	0.19454344	0.01186423	0.26320611	0.02458626
I06-106a m D	0.14343066	0.00899287	0.27014347	0.03253142
I06-106a m D	3.48171282	0.22458863	0.35148448	0.04298687
I06-106a m D	0.23043183	0.01471299	0.26799794	0.03456469
I06-106a m D	2.39168841	0.26766326	0.30789993	0.05600865
I06-106a m D	4.44241983	0.32626629	0.36559309	0.05038988
I06-106a m D	0.08845491	0.00550172	0.29820026	0.02399123
I06-106a m D	0.98367172	0.0500546	0.27373823	0.02830217
I06-106a m D	1.8578722	0.10117181	0.31254383	0.03867437
I06-106a m D	1.79386934	0.10843439	0.28102897	0.03432765
I06-106a m D	1.85857794	0.1095892	0.28696691	0.03387735
I06-106a m D	1.36720458	0.07900681	0.3276847	0.03757121
I06-106a m D	1.97431978	0.11794821	0.28498945	0.03768049
I06-106a m D	2.28510952	0.24312573	0.36655393	0.07281682
I06-106a m D	0.17237197	0.01158627	0.29847139	0.0294518
I06-106a m D	0.15639763	0.00808229	0.27609002	0.02315048
I06-106a m D	0.14163161	0.00592187	0.28613293	0.01704722
I06-106a m D	0.31850777	0.01189702	0.28533957	0.01800363
I06-106a m D	0.34563611	0.01328076	0.27654722	0.01841705
I06-106a m D	1.80535086	0.09801628	0.30166047	0.03462267
I06-106a m D	0.10194266	0.00619557	0.27876359	0.02240099
I06-106a m D	0.40724094	0.02091338	0.28643531	0.02364238
I06-106a m D	0.00169621	0.00015603	0.28207993	0.00489734
I06-106a m D	0.06033361	0.00464135	0.29160019	0.02811672
I06-106a m D	1.14623055	0.05127417	0.28612683	0.02671573
I06-106a m D	1.40695167	0.06305262	0.29603055	0.02578057
I06-106a m D	0.46004526	0.02223864	0.31207443	0.03096322
I06-106a m D	0.34335121	0.02057034	0.27790742	0.03356899
I06-106a m D	0.12584772	0.00781082	0.26510188	0.02662352
I06-106a m D	0.23444615	0.01439665	0.29249638	0.02830867
I06-106a m D	3.8972545	0.27179026	0.35537679	0.04318808
I06-106a m D	0.04837066	0.00342085	0.27804485	0.0201822

I06-106a m D	0.04142607	0.00313051	0.2746355	0.02612718
I06-106a m D	0.05323413	0.00441072	0.29219448	0.02692349
I06-106a m D	0.64463659	0.0335577	0.28169003	0.02752423
I06-106a m D	1.90719283	0.13186862	0.31574245	0.0492282
I06-106a m D1 - 25				
I06-106a m D	0.11940923	0.00758155	0.28255679	0.02565766
I06-106a m D	0.132892	0.00785157	0.28807073	0.02722508
I06-106a m D	0.0787778	0.00516853	0.2751005	0.02401898
I06-106a m D	0.14254426	0.00830721	0.2633975	0.02280959
I06-106a m D	0.09832399	0.00709662	0.2818485	0.02373881
I06-106a m D	0.9257927	0.08066065	0.2831645	0.04822342
I06-106a m D1 - 2				
I06-106a m D	0.16866173	0.01029494	0.29725858	0.0298748
I06-106a m D	0.42802096	0.02138536	0.27405849	0.02480629
I06-106a m D	2.61117778	0.15720275	0.25525128	0.03141315
I06-106a m D	6.03051348	0.5016084	0.36502418	0.05737983
I06-106a m D	6.25738869	1.05138192	0.41287612	0.15217846
I06-106a m D	1.484921	0.10132858	0.30005932	0.04000445
I06-106a m D	1.69319527	0.10067804	0.31260225	0.04634752
I06-106a m D	2.26065886	0.21289093	0.30668944	0.05736745
I06-106a m D	2.20984967	0.20852162	0.30508495	0.07608638
I06-106a m D	1.83801041	0.10976326	0.3038644	0.03531002
I06-106a m D	2.50475577	0.20053897	0.30286639	0.05069875
I06-106a m D	1.62077186	0.13307652	0.24742447	0.04300284
I06-106a m D1 - 10				
I06-106a m D	1.53034635	0.11068566	0.29123267	0.04143318
I06-106a m D1 - 1				
I06-106a D3 -	0.23497327	0.01568012	0.29136505	0.03951576
I06-106a D3 -	0.03160236	0.0030912	0.29245585	0.0243529
I06-106a D3 -	0.05106493	0.01192345	0.26649388	0.06284992
I06-106a D3 -	0.03854684	0.0087092	0.24737529	0.06300076
I06-106a D3 -	0.0466111	0.00983011	0.29211943	0.06150894
I06-106a D3 -	0.02964751	0.00353247	0.27828202	0.02724174
I06-106a D3 -	0.75540513	0.03638406	0.28568208	0.03042536
I06-106a D3 -	0.02928732	0.00283897	0.29022111	0.02465233
I06-106a D3 -	0.2577625	0.01668878	0.30517218	0.03059938
I06-106a D3 -	0.10491022	0.0105727	0.25832898	0.02952178
I06-106a D3 -	0.0963647	0.00752781	0.26927901	0.0282238
I06-106a D3 -	0.03162694	0.00324077	0.30003826	0.02994169
I06-106a D3 -	0.20414055	0.02168812	0.29005906	0.05512469
I06-106a D3 -	0.15320768	0.01740859	0.26523433	0.04998872
I06-106a D3 -	0.11074252	0.00957922	0.30656931	0.03963935
I06-106a D3 -	0.16175823	0.02005587	0.28265049	0.0616907
I06-106a D3 - 27				
I06-106a D3 -	0.11239065	0.00950309	0.30009654	0.03585561
I06-106a D3 -	0.24605149	0.01598212	0.28452445	0.03181521
I06-106a D3 -	0.79696425	0.04217076	0.27932931	0.02900315
I06-106a D3 -	2.39887803	0.11287464	0.32403194	0.02949684
I06-106a D3 -	0.90126847	0.03310761	0.2956606	0.02040086
I06-106a D3 -	0.80082028	0.03607155	0.29015775	0.024655
I06-106a D3 -	0.96801661	0.05258695	0.29576166	0.02785721
I06-106a D3 -	0.23806366	0.01694237	0.27937474	0.03729671
I06-106a D3 -	0.86725234	0.03831695	0.30966622	0.02862977
I06-106a D3 -	1.00631852	0.04160227	0.31507525	0.02416556
I06-106a D3 -	1.64934659	0.05625635	0.30331752	0.02057418
I06-106a D3 -	2.1880509	0.08281845	0.29339236	0.02322588
I06-106a D3 -	1.72591498	0.05214816	0.28548308	0.01674129
I06-106a D3 -	2.08499141	0.09825041	0.29186675	0.02733752
I06-106a D3 -	0.1550228	0.0093628	0.2830151	0.029628
I06-106a D3 -	0.38785436	0.02059859	0.28941413	0.03164728

I06-106a D3 -	0.19991324	0.01216882	0.27072189	0.02987424
I06-106a D3 -	0.12992927	0.00893899	0.26265583	0.02711545
I06-106a D3 -	0.11426775	0.01089465	0.29234566	0.03133009
I06-106a D2 -	0.2174163	0.01679722	0.28114958	0.03505985
I06-106a D2 -	0.09728961	0.00748403	0.24658461	0.02592078
I06-106a D2 -	1.21244397	0.0716303	0.33478957	0.03666071
I06-106a D2 -	2.10788875	0.1248849	0.31168736	0.03879483
I06-106a D2 -	0.51415544	0.064952	0.30399494	0.06227973
I06-106a D2 -	0.73439446	0.0746522	0.29322061	0.06028495
I06-106a D2 -	0.77742771	0.0784643	0.31969891	0.06374403
I06-106a D2 -	0.09869358	0.00860611	0.29649557	0.03336808
I06-106a D2 -	0.072803	0.00617729	0.29450504	0.03049033
I06-106a D2 -	0.16370466	0.01232032	0.26342628	0.03918228
I06-106a D2 - 16				
I06-106a D2 -	0.17310299	0.01871229	0.27332342	0.04533474
I06-106a D2 -	0.09433218	0.00719362	0.28975486	0.03360025
I06-106a D2 -	0.03714436	0.00373343	0.28853738	0.0230828
I06-106a D2 - 13				
I06-106a D2 -	0.07827929	0.00745989	0.28936003	0.03159569
I06-106a D2 -	0.22873856	0.01506008	0.30304665	0.03771284
I06-106a D2 -	0.09422046	0.00742045	0.27681509	0.02526902
I06-106a D2 -	0.07061009	0.00655344	0.27004831	0.02975935
I06-106a D1 -	1.0361502	0.05959348	0.32813545	0.03635091
I06-106a D1 -	0.9133884	0.06438867	0.29275894	0.0293418
I06-106a D1 -	0.83298407	0.05366257	0.30327123	0.03163915
I06-106a D1 -	1.01219248	0.05714138	0.28902647	0.03792502
I06-106a D1 -	0.81690879	0.04820087	0.28797837	0.02832808
I06-106a D1 -	0.98509473	0.0553773	0.27509934	0.02833379
I06-106a D1 -	0.81717965	0.04329214	0.2947466	0.0294808
I06-106a D1 -	0.50345323	0.02745001	0.29296877	0.03197038
I06-106a D1 -	0.90316845	0.05653874	0.2823278	0.03561055
I06-106a D1 -	0.19580292	0.02642751	0.28640669	0.02064996
I06-106a D1 -	0.12261534	0.00713285	0.28360007	0.01187295
I06-106a D1 -	0.10973219	0.00577407	0.28849293	0.01627284
I06-106a D1 -	0.87758343	0.04670841	0.26361188	0.02777582
I06-106a D1 -	0.23559426	0.01565988	0.30148584	0.03185668
I06-106a D1 -	3.36303775	0.19940218	0.33443156	0.04246321
I06-106a D1 -	3.93879614	0.21873438	0.32044121	0.03489876
I06-106a D1 -	0.88518366	0.05748713	0.2690702	0.02290128
I06-106a D1 -	6.34808298	0.40626265	0.33959048	0.0401805
I06-106a D1 -	3.7293189	0.21589082	0.33601817	0.03740183
I06-106a D1 -	1.71706012	0.14614931	0.29617595	0.02924273
I06-106a D1 -	0.21976399	0.01344325	0.2985765	0.02789105
I06-106a D1 -	0.32934831	0.01825723	0.33077017	0.02975288
I06-106a D1 -	3.82315089	0.29079905	0.29874944	0.04500466
I06-08 D3 - 9	1.66444151	0.04215046	0.30409977	0.01296418
I06-08 D3 - 8	1.173024	0.02581539	0.29039304	0.01250265
I06-08 D3 - 7	5.01659468	0.1231472	0.32044024	0.01531949
I06-08 D3 - 6	3.55500083	0.07984891	0.32292969	0.0137782
I06-08 D3 - 5	2.28540852	0.05016076	0.29738365	0.01236313
I06-08 D3 - 4	3.72543008	0.08734742	0.31810125	0.01444029
I06-08 D3 - 3	2.41904055	0.05600911	0.30005025	0.01446527
I06-08 D3 - 20	2.13361721	0.04664011	0.3066466	0.01251851
I06-08 D3 - 2	1.24288661	0.02849972	0.28753513	0.01238635
I06-08 D3 - 19	2.77205246	0.05738182	0.29804173	0.01164299
I06-08 D3 - 18	1.45777942	0.03087034	0.29178843	0.01152312
I06-08 D3 - 17	1.14492569	0.02468725	0.30031566	0.01282205
I06-08 D3 - 16	2.52701922	0.05333751	0.30583611	0.01332805
I06-08 D3 - 15	2.91946228	0.06272582	0.31354861	0.01262506
I06-08 D3 - 14	3.06802694	0.06869132	0.31918967	0.0144334

I06-08 D3 - 13	3.23056432	0.06703836	0.32182364	0.01333996
I06-08 D3 - 12	1.62977545	0.03697427	0.29517145	0.01182821
I06-08 D3 - 11	1.43295205	0.03056426	0.29370514	0.01166558
I06-08 D3 - 10	1.72844516	0.03831085	0.31108322	0.01548918
I06-08 D3 - 1	1.14618674	0.02665599	0.28959167	0.01265431
I06-08 D2 - 9	0.96648867	0.02490092	0.28520449	0.01380978
I06-08 D2 - 8	1.0696681	0.03033858	0.29057145	0.01585018
I06-08 D2 - 7	1.01672237	0.02966823	0.30098575	0.01636965
I06-08 D2 - 6	10.6483489	0.26409051	0.38562313	0.01704876
I06-08 D2 - 5	6.28440506	0.15589955	0.35893846	0.01628156
I06-08 D2 - 4	3.76324458	0.0776939	0.3279913	0.01242612
I06-08 D2 - 3	16.0638802	0.35485311	0.46165203	0.01896284
I06-08 D2 - 25	0.8870064	0.02020511	0.28766737	0.01204825
I06-08 D2 - 24	0.9021759	0.02116919	0.30143923	0.01382546
I06-08 D2 - 23	0.85948949	0.01959247	0.29872502	0.01436516
I06-08 D2 - 22	1.00423909	0.02335441	0.28794109	0.01245492
I06-08 D2 - 21	1.01618727	0.02298329	0.29217057	0.01239943
I06-08 D2 - 20	0.84156568	0.02002116	0.29441849	0.01294679
I06-08 D2 - 2	9.52751687	0.21021779	0.37775797	0.01557194
I06-08 D2 - 19	0.85400953	0.01995672	0.28079436	0.01216344
I06-08 D2 - 18	0.85009485	0.02016549	0.29526345	0.01370961
I06-08 D2 - 17	0.9266705	0.02282607	0.29803414	0.01345377
I06-08 D2 - 16	0.80436812	0.01862445	0.28790048	0.01217468
I06-08 D2 - 15	1.35996676	0.03683749	0.30529005	0.01718542
I06-08 D2 - 14	0.88908906	0.02010153	0.27713536	0.01201474
I06-08 D2 - 13	0.90429926	0.02229784	0.2841657	0.01577578
I06-08 D2 - 12	1.06275157	0.02994044	0.30825315	0.01857212
I06-08 D2 - 11	0.87648936	0.02256577	0.28296049	0.01363802
I06-08 D2 - 10	1.18707524	0.03553241	0.29787493	0.0168826
I06-08 D2 - 1	11.3616267	0.23812732	0.40366003	0.01630888
I06-08 D1 - 9	5.00474789	0.11077424	0.33653042	0.01461223
I06-08 D1 - 8	2.15651021	0.05228077	0.30588529	0.01670576
I06-08 D1 - 7	9.4566094	0.20032741	0.37808427	0.0140789
I06-08 D1 - 6	10.1681366	0.21574124	0.4031573	0.0147099
I06-08 D1 - 5	3.14575447	0.06921044	0.31576374	0.01353097
I06-08 D1 - 4	13.6089323	0.31889529	0.43769625	0.01775316
I06-08 D1 - 3	9.86352745	0.23313876	0.37687367	0.01693453
I06-08 D1 - 20	3.08488909	0.06385304	0.31221827	0.01288182
I06-08 D1 - 2	5.49355184	0.14297042	0.35593767	0.0176748
I06-08 D1 - 19	4.56315611	0.101934	0.34658431	0.01666652
I06-08 D1 - 18	1.50369136	0.0346657	0.29745424	0.01287576
I06-08 D1 - 17	1.56266627	0.03491415	0.30431911	0.01279518
I06-08 D1 - 16	2.73170662	0.06058243	0.30886701	0.01288171
I06-08 D1 - 15	5.70940599	0.11911906	0.34320379	0.01343995
I06-08 D1 - 14	1.86714899	0.0421554	0.29668941	0.01282849
I06-08 D1 - 13	9.25259883	0.22130695	0.38980514	0.01650422
I06-08 D1 - 12	7.21355183	0.20650307	0.33620678	0.0203595
I06-08 D1 - 11	15.3083756	0.35461739	0.45953949	0.01905333
I06-08 D1 - 10	2.77440499	0.0662263	0.31954986	0.01429112
I06-08 D1 - 1	2.68958747	0.06378468	0.30414582	0.01369543
I06-05 R - 9	1.31357135	0.0292434	0.29811744	0.01302096
I06-05 R - 8	1.15897765	0.02918656	0.30475293	0.01253561
I06-05 R - 7	1.09295031	0.02602931	0.28996569	0.01189833
I06-05 R - 6	0.97828358	0.02158161	0.29437059	0.01180917
I06-05 R - 5	1.03951755	0.023274	0.29255178	0.01201074
I06-05 R - 40	0.99934569	0.0230882	0.29502268	0.01250642
I06-05 R - 4	1.01903556	0.0235028	0.28767704	0.01229594
I06-05 R - 39	1.33080014	0.03095648	0.29523479	0.01281708
I06-05 R - 38	1.21975529	0.02815299	0.2893486	0.01250815
I06-05 R - 37	1.11277079	0.02500861	0.28728026	0.01230041

I06-05 R - 36	1.03001415	0.02324489	0.28887266	0.01415602
I06-05 R - 35	1.10565984	0.02541874	0.2973914	0.01427492
I06-05 R - 34	1.10610004	0.02603521	0.29686167	0.01289546
I06-05 R - 33	0.96510933	0.022345	0.29069648	0.0127034
I06-05 R - 32	0.97122514	0.02283302	0.30203194	0.01643044
I06-05 R - 31	1.07559095	0.02489791	0.28729213	0.01330647
I06-05 R - 30	1.01220748	0.02196298	0.30923555	0.01498641
I06-05 R - 3	1.08693443	0.02473759	0.31006892	0.0147077
I06-05 R - 29	1.03608204	0.02267266	0.29713787	0.01184926
I06-05 R - 28	0.99951623	0.02196051	0.29220596	0.01174951
I06-05 R - 27	0.9611301	0.02131738	0.29831508	0.01226539
I06-05 R - 26	1.21243997	0.02883941	0.31175234	0.01735215
I06-05 R - 25	1.41964265	0.03406903	0.29186211	0.01322973
I06-05 R - 24	1.21863642	0.02764518	0.28579995	0.01314841
I06-05 R - 23	1.29474024	0.03117037	0.30350284	0.01634811
I06-05 R - 22	1.07506456	0.02490795	0.30556527	0.01413955
I06-05 R - 21	1.04144052	0.02394835	0.30296059	0.01323026
I06-05 R - 20	1.04879287	0.02536539	0.30286862	0.0140687
I06-05 R - 2	0.93187813	0.02093061	0.29352736	0.01307531
I06-05 R - 19	0.97804372	0.02132732	0.29245383	0.01291862
I06-05 R - 18	1.02089148	0.02302772	0.29486431	0.01216655
I06-05 R - 17	1.35184737	0.02923817	0.30939714	0.01213964
I06-05 R - 16	1.14335038	0.0248365	0.29236064	0.0119896
I06-05 R - 15	0.93857501	0.02113222	0.30568424	0.01324639
I06-05 R - 14	1.12312383	0.02455728	0.29195359	0.01173142
I06-05 R - 13	1.09590986	0.02498058	0.29030339	0.01329342
I06-05 R - 12	1.18211038	0.02786378	0.3008714	0.01550707
I06-05 R - 11	1.10409085	0.02477747	0.30784903	0.01490311
I06-05 R - 10	1.3179924	0.02998289	0.3052459	0.0127206
I06-05 R - 1	0.81561785	0.01862591	0.29026376	0.01414873
I06-05 O - 9	0.97338426	0.02353227	0.29610002	0.01315954
I06-05 O - 8	0.7799676	0.01722299	0.28974478	0.01191186
I06-05 O - 7	0.6978229	0.01589309	0.28699033	0.01175631
I06-05 O - 6	0.77403576	0.01654585	0.29186372	0.01168615
I06-05 O - 5	0.98201648	0.02223199	0.29806201	0.01258501
I06-05 O - 4	0.98288843	0.0223592	0.29969557	0.01239206
I06-05 O - 3	0.83853672	0.01858851	0.30732515	0.01208604
I06-05 O - 2	1.00239614	0.02278668	0.28542158	0.01387549
I06-05 O - 17	1.03180295	0.02366424	0.27730973	0.0133357
I06-05 O - 16	0.97027605	0.02153126	0.28694031	0.01171506
I06-05 O - 15	0.89429008	0.02005294	0.28568168	0.01187421
I06-05 O - 14	0.83347299	0.01893909	0.29987899	0.01231892
I06-05 O - 13	0.84624863	0.02067991	0.28268811	0.01280521
I06-05 O - 12	0.87681396	0.01993902	0.28907297	0.01200979
I06-05 O - 11	0.94834785	0.0229819	0.29744035	0.01328197
I06-05 O - 10	0.89292442	0.02141682	0.28023823	0.01366635
I06-05 O - 1	1.04672149	0.02446781	0.29560285	0.01276943
I06-05 C - 9	0.98179479	0.01876773	0.31623721	0.01047313
I06-05 C - 8	1.09741437	0.07675294	0.28357248	0.02975737
I06-05 C - 8	0.94603191	0.11023778	0.29738036	0.0360789
I06-05 C - 7	1.24472208	0.02531349	0.30526255	0.01117885
I06-05 C - 6	1.25253849	0.02610602	0.30446079	0.01147916
I06-05 C - 5	1.15594559	0.02315743	0.31504663	0.01180787
I06-05 C - 40	1.08267488	0.02128725	0.30452564	0.01062642
I06-05 C - 4	0.93414424	0.0177807	0.31282245	0.01197503
I06-05 C - 39	0.94473343	0.01774107	0.31517897	0.01073837
I06-05 C - 38	1.23306404	0.02549018	0.3060163	0.01195073
I06-05 C - 37	1.13669095	0.02284465	0.30645186	0.01117131
I06-05 C - 36	0.99002537	0.03228282	0.3082135	0.01088359
I06-05 C - 35	1.09251717	0.02184896	0.31612989	0.01216918

I06-05 C - 34	1.02765014	0.02003288	0.30794455	0.01055307
I06-05 C - 33	1.05283123	0.02041886	0.30707998	0.01129804
I06-05 C - 32	0.97554909	0.01855514	0.30952342	0.01024586
I06-05 C - 31	1.35416258	0.02900215	0.31377134	0.01209997
I06-05 C - 30	0.97398716	0.02647439	0.31547702	0.01145277
I06-05 C - 3	1.15688328	0.02562392	0.30711247	0.01221985
I06-05 C - 29	1.36762531	0.04503413	0.3165697	0.02117544
I06-05 C - 29	0.94068841	0.07900572	0.29492274	0.03258194
I06-05 C - 28	0.99595216	0.01971484	0.31404522	0.0116832
I06-05 C - 27	1.09859482	0.02294459	0.30800742	0.01270519
I06-05 C - 26	1.3274949	0.06882862	0.30681045	0.01202045
I06-05 C - 25	1.24406802	0.02560803	0.31394833	0.01267862
I06-05 C - 24	1.52846317	0.03483607	0.31701481	0.01368783
I06-05 C - 23	1.06707843	0.02046495	0.31341302	0.01051349
I06-05 C - 22	1.0759168	0.02049793	0.31413921	0.01045153
I06-05 C - 21	1.45591245	0.03307045	0.30056338	0.01552203
I06-05 C - 20	1.10374946	0.02044482	0.31932917	0.01022523
I06-05 C - 2	0.94911028	0.01846589	0.30518291	0.01179912
I06-05 C - 19	1.19833923	0.02376211	0.31083106	0.01104904
I06-05 C - 18	1.24572714	0.02654906	0.30684457	0.01183677
I06-05 C - 17	1.26066128	0.026778	0.29795117	0.0115819
I06-05 C - 16	1.21502467	0.02423445	0.31798724	0.01218138
I06-05 C - 15	1.05684399	0.01957342	0.32155415	0.01085075
I06-05 C - 14	1.1146427	0.0211514	0.31550887	0.0108916
I06-05 C - 13	1.17502917	0.02422233	0.30839345	0.01368994
I06-05 C - 12	1.08081009	0.02043406	0.3170384	0.01042672
I06-05 C - 11	1.10038375	0.02137572	0.31700781	0.01077121
I06-05 C - 10	1.01377819	0.01926926	0.31036357	0.01029889
I06-05 C - 1	0.97819877	0.02008518	0.31058021	0.0112656
I06-02a T2 - 9	0.98478164	0.01900208	0.30519869	0.01089959
I06-02a T2 - 8	1.11354624	0.02128496	0.30515875	0.01186184
I06-02a T2 - 7	1.23757122	0.02206534	0.30355011	0.00983233
I06-02a T2 - 6	1.9899866	0.038549	0.35352016	0.01320389
I06-02a T2 - 5	1.40529178	0.02693664	0.32727004	0.01209975
I06-02a T2 - 4	1.32202781	0.02574658	0.31752481	0.01044721
I06-02a T2 - 3	1.22152381	0.02193596	0.30889775	0.01026479
I06-02a T2 - 2	1.02775199	0.01803105	0.30935643	0.00922394
I06-02a T2 - 1	1.03024092	0.01812402	0.29938933	0.00997082
I06-02a T1 - 9	1.36440268	0.02663501	0.32752096	0.01116971
I06-02a T1 - 8	1.37778785	0.02838422	0.33079582	0.01176168
I06-02a T1 - 7	1.20377644	0.02268638	0.33074482	0.01158258
I06-02a T1 - 6	1.30453875	0.02617283	0.32943263	0.0120634
I06-02a T1 - 5	1.5184623	0.03102897	0.3348033	0.01202826
I06-02a T1 - 4	1.44223074	0.02811681	0.32573214	0.01204932
I06-02a T1 - 3	1.12871993	0.0195863	0.30394871	0.00944177
I06-02a T1 - 2	1.11262886	0.01962674	0.3132216	0.00950286
I06-02a T1 - 1	1.12945107	0.02102367	0.31624466	0.0107712
I06-02a T1 - 1	0.80978519	0.01266529	0.30114669	0.00785515
I06-02a D3 - 9	0.85424332	0.01513329	0.29934223	0.00914262
I06-02a D3 - 8	0.64096719	0.01191096	0.30717801	0.00960364
I06-02a D3 - 7	1.07632927	0.03411962	0.30225339	0.01651351
I06-02a D3 - 6	0.39849994	0.00751275	0.29635052	0.00981244
I06-02a D3 - 5	0.52307436	0.01230611	0.30072012	0.01124454
I06-02a D3 - 4	0.61565463	0.01184995	0.29369151	0.00970593
I06-02a D3 - 3	0.33787709	0.00665273	0.28744096	0.00928689
I06-02a D3 - 2	0.21173364	0.00410801	0.29552681	0.00837071
I06-02a D3 - 1	0.54709952	0.01007135	0.29261303	0.01065287
I06-02a D3 - 1	0.50612484	0.01314701	0.30310361	0.01187449
I06-02a D2 - 9	1.00700891	0.02584857	0.31572593	0.01463363
I06-02a D2 - 8	1.03816856	0.02503851	0.32264166	0.01386902

I06-02a D2 - 7	0.63336897	0.01398325	0.29673153	0.01190244
I06-02a D2 - 6	1.3324946	0.03545649	0.29608164	0.01568523
I06-02a D2 - 5	0.9470828	0.02300595	0.29466536	0.01312434
I06-02a D2 - 4	1.44560699	0.03868588	0.29935192	0.01535088
I06-02a D2 - 3	0.89791835	0.02161975	0.30383678	0.01376292
I06-02a D2 - 2	0.95951863	0.02126513	0.29761818	0.01193287
I06-02a D2 - 1	1.01712161	0.02407976	0.31573124	0.01567109
I06-02a D2 - 1	0.67549525	0.01320018	0.28965341	0.00986921
I06-02a D1 - 9	0.63717818	0.01234783	0.28517366	0.0086099
I06-02a D1 - 8	0.6846354	0.01238925	0.29760189	0.00948021
I06-02a D1 - 7	0.65448773	0.01204477	0.28200675	0.00922296
I06-02a D1 - 6	0.65045921	0.01177951	0.29388645	0.00909853
I06-02a D1 - 5	0.95388564	0.01572784	0.30071579	0.00924247
I06-02a D1 - 5	1.023749	0.01734473	0.31058807	0.01068205
I06-02a D1 - 5	1.300945	0.02365287	0.33047768	0.0105867
I06-02a D1 - 5	1.33719187	0.02263904	0.31708484	0.01041506
I06-02a D1 - 5	0.58770966	0.01132688	0.29604004	0.01050007
I06-02a D1 - 4	1.28841487	0.02135506	0.32519415	0.00907463
I06-02a D1 - 4	0.89287905	0.01482173	0.3069851	0.00873933
I06-02a D1 - 4	1.37037952	0.02783123	0.32199699	0.01174671
I06-02a D1 - 4	0.92813282	0.01893123	0.32047443	0.01147959
I06-02a D1 - 4	0.7557785	0.01489163	0.30587197	0.01039373
I06-02a D1 - 4	0.79350102	0.01667765	0.31250587	0.01140231
I06-02a D1 - 4	0.91632472	0.01803657	0.32042186	0.01177384
I06-02a D1 - 4	0.77658893	0.01483782	0.3128542	0.01073878
I06-02a D1 - 4	0.77020853	0.01657669	0.32419435	0.01195357
I06-02a D1 - 4	0.63929628	0.01239246	0.30139375	0.0099507
I06-02a D1 - 4	0.56489277	0.01045083	0.28819638	0.01049978
I06-02a D1 - 3	0.66482532	0.01309806	0.30573809	0.0125762
I06-02a D1 - 3	0.84317779	0.01898484	0.3109638	0.01235908
I06-02a D1 - 3	2.38146796	0.05171613	0.35400808	0.01355144
I06-02a D1 - 3	2.1925667	0.04548182	0.35529871	0.01285394
I06-02a D1 - 3	1.58465159	0.02996535	0.33637948	0.01100459
I06-02a D1 - 3	1.30381629	0.03441998	0.32438917	0.01182439
I06-02a D1 - 3	1.25395674	0.02332149	0.32472593	0.01091479
I06-02a D1 - 3	1.58851247	0.03053391	0.33024596	0.01129813
I06-02a D1 - 3	1.52937466	0.02834601	0.32920164	0.01058221
I06-02a D1 - 3	1.18595891	0.02129642	0.32353269	0.0101839
I06-02a D1 - 3	0.81804768	0.0171944	0.29330408	0.01165592
I06-02a D1 - 2	1.18002201	0.02006132	0.31762339	0.01012616
I06-02a D1 - 2	1.8059273	0.03712331	0.34582871	0.01241201
I06-02a D1 - 2	1.1947559	0.0205288	0.3163904	0.0093135
I06-02a D1 - 2	1.6263408	0.03336384	0.33850263	0.01217262
I06-02a D1 - 2	1.40731414	0.02576736	0.31468485	0.01038195
I06-02a D1 - 2	2.16361333	0.04463433	0.36708762	0.01442859
I06-02a D1 - 2	1.20595293	0.0210808	0.32330171	0.00984219
I06-02a D1 - 2	0.70955417	0.01224971	0.30655	0.0088763
I06-02a D1 - 2	0.59506788	0.01064877	0.29759649	0.00895248
I06-02a D1 - 2	1.65453919	0.03171887	0.34408298	0.01150781
I06-02a D1 - 2	0.62386145	0.01198253	0.30058821	0.00954675
I06-02a D1 - 1	0.87545609	0.01486025	0.30889972	0.00888583
I06-02a D1 - 1	0.77867019	0.01463707	0.30770265	0.0113341
I06-02a D1 - 1	1.42658674	0.02640388	0.34247991	0.01104
I06-02a D1 - 1	0.80844437	0.01358026	0.3013024	0.00877102
I06-02a D1 - 1	0.80882358	0.01426439	0.30274346	0.00961194
I06-02a D1 - 1	0.98619648	0.01947279	0.31410555	0.01086829
I06-02a D1 - 1	1.14167665	0.02023299	0.31988299	0.01055696
I06-02a D1 - 1	1.09661	0.02149564	0.3080431	0.0110298
I06-02a D1 - 1	0.80568351	0.01488084	0.30218534	0.0099891

Appendix B 7: Lu-Hf Raw Data.

APPENDIX C: ISOSTASY CALCULATIONS

To estimate certain properties such as density, *thermal conductivity and *heat production, simple weighted molar mass for minerals in the whole rock sample were calculated. *these were not calculated due to limitations on time.

	Country	Location	Provinces	Sub_Province1	Sub_Province2	Density	Moho_Depth	Pressure (Kbar)		Temperature	latitude_true	longitude_tr	age_peak	age_peakerr	Notes
0	**Madagascar**	Northern Madagascar	Bemarivo Block	Bemivaro Belt		2750	31.3	9.1	0.2	925	-14.662432	49.658425			
1	**Madagascar**	Southern Madagascar	Bekliv Block	Androyan Block		2709.7	35.04	11.2	1.8	1000	-24.619257	45.618667	540		
5	**Madagascar**	Central Madagascar	Itremo Block	Ikalamavony Domain		2695.8	39.952	12.8	2.2	857					
8	**Sri Lanka**	Central Sri Lanka	Highland Complex			2789.75	35.6127	8.7	0.7	800	7.5458	80.837	539	6	
9	**Sri Lanka**	Central Sri Lanka	Highland Complex			2899.4	33.0185	6.05	0.85	730	7.2962	80.375	539	6	
11	**India**	Southern India	Southern Granulite Terrain			3107.7	50.5981	11.5	1.5	950	11.13575	78.047917	535	4.9	
13	**India**	Southern India	Southern Granulite Terrain			2653.5	43.0931	11.15	1.05	996	10.944675	78.05922	521	8	
14	**India**	Southern India	Southern Granulite Terrain			2761.1	36.78	6.4	0.2	950	8.516487	77.0012	544	5	
15	**India**	Southern India	Southern Granulite Terrain			2749.6	42.9649	11	2	900	9.442253	77.593422	546.7	5.9	
19	**Yemen**	South Eastern Yemen	North Azania		Azania	2934.6	34.3926	7.15	0.35	813	14.0428	46.905	760		
20	**Saudi Arabia**	North Western Saudi Arabia	Midyan Terrane	Arabian Shield	Arabian Nubian Shield	2844.1	29.7953	4.5	0.5	670	26.167	37.0157	632	3	**WE ARE USING A PROXY (NO DATA AVALIABLE FOR THIS AREA**
21	**Saudi Arabia**	North Western Saudi Arabia	Midyan Terrane	Arabian Shield	Arabian Nubian Shield	2844.1	29.7953	5.4	0.8	670	26.287	37.001	676		**WE ARE USING A PROXY (NO DATA AVALIABLE FOR THIS AREA**
22	**Saudi Arabia**	North Western Saudi Arabia	Midyan Terrane	Arabian Shield	Arabian Nubian Shield	2844.1	29.7953	5.6	0.3	615	29.34	34.559	620	6	**WE ARE USING A PROXY (NO DATA AVALIABLE FOR THIS AREA**
23	**Saudi Arabia**	North Western Saudi Arabia	Midyan Terrane	Arabian Shield	Arabian Nubian Shield	2844.1	29.7953	5.35	1.55	725	26.167	37.0157	750		**WE ARE USING A PROXY (NO DATA AVALIABLE FOR THIS AREA**
24	**Saudi Arabia**	North Western Saudi Arabia	Midyan Terrane	Arabian Shield	Arabian Nubian Shield	2844.1	29.7953	4.8	1.2	330	26.1236	37.0487	635	15	**WE ARE USING A PROXY (NO DATA AVALIABLE FOR THIS AREA**
26	**Egypt**	North Eastern Egypt	Sinai Shield	Sinai peninsula	Arabian Nubian Shield	2806.9	29.2463	7.5	0.5	750	28.43	34.135	587		Two instances of metamorphism w 25
27	**Egypt**	North Eastern Egypt	Sinai Shield	Sinai Peninsula	Arabian Nubian Shield	2821.9	28.7426	4.95	0.95	670	28.38	34.143	632	3	Two instances of metamorphism w 26
28	**Egypt**	Eastern Egypt	East Desert Terrain		Arabian Nubian Shield	3053.8	28.2796	4.6	0.3	555	26.388165	33.5006695	625	5	
29	**Egypt**	Eastern Egypt	East Desert Terrain		Arabian Nubian Shield	2941.3	27.5986	7.5	0.5	750	26.0879	33.9032	582	0.2	
30	**Egypt**	Eastern Egypt	East Desert Terrain		Arabian Nubian Shield	2878.9	24.92	7	0.5	650	24.6666	34.6666	593	4	
31	**Israel**	Central Southern Israel	Israel Accretionary Complex		Arabian Nubian Shield	2806.9	29.2463	5.8	0.1	615	29.34	34.559	620	6	
32	**Jordan**	Western Jordan	Arabian Platform		Arabian Nubian Shield	2820.7	33.8074	5.5	0.5	700	30.124866	35.2623487	625		
33	**Sudan**	Central East Sudan	Haya Terrane		Arabian Nubian Shield	2965.4	35	5.75	0.25	950	16.191985	32.77344	602		
34	**Eritrea**	Associated to Upper Ethiopia	Nakfa Terrane		Arabian Nubian Shield	2964.9	34.1148	8	0.5	700	15.421	39.5693	593	5	Using a base value for Nakfa Terrane Metamorphics, lack of dat
35	**Eritrea**	Associated to upper Ethiopia	Nakfa Terrane	Haya Terrane Border	Arabian Nubian Shield	2930.5	34.206	9	0.5	600	15.3227	36.7226			Using a base value for Nakfa Terrane Metamorphics, lack of dat
36	**Ethiopia**	Upper Ethiopia	Nakfa Terrane		Arabian Nubian Shield	2930.5	34.206	8.2	1	637	9.072778	35.901667	590	6	Using a base value for Nakfa Terrane Metamorphics, lack of dat
37	**Ethiopia**	Upper Ethiopia	Nakfa Terrane		Arabian Nubian Shield	2930.5	34.206	8.1	2.1	710	8.1666667	34.834167	533	12	Using a base value for Nakfa Terrane Metamorphics, lack of dat
38	**Ethiopia**	Upper Ethiopia	Nakfa Terrane		Arabian Nubian Shield	2930.5	34.206	8.6	2.2	570	9.001944	35.375833	604	6	Using a base value for Nakfa Terrane Metamorphics, lack of dat
39	**Kenya**	Southern Kenya	Tanzania Southern Granulites	Nakfa Terrane Border	Mozambique Belt	2837.4	40.357	10.9	0.2	780	-3.462913	38.570591	629	6.8	Using a base value for the Granulites at the border of nakfa terr
40	**Kenya**	Southern Kenya	Tanzania Southern Granulites	Nakfa Terrane Border	Mozambique Belt	2837.4	40.357	12	0.3	830	-3.384169	38.363527	644	15	Using a base value for the Granulites at the border of nakfa terr
41	**Kenya**	Southern Kenya	Tanzania Southern Granulites	Nakfa Terrane Border	Mozambique Belt	2837.4	40.357	7.88	0.1	800	-2.349705	38.196678	638	1.8	Using a base value for the Granulites at the border of nakfa terr
42	**Tanzania**	Central Western Tanzania	Tanzania Southern Granulites		Mozambique Belt	2837.4	40.357	12.5	0.5	800	-7.693969	36.909978	640	na	Using a base value for the Granulites at the border of nakfa terr
43	**Tanzania**	Central Western Tanzania	Tanzania Southern Granulites		Mozambique Belt	2837.4	40.357	10.25	0.75	855	-7.116612	37.655259	635	15	Using a base value for the Granulites at the border of nakfa terr
44	**Tanzania**	Western Tanzania	Ubendian Belt	Tanzania Craton Border	Mozambique Belt	2939.3	37	11	3.5	710	-7.016667	31.016667	593	20	Data From border of ubendian belt and tnzania craton boundary
45	**Tanzania**	Southern Tanzania	Tanzania Southern Granulites	Usagaran Belt Border	Mozambique Belt	2756.7	38.4461	8.5	2.5	810	-8.99111	36.316389	642	0.9	Dat from usagaran belt and tnzania granulite border
46	**Mozambique**	North Eastern Mozambique	Cabe Delgado Nappe		Mozambique Belt	2837.4	40.357	15.7	1.4	949	-13.536621	40.023039	557	16	**WE ARE USING A PROXY (NO DATA AVALIABLE FOR THIS AREA**
47	**Mozambique**	North Eastern Mozambique	Cabo Delgado Nappe		Mozambique Belt	2837.4	40.357	12.3	1.5	914	-11.459522	38.4742949	575	1	**WE ARE USING A PROXY (NO DATA AVALIABLE FOR THIS AREA**
48	**Mozambique**	Central Mozambique	Lurio Blet		Mozambique Belt	2837.4	40.357	9.2	1.8	747	-12.859359	37.98223	555	11	**WE ARE USING A PROXY (NO DATA AVALIABLE FOR THIS AREA**
50	**Mozambique**	Central Mozambique	Lurio Blet		Mozambique Belt	2837.4	40.357	11.8	1.8	950	-16.162303	37.115239	596	11	**WE ARE USING A PROXY (NO DATA AVALIABLE FOR THIS AREA**

Appendix C 1: Parameters, Pressures, densities from (Appendix C).

Pressure (Pa)	Depth(t)	C1_p1*h1	C1_crustalco	C1_density	C1_density	C1_thickness	C2_thickness	C2_p*h	C1_h*m	C2_h*m	Elevation Peak (relative c	
900000	33.37253061	95111.7122	179840.812	2828.2831	2850	64.6725306	31.3	84729.1	213419.351	103290	-3.6200685	3.62006847
1120000	42.1479189	120121.569	214974.849	2817.5745	2778.57143	77.1879189	35.04	94853.28	254720.132	115632	-4.987485	4.98748505
1280000	48.41741793	137989.641	246139.705	2829.71337	2805.12821	88.3694179	39.952	108150.064	291619.079	131841.6	-5.4143697	5.4143697
940000	34.35910889	97923.4603	194327.039	2826.73336	2804.28571	69.9718089	35.6127	96403.5789	230906.969	117521.91	-3.6354521	3.63545213
690000	24.26723415	69161.6173	158542.697	2823.65108	2804.28571	57.2857342	33.0185	89381.0795	189042.923	108961.05	-2.3357658	2.33576576
1200000	39.37508304	112218.987	252881.705	2810.63419	2780	89.973183	50.5981	140662.718	296911.504	166973.73	-5.3693295	5.36932951
1080000	41.50342981	118284.775	238083.593	2814.34231	2780	84.5965298	43.0931	119798.818	279168.548	142207.23	-5.6595586	5.65955861
1000000	36.93152052	105254.833	207503.233	2815.07195	2780	73.7115205	36.78	102248.4	243248.018	121374	-5.0361164	5.03611643
1200000	44.50318067	126834.065	246276.487	2815.61554	2780	87.4680807	42.9649	119442.422	288644.666	141784.17	-6.0686155	6.06861555
750000	26.06103591	74273.9523	167374.721	2845.12364	2841.42857	60.4536359	34.3926	93100.7682	199496.998	113495.58	-2.1527631	2.15276305
450000	16.1341829	45982.4213	126638.298	2850	2850	45.9294829	29.7953	80655.8771	151567.294	98324.49	-0.9089862	0.90898618
500000	17.92686989	51091.5792	131747.456	2850	2850	47.7221699	29.7953	80655.8771	157483.161	98324.49	-1.1534435	1.1534435
590000	21.15370647	60288.0634	140943.941	2850	2850	50.9490065	29.7953	80655.8771	168131.721	98324.49	-1.5934667	1.59346667
690000	24.73908045	70506.3793	151162.256	2850	2850	54.5343804	29.7953	80655.8771	179963.455	98324.49	-2.0823813	2.0823813
400000	14.34149591	40873.2633	121529.14	2850	2850	44.1367959	29.7953	80655.8771	145651.427	98324.49	-0.6645289	0.66452887
800000	29.06312909	82829.9179	161999.652	2778.05055	2706.55172	58.3094291	29.2463	79169.7341	192421.116	96512.79	-3.9671268	3.96712682
450000	16.26111116	46344.1668	124150.385	2758.38364	2706.55172	45.0037112	28.7426	77806.2182	148512.247	94850.58	-2.2213287	2.22132868
490000	16.36194068	46631.5309	123184.408	2818.32591	2800	44.6415407	28.2796	76552.8772	147317.084	93322.68	-1.4342032	1.43420318
800000	27.73511612	79045.0809	153754.491	2825.06168	2800	55.3337161	27.5986	74709.4102	182601.263	91075.38	-3.0042826	3.00428256
700000	24.79423909	70663.5814	138122.021	2824.93676	2800	49.7142391	24.92	67458.44	164056.989	82236	-2.6787417	2.67874169
590000	21.4340577	61087.0645	140256.799	2850	2850	50.6803577	29.2463	79169.7341	167245.18	96512.79	-1.6554864	1.65548638
550000	19.88314664	56666.9679	148183.6	2850	2850	53.6905466	33.8074	91516.6318	177178.804	111564.42	-1.2463508	1.24635084
550000	18.91292632	53901.84	148646.84	2850	2850	53.9129263	35	94745	177912.657	115500	-1.0623687	1.06236874
800000	27.51435024	78415.8982	170764.662	2814.50769	2785.88235	61.6291502	34.1148	92348.7636	203376.196	112578.84	-2.9364854	2.93648543
900000	31.31699682	89253.4409	181849.083	2816.52766	2785.88235	65.5229968	34.206	92595.642	216225.889	112879.8	-3.4528481	3.45284812
820000	28.53326377	81319.8017	173915.444	2815.04249	2785.88235	62.7392638	34.206	92595.642	207039.57	112879.8	-3.0732482	3.07324816
810000	28.18529713	80328.0968	172923.739	2814.84753	2785.88235	62.3912971	34.206	92595.642	205891.281	112879.8	-3.0257982	3.02579817
860000	29.92513029	85286.6213	177882.263	2815.80119	2785.88235	64.1311303	34.206	92595.642	211632.73	112879.8	-3.2630481	3.26304814
1090000	39.17285797	111642.645	220889.044	2826.65755	2804	79.529858	40.357	109246.399	262448.531	133178.1	-4.1555021	4.15550215
1200000	43.12608217	122909.334	232155.733	2827.7629	2804	83.4830822	40.357	109246.399	275494.171	133178.1	-4.6945782	4.69457818
788000	28.31946063	80710.4628	189956.862	2822.96858	2804	68.6764606	40.357	109246.399	226632.32	133178.1	-2.6754934	2.67549342
1300000	46.71992235	133151.779	242398.178	2828.68067	2804	87.0769224	40.357	109246.399	287353.844	133178.1	-5.1846473	5.18464729
1100000	39.53224199	112666.89	221913.289	2826.76255	2804	79.889242	40.357	109246.399	263634.499	133178.1	-4.2045091	4.20450906
1200000	41.63098206	118648.299	218807.299	2828.35459	2804	78.6309821	37	100159	259482.241	122100	-4.5893763	4.58937634
1500000	55.485701	158134.248	262207.841	2831.17229	2804	93.931801	38.4461	104073.593	309974.943	126872.13	-6.4361496	6.43614962
1570000	56.42329084	160806.379	277417.93	2866.47134	2889.5	96.7802908	40.357	116611.552	319374.96	133178.1	-7.6940851	7.69408511
1510000	54.26698673	154660.912	271272.464	2866.8467	2889.5	94.6239867	40.357	116611.552	312259.156	133178.1	-7.4000436	7.40004365
970000	34.86024976	99351.7118	215963.263	2871.1933	2889.5	75.2172498	40.357	116611.552	248216.924	133178.1	-4.7536704	4.75367042
1400000	50.31376254	143394.223	260005.775	2867.58121	2889.5	90.6707625	40.357	116611.552	299213.516	133178.1	-6.8609676	6.86096762

Appendix C 2: Depth, Crustal thickness, Weighted Crustal Densities and the Depth.

Crustal Layout (modern)					
Southern Granulite Terrain	Vijaya Rao et al. 2006	Vellar - Bhavani Profile			
Density	**Crust(km)**	**Crustal Column**			
2730	9000	24570000			
2770	12000	33240000			
2750	14000	38500000			
2870	6000	17220000			
3330					
2780	**Average for (Crustal Column 2)**	28382500			
Sri Lankan Highland Complex					
Southern Granulite Terrain	Vijaya Rao et al. 2006	Vellar - Bhavani Profile			
Density	**Crust(km)**	**Crustal Column**			
	9000	0			
	12000	0			
	14000	0			
	6000	0			
3330					
#DIV/0!	**Average for (Crustal Column 2)**	0			
Eastern Mozambique					
Cabo Delgado and Associates	Thor Leinweber et al. 2013				
Density	**Crust(km)**				
2690	7	0.175			
2900	26	0.65			
3050	7	0.175			
3330					
2889.5	40				
South West Saudi Arabia and Yemen	Mooney ad Healey, 1986				
Density	**Crust (km)**	**Percent**			
2750	22	0.628571429			
2950	7	0.2			
3050	6	0.171428571			
3330					
2841.428571	35				
Egypt (Sinai Peninsula)	Saleh et al. 2006				
Density	**Crust(km)**	**Percent**			
2390	6	0.206896552			
2750	17	0.586206897			
2900	6	0.206896552			
2706.551724	29				
Egypt (East Desert Terrane)	Saleh et al. 2006				
Density	**Crust(km)**	**Percent**			
2400	1	0.034482759			
2750	16	0.551724138			
2900	12	0.413793103			
2800	29				
Western Arabian Shield (Saudi Arabia, Jordan and Israel)	Hansen et al. 2007				
Density	**Crust(km)**	**Percent**			
2850	Average upper crus given for whole AS	1			
Madagascar (Androyen) Inferred	Rindraharisaona et al. 2017				
Inferred Lithology	**Crust(km)**	**Inferred Density**			
Felsic Lower density	10	2650	0.2857143		
Felsic Higher density	10	2800	0.2857143		
Intermideate Granite	15	2850	0.4285714		
2778.571429	35				
Madagascar (Ikalamavony) Inferred	Rindraharisaona et al. 2017			**Error**	
Felsc Lower Density	5	2650	0.1282051	50	
Felsic Higher Density	15	2800	0.3846154	50	
Intermediate granite	19	2850	0.4871795	50	
2805.128205	39				
2811.53	2711.53			25	
Sri Lanka Inferred	Dreiling et al. 2020				
Felsic Lower density	2750	10	0.2857143		
Felsic Higher density	2800	12	0.3428571		
Intermediate	2850	13	0.3714286		
2804.285714	35	35			
Sudan Averaged	Qureshi 1971				
2850	35	1			
Ethiopian Rift 2D model	Mahatsente et al. 1999				
2700	11	0.323529412			
2780	14	0.411764706			
2900	9	0.264705882			
2785.882353	34				
Kenya Rift 2d Model	Simyu and Keller. 1994				
2710	11	0.275			

Appendix C 3: Weighted crustal Densities